

**OPTICAL PROCESSING TECHNIQUES**  
**Final Report**  
**1 March 1967 Through 29 February 1968**

October 1968

Prepared Under NASA Grant NGR-23-005-195<sup>235</sup>  
Radar and Optics Laboratory  
Willow Run Laboratories  
Institute of Science and Technology  
The University of Michigan  
Ann Arbor, Michigan

NATIONAL AERONAUTICS AND SPACE ADMINISTRATION

FACILITY FORM 602

N 69 - 10976	(ACCESSION NUMBER)	(THRU)
115	(PAGES)	1
CR - 97741	(NASA CR OR TMX OR AD NUMBER)	23
		(CATEGORY)



## NOTICES

Sponsorship. The work reported herein was conducted by the Willow Run Laboratories of the Institute of Science and Technology for the National Aeronautics and Space Administration under Grant NGR-23-005-195. Contracts and grants to The University of Michigan for the support of sponsored research are administered through the Office of the Vice-President for Research.

Availability Notice. Libraries of contractors and of other qualified requesters may obtain additional copies of this report by submitting NASA form 492 directly to:

Scientific and Technical Information Facility  
P. O. Box 5700  
Bethesda, Maryland 20014

**OPTICAL PROCESSING TECHNIQUES**  
**Final Report**  
**1 March 1967 Through 29 February 1968**

October 1968

Prepared Under NASA Grant NGR-23-005-195<sup>235</sup>  
Radar and Optics Laboratory  
Willow Run Laboratories  
Institute of Science and Technology  
The University of Michigan  
Ann Arbor, Michigan

NATIONAL AERONAUTICS AND SPACE ADMINISTRATION

## FOREWORD

This report was prepared by the Radar and Optics Laboratory of the Willow Run Laboratories, a unit of The University of Michigan's Institute of Science and Technology, under National Aeronautics and Space Administration Grant NGR-23-005-195<sup>235</sup>, and covers the work performed between 1 March 1967 and 29 February 1968. This contract was monitored by Mr. Neil Patt of the NASA Electronics Research Center at Cambridge, Massachusetts. The work reported here also was supported by Air Force Contracts AF33(615)-3100 and AF33(614)-1452 and by a contract with the Army Electronics Command under Project MICHIGAN, Contract DA-23-043 AMC-00013(E). The principal investigator on this project was E. N. Leith. Section 2 of this report was contributed by D. Brumm and K. Haines, section 3 by J. Upatnieks and C. Leonard, section 4 by J. Zelenka and J. Varner, section 5 by C. Vest and A. Friesem, and sections 6 and 7 by R. Harger.

The Willow Run Laboratories report number is 8688-3-F.

## SUMMARY

This is the final report of a study of the applications of optical processing techniques and holography. The report includes studies of holographic information reduction, diffraction efficiency of photographically recorded interference patterns, recent advances in contour holography, hologram interferometry of transparent media, propagation through turbulent media, and the log-normal random process.

Some preliminary analysis and experimental results of a new technique for reducing the information content of holographic records is presented. With this technique, three-dimensional images having a large viewing angle can be generated at the expense of poorer image resolution.

Some techniques for improving the diffraction efficiency of photographically recorded interference patterns are described. The results obtained with different bleaches and different bleaching procedures are reported.

A new two-frequency contouring technique is described. With this technique, constant range or constant depth contours can be formed on image surfaces which are much larger than those previously obtainable.

A preliminary study of hologram interferometry of transparent media is reported. The use of holographic interferometry to measure the index of refraction of homogeneous media has been explored, and an investigation of its application to heat and mass transfer and related fields has been initiated.

In certain propagation experiments at optical wavelengths, it is well known that the first-order distribution of the received wavefront is log-normal. The basic way the log-normal law occurs is reviewed, and then an approximate solution to the wave equation is obtained. A thorough discussion of the log-normal process is presented, including a derivation of its likelihood functional.

PRECEDING PAGE BLANK NOT FILMED:

## CONTENTS

Foreword . . . . .	ii
Summary . . . . .	iii
List of Figures . . . . .	
1. Introduction . . . . .	1
2. Holographic Information Reduction . . . . .	2
2.1. Methods . . . . .	2
2.2. The Information-Reduction Factor . . . . .	4
2.3. Analytical Description of the System . . . . .	7
2.3.1. Ground-Glass Dispersion Function . . . . .	9
2.3.2. Resolution-Reducing Dispersion Function . . . . .	9
2.4. Related Activities . . . . .	12
2.5. Derivation of Equation 11 . . . . .	
2.6. Conclusions . . . . .	16
3. Techniques for Improving the Diffraction Efficiency of Photographically Recorded Interference Patterns . . . . .	17
3.1. Introduction . . . . .	17
3.2. Bleaching of Silver Images . . . . .	17
3.3. Measurement of Diffraction Efficiency . . . . .	23
3.4. Light Distribution in a Bleached Grating . . . . .	23
3.5. Chemical Reactions in Bleaching . . . . .	24
3.6. Discussion . . . . .	25
3.7. Chemical Reactions and Bleaching Procedures . . . . .	27
3.7.1. Kodak Chromium Intensifier Bleach . . . . .	27
3.7.2. Kodak R-10 and Modified R-10 Bleaches . . . . .	27
3.7.3. Potassium Ferricyanide Bleach . . . . .	28
3.7.4. Copper Bromide Bleach . . . . .	29
3.7.5. Mercuric Chloride Bleach . . . . .	29
4. Recent Developments in Contour Holography . . . . .	30
4.1. Introduction . . . . .	30
4.2. Theory . . . . .	31
4.3. Experimental Results . . . . .	37
4.4. Conclusions . . . . .	37
5. Hologram Interferometry of Transparent Media . . . . .	37
5.1. Introduction . . . . .	37
5.2. Basic Apparatus and Procedure . . . . .	39
5.3. Measurement of Index of Refraction of Homogeneous Media . . . . .	41
5.3.1. Analysis . . . . .	41
5.3.2. Experimental Results . . . . .	42
5.4. Experiments with Nonhomogeneous Media . . . . .	47
5.4.1. Differential Interferometry with Plane Waves . . . . .	47
5.4.2. Differential Interferometry with Diffused Light . . . . .	49
5.5. Evaluation . . . . .	49
6. Propagation Through a Turbulent Medium . . . . .	53
6.1. Introduction . . . . .	53
6.2. The Log-Normal Distribution . . . . .	53
6.3. Approximate Solution of Wave Equation . . . . .	56
6.4. Application . . . . .	61
6.5. Further Comments . . . . .	62

7. The Log-Normal Random Process . . . . .	62
7.1. Definitions	62
7.2. Stationary Processes	67
7.3. Likelihood Functional	70
Appendix: Photochromic Materials in Holography . . . . .	73
References . . . . .	104
Distribution List . . . . .	106

## FIGURES

1. Construction of a Hologram Through a Dispersion Plane . . . . .	3
2. Geometry for Calculating Information Content of a General Hologram . . . . .	5
3. Geometry for Calculating Information Content at the Hologram Plane . . . .	6
4. Imaging Through Ground-Glass Dispersion Function . . . . .	10
5. Imaging Through a Resolution-Reducing Dispersion Function . . . . .	13
6. Scanning Disc Assembly for Producing Animated Hologram Movie. . . . .	14
7. Experimental Arrangement for Recording Interference Fringes . . . . .	19
8. Transmission Before Bleaching vs. Diffraction Efficiency of Standard Bleaches . . . . .	20
9. Transmission Before Bleaching vs. Diffraction Efficiency of R-10 Series Bleaches . . . . .	21
10. Transmission Before Bleaching vs. Diffraction Efficiency of Special Bleaches . . . . .	22
11. A System for Generating Contours over Large Surfaces . . . . .	32
12. An Inclined Surface of the Object . . . . .	35
13. Depth Contours on Four Flat Surfaces . . . . .	38
14. Experimental Setup for Hologram Interferometry of Transparent Media . . . . .	40
15. Effect of Placing a Plane Parallel Object in the Beam . . . . .	43
16. Dual-Exposure Interferogram for Index-of-Refraction Measurement. . . .	44
17. Real-Time Interferograms for Index-of-Refraction Measurement . . . . .	45
18. Real-Time Interferometry for Index-of-Refraction Measurement—Nulling Technique . . . . .	46
19. Interferograms of Natural Convection in Air—Plane Wave Interferometry . . . . .	48
20. Interferograms of Natural Convection in Air-Diffuse Illumination Interferometry . . . . .	50
21. Interferograms of Natural Convection in Air-Diffuse Illumination Interferometry—Irons Heated Simultaneously . . . . .	51
22. Interferograms of Natural Convection in Air-Diffuse Illumination Interferometry—Irons Heated Separately. . . . .	52
23. Typical Geometry for Optical Communication Channel . . . . .	54
24. The Scattering Mechanism, Implied by Equation 32, that Implies a Log-Normal Distribution for $E_n/E_0$ as $n \rightarrow \infty$ if $\sum_{1}^n \xi_1$ Converges (in distribution) to a Normal Random Variable as $n \rightarrow \infty$ . . . . .	57
25. Geometry where Normal, Vice Log-Normal, Distributions May Occur. . .	58



26. The Geometry and Subdivision for the Convolution of the Scattered Wave . . . . .	60
27. Transmittance vs. Exposure Characteristics of KBr Crystals . . . . .	74
28. Transmittance vs. Exposure Characteristics of KBr Crystals Showing the Effect of Temperature Variations . . . . .	75
29. Transmittance vs. Exposure Characteristics of Photochromic Glass Showing Effect of Wavelength Variations. . . . .	76
30. Calculated Transmittance vs. Exposure Characteristics of KBr Crystals . . . . .	77
31. Diagram of Angle Convention for Reference and Signal Beams . . . . .	78
32. Calculated Half-Power Width as a Function of Hologram Thickness for Different Incidence Angles . . . . .	81
33. Calculated Half-Power Width as a Function of Incidence Angle . . . . .	81
34. Calculated Half-Power Width as a Function of Reference Angle for Different Signal Beam Angles . . . . .	81
35. Calculated Half-Power Width as a Function of Reference Angle with a Fixed Offset Angle of $60^{\circ}$ . . . . .	81
36. Calculated Optimum Reference Beam Angle as a Function of the Refractive Index of the Recording Medium . . . . .	82
37. Calculated Optimum Reference Beam Angle as a Function of Signal Beam Angle. . . . .	83
38. Diagram of Setup for Angular Orientation Sensitivity Measurements . . . . .	84
39. Curve Representing Error Due To Fixed Photomultiplier Position . . . . .	85
40. Experimental Results of Angular Orientation Sensitivity Measurements of KBr Crystals . . . . .	87
41. Experimental Results of Angular Orientation Sensitivity Measurements of Silver Halide Glass . . . . .	88
42. Experimental Results of Angular Orientation Sensitivity Measurements of Kodak 649F Spectroscopic Plates . . . . .	90
43. Curve of Diffraction Efficiency as a Function of Exposure Levels for Silver Halide Glass . . . . .	91
44. Curve Illustrating Reduction of Diffraction Efficiency During Reconstruction . . . . .	91
45. Effect of Nonlinear Bleaching on KBr Crystals . . . . .	92
46. Effect of Nonlinear Bleaching on Silver Halide Glass . . . . .	92
47. Reconstructed Images from a Multiple-Exposure Hologram of 100 Recordings. . . . .	94
48. Reconstructed Images from a Multiple-Exposure Hologram of 100 Recordings Illustrating Bragg Discrimination Capabilities . . . . .	96
49. Diagram Illustrating Fringe Surfaces and Orientation of Waves. . . . .	97
50. Degradation of Reconstructed Image Due To Reduction in Temperature . . . . .	99
51. Reciprocity Curves for KBr Crystals . . . . .	100
52. Reconstructed Image of Coherently Illuminated Transparent Objects on a Dark Background . . . . .	101
53. Reconstructed Image of a Diffusely Illuminated, Transparent, Continuous-Tone Object . . . . .	102

54. Reconstructed Image of a Diffusely Illuminated Multicolor Transparency Using Silver Halide Glass . . . . .	103
55. Reconstructed Image of a Diffusely Illuminated Multicolor Transparency Using Kodak 649F Spectroscopic Plates . . . . .	103

1  
INTRODUCTION

This is the final report on a study of optical data processing techniques and applications of hologram techniques. The study began on 1 March 1967 and ended on 29 February 1968. This report includes primarily those contributions of the final six months of the grant period. The previous work performed under this grant has been reported [1].

A new technique for reducing the space-bandwidth requirements of a holographic recorder was described in the semiannual report [1]. The merit of this technique is that the information content of a hologram can be reduced radically without sacrificing the viewing angle. An analysis which indicates the improvement provided by this technique is presented here. Recent experimental results support the analytical results.

An investigation was undertaken both to examine old bleaches and to discover new ones which would improve the diffraction efficiency of photographically recorded interference patterns. Only three-dimensional diffraction gratings were considered. The diffraction of such gratings depends primarily on the index-of-refraction change which results from the bleaching process. Although diffraction efficiencies approaching 100% are theoretically possible, the highest measured value was approximately 47%. By eliminating surface reflections, this value could be increased to 60%.

The generation of range contours holographically appears to be a very promising application of hologram techniques. Here, a modification of the previously reported [1] two-frequency technique is presented. With this new version, range contours can be generated over considerably larger surfaces than were previously possible. It is also shown that contour surfaces denoting equidistant planes can easily be obtained. Such surfaces are generally much easier to interpret than ellipsoidal ones.

Holographic interferometry has been used to measure the index of refraction of a transparent, homogeneous medium, and experimental results are illustrated. Also, its applications to heat and mass transfer have been considered. To illustrate the use of holographic interferometry of nonhomogeneous media, we have examined the density field of air surrounding heated objects.

‡ The processing of holographically recorded images after they have propagated through turbulent media was first considered in the semiannual report. Here, the log-normal law representation of the received wavefront is reviewed. Then an approximate solution to the wave

equation is derived, definitions and properties pertaining to the log-normal process are presented, and the likelihood functional is obtained.

## 2

### HOLOGRAPHIC INFORMATION REDUCTION

#### 2.1. METHODS

The need for reducing the information content of a hologram while maintaining, insofar as possible, some of the image characteristics (such as resolution, viewing angle, field of view, or signal-to-noise ratio) has been well documented [2, 3, 4]. Three basic approaches to the problem have come to light.

The first and most straightforward method is to perform a spatial filtering operation on the hologram, removing all but a narrow band of frequencies. For example, in the case of a hologram made and reilluminated with a collimated reference wave, the filtering operation reduces the angular field of view which any small region of the hologram reconstructs. Thus, from any fixed position, an observer can view only part of the reconstructed image at a time, and he must scan the hologram to see the entire image. Such a system seems to have little use, although it might be of value in some particular application.

Another method is to sample the complex object field in some plane between the object and the hologram. The number of samples recorded might vary from one or two samples [5] up to a very large number [6], usually uniformly distributed. This method can reduce the spatial frequencies which must be recorded as well as the spatial bandwidth. However, the viewing angle is reduced, image resolution is slightly reduced, and usually a two-step process is necessary. In addition, the perspective becomes discontinuous, i.e., the image changes in discrete jumps as the observing position changes. The sampling method is useful when perspective can be sacrificed rather than image resolution in order to gain a reduction in the information which must be transmitted.

The dispersion method [3, 4, 7] with which we are primarily concerned is fundamentally different. Full normal perspective is preserved while the reduction in information manifests itself in a reduced resolution in the reconstructed image or in a decrease in the signal-to-noise ratio. A diagram illustrating this technique appears in figure 1. Light from the object is diffracted by a dispersion plane  $m(y)$  and falls upon the hologram plane  $h(z)$  where it is recorded. If the hologram is constructed with a reference beam diverging from a point source and is then reconstructed with a beam originating from the opposite side of the hologram but which now converges to the same point, a conjugate wavefront traveling from right to left, again diffracted by the  $m(y)$  plane is generated. If the dispersion function  $m(y)$  is strictly a

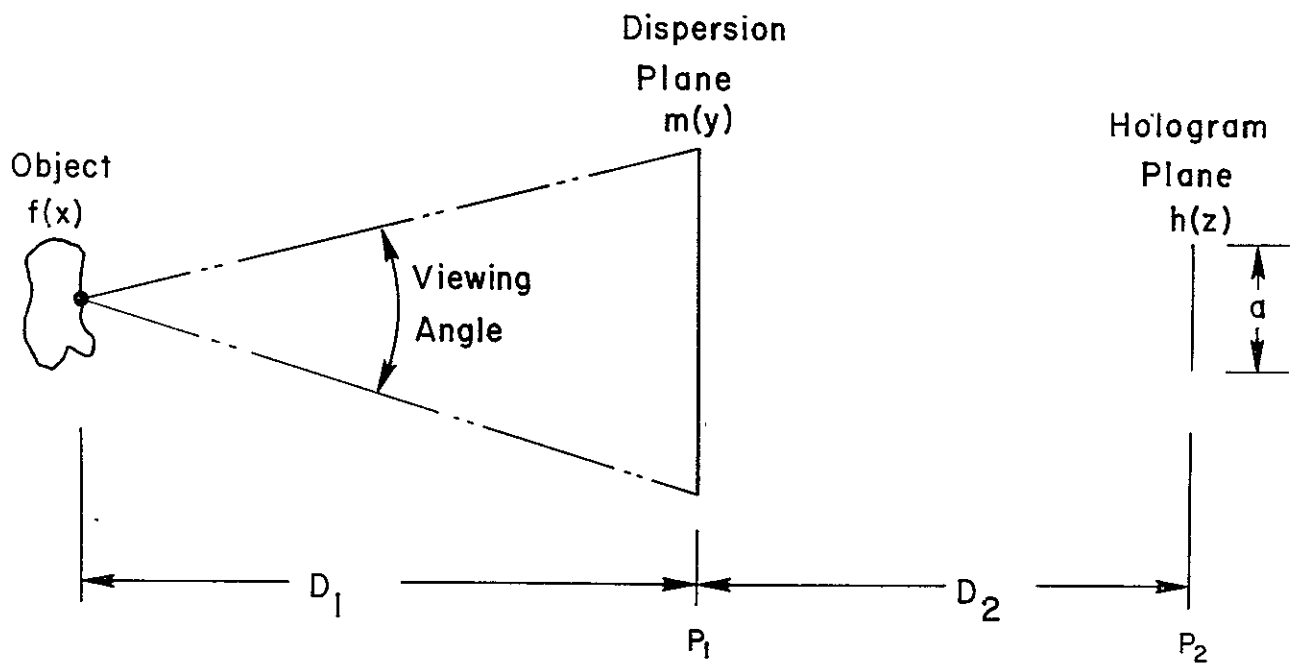


FIGURE 1. CONSTRUCTION OF A HOLOGRAM THROUGH A DISPERSION PLANE

phase function, such as say a ground glass, then a pseudoscopic image may be observed to the left of the  $m(y)$  plane [8]. An observer viewing this image cannot see beyond  $P_1$ . The scattering function appears to him to be the hologram, i.e., the source of the reconstructed wavefront. Thus, with a small hologram in  $P_2$  and a scattering function in  $P_1$ , we have simulated a large hologram which appears to be in  $P_1$ . The most important characteristic of this method is that it reconstructs an image over a large viewing angle from a relatively small hologram.

## 2.2. THE INFORMATION-REDUCTION FACTOR

To determine how much a given system reduces the information which must be recorded or transmitted, it is necessary to derive a standard means of comparison. The total information recorded by a one-dimensional plane hologram is proportional to the space-bandwidth product

$$I = kLB \quad (1)$$

where  $k$  is a constant,  $L$  is the length of the hologram, and  $B$  is the spatial bandwidth (assumed here to be essentially constant over the entire hologram). For a hologram in plane  $P_1$  of figure 2, with a point reference source  $S$ , and a field of view  $\alpha$ ,

$$B = \frac{2 \sin \alpha/2}{\lambda} \quad (2)$$

Thus for  $L = 2Y_m$ , the information content is

$$I_1 = \frac{k4Y_m \sin \alpha/2}{\lambda} \quad (3)$$

Now, instead of recording the fringe system present in  $P_1$  on a photographic plate, let us replace the plate, as shown in figure 3, with a scattering function  $m(y)$  whose extent is  $2Y_m$ , the same as the size of the previous hologram. Thus, the information  $I_1$  is not recorded, but is still present within the aperture  $|y| \leq Y_m$ . By a similar argument as above, the information recorded by a hologram in  $P_2$  with reference source  $S'$  is

$$I_2 = \frac{k2a \sin \beta/2}{\lambda} \quad (4)$$

The magnitude of  $I_2$  can be made arbitrarily small by decreasing the size of the hologram  $a$  or by increasing  $D_2$ . Increasing  $D_2$  also reduces the maximum spatial frequency which the hologram must record, thus permitting the use of a lower resolution film or other detector.

The reduction in information between a reference hologram recorded in  $P_1$  and the actual hologram recorded in  $P_2$  is

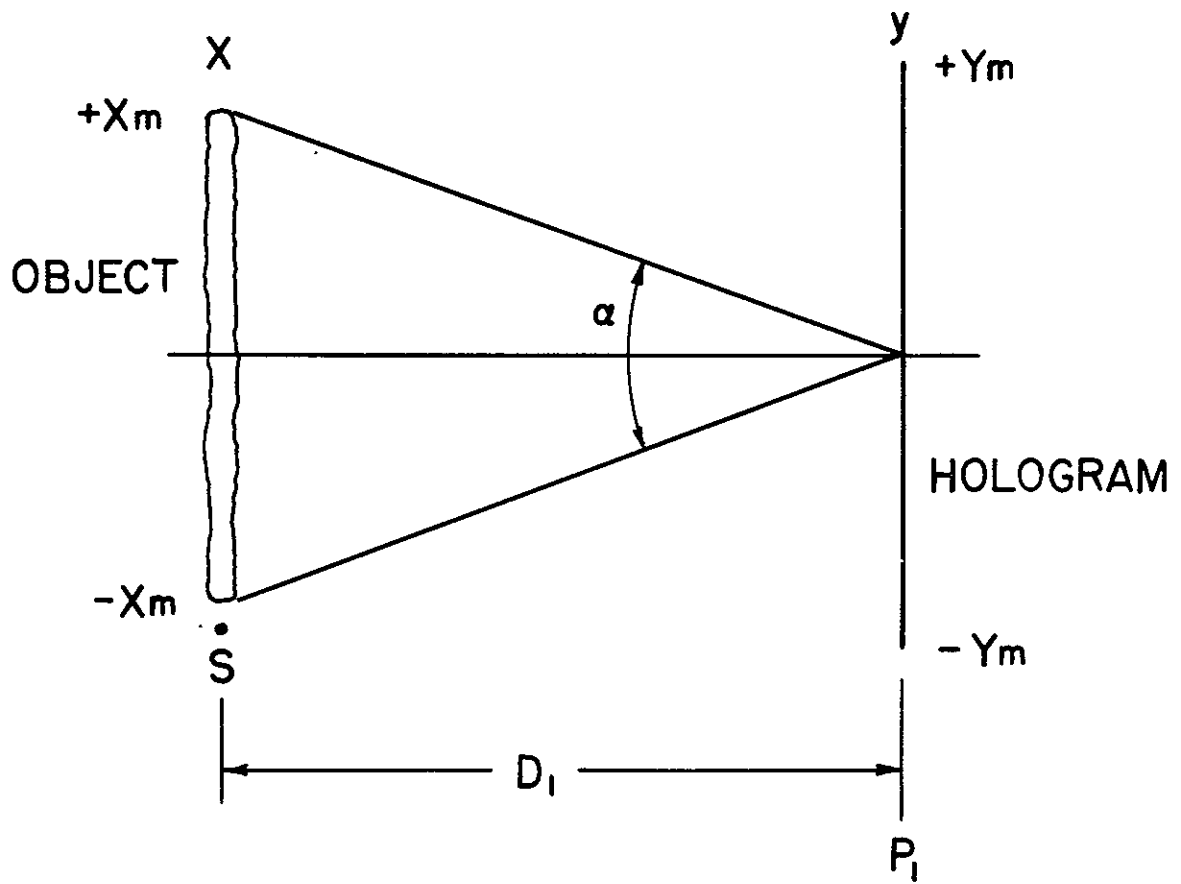


FIGURE 2. GEOMETRY FOR CALCULATING INFORMATION CONTENT OF A GENERAL HOLOGRAM

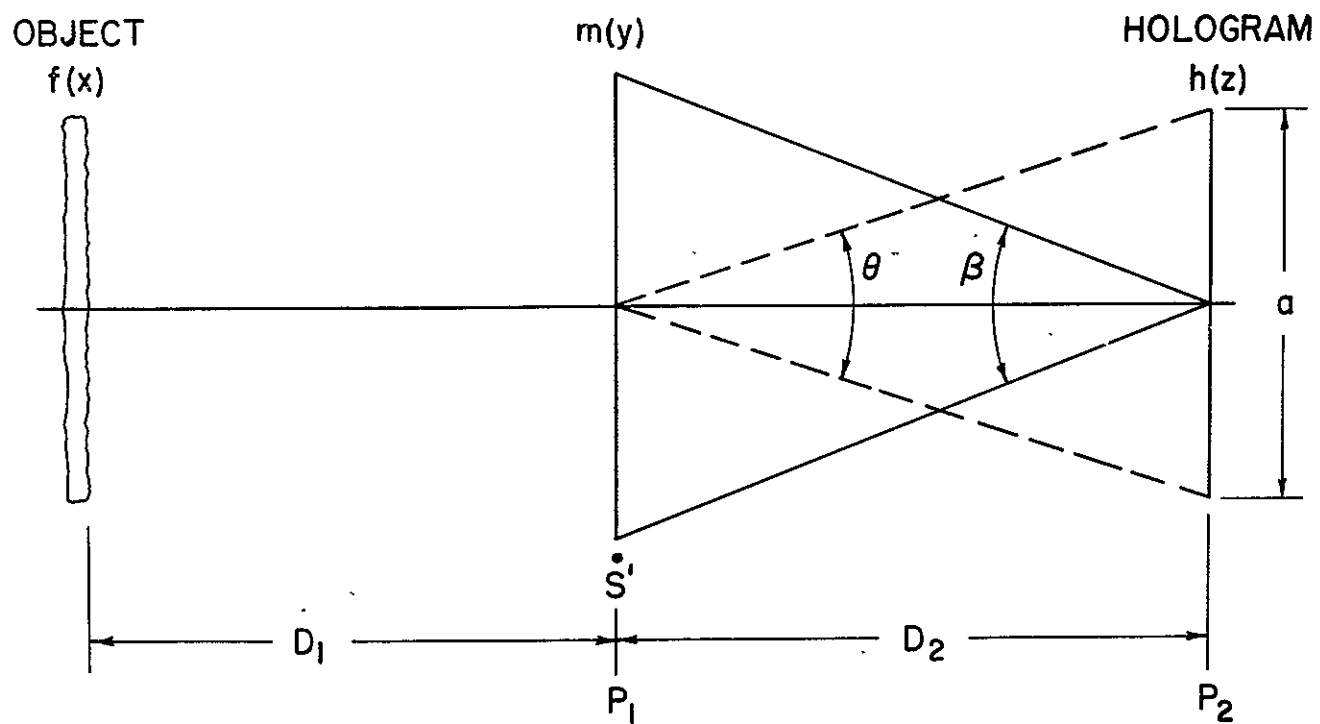


FIGURE 3. GEOMETRY FOR CALCULATING INFORMATION CONTENT AT THE HOLOGRAM PLANE



$$R = \frac{I_1}{I_2} = \frac{2Y_m \sin \alpha/2}{a \sin \beta/2} \quad (5)$$

In most applications,  $X_m \approx Y_m$ ,  $D_1 \ll D_2$ , and  $a \ll Y_m$ . This allows the approximation

$$\sin \beta/2 \approx \frac{Y_m}{D_2}$$

which gives

$$R \approx \frac{2D_2 \sin \alpha/2}{a} \quad (6)$$

In the case where  $X_m \ll D_1$ , we have

$$\sin \alpha/2 \approx \frac{X_m}{D_1}$$

thus permitting the approximation

$$R \approx \frac{2X_m/D_1}{a/D_2} \approx \frac{\alpha}{\theta} \quad (7)$$

We observe that in cases where these approximations are valid, the size of the scattering function does not influence the information-reduction factor  $R$ . Since  $\theta$  can be arbitrarily smaller than  $\alpha$ , very large reductions can be achieved.

The above equations describe a one-dimensional model; for a square two-dimensional system, the information reduction is  $R^2$ .

### 2.3. ANALYTICAL DESCRIPTION OF THE SYSTEM

It is impossible to achieve a reasonable degree of data reduction without sacrificing signal-to-noise ratio, resolution of the reconstructed image, or viewing angle. In order to examine what happens to the image, it is convenient first to present a general analytical description of the system.

The wavefront radiating from the object and falling upon the dispersion plane in figure 1 is  $g_1(y)$ , and that which is rediffracted by the dispersion plane and forms an image is  $g_2(y)$ . For simplicity in the analysis, the hologram aperture is assumed to be Gaussian weighted with a variable standard deviation of  $a$ . Using the conventional simplification of the Fresnel diffraction formula, we may write the wavefront at the hologram plane as

$$h(z) = \left\{ \int g_1(y') m(y') \exp \left[ \frac{-jk}{2D_2} (y' - z)^2 \right] dy' \right\} \exp \left( \frac{-z^2}{2a^2} \right) \quad (8)$$

Upon reillumination of the hologram, the wavefront, at the left of the dispersion plane, which will form the image is

$$g_2(y) = m(y) \iint g_1^*(y') m^*(y') \exp \left[ \frac{jk}{2D_2} (y' - z)^2 \right] dy' \\ \exp \left[ \frac{-jk}{2D_2} (y - z)^2 \right] \exp \left( \frac{-z^2}{2a^2} \right) dz$$

This can be rewritten, after successive Fourier transformations, as

$$g_2(y) = \left\{ a \left[ g_1^*(y) m^*(y) \exp \left( \frac{jk}{2D_2} y^2 \right) \right] * \exp \left( \frac{-k^2 a^2}{2D_2^2} y^2 \right) \right\} m(y) \exp \left( \frac{-jk}{2D_2} y^2 \right) \quad (9)$$

Consider an on-axis point in a general object field. For this point,

$$g_1(y) = \exp \left( \frac{-jk}{2D_1} y^2 \right)$$

With the exception of a phase function in the image plane, the image function  $f_2(x)$  can be expressed as

$$f_2(x) = F_s \left( \frac{-x}{\lambda D_1} \right) * \left[ F_s \left( \frac{x}{\lambda D_1} \right) \exp \left( \frac{-D_2^2 x^2}{2D_1^2 a^2} \right) \right] \quad (10)$$

where

$$s = m(y) \exp \left[ \frac{-jk}{2} \left( \frac{1}{D_1} * \frac{1}{D_2} \right) y^2 \right]$$

and  $F_s$  is the Fourier transform of  $s$  as given by

$$F_s(u) = \int s(x) \exp(-j2\pi ux) dx$$

The total reconstructed image can then be considered to be a summation of such terms, given by equation 10, in which each term is representative of a point in the object space.

In the following discussion, the characteristics of the image resulting from the use of a ground-glass dispersion structure are derived and demonstrated. It is shown that such a structure causes the signal-to-noise ratio of the image to be reduced as the recorded information is reduced (the hologram aperture is narrowed). A different type of random structure is then de-

scribed which causes the resolution of the image to deteriorate rather than the background noise to build up.

**2.3.1. GROUND-GLASS DISPERSION FUNCTION.** Assuming that the ground glass is characterized by a random phase function, which has no transmission amplitude variations across the surface, choose a model in which the spatial bandwidth of  $m(y)$  is extremely broad and in which the phase relationship between spectral components is random. With an axial point object, the characteristics of the reconstructed image may be examined using equation 10. The width of the correlation function in (10) depends mainly on the frequency spread of the function  $F_s(x/\lambda D_1)$  and has little dependence on the size of the hologram aperture. That is, the resolution of the point image depends on the extent of the  $m(y)$  function. However, the intensity of the correlation peak is related to "a," the size of the hologram aperture. Because of the random nature of  $F_s$ , the correlation function for off-axis points is relatively constant. As  $a$  becomes smaller, this correlation becomes larger. This implies that the background noise in the image function is uniform and that it increases with decreasing aperture. In the limit, as  $a$  goes to zero, the term in the square braces is a delta function, and

$$f_2(x) \rightarrow F_s\left(\frac{x}{\lambda D_1}\right)$$

i.e., the image function  $f_2(x)$  is entirely noise.

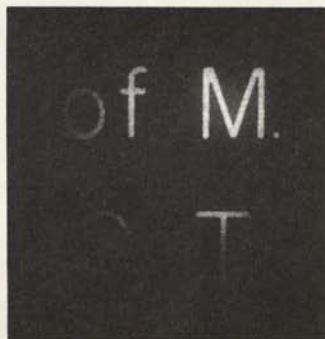
An experimental demonstration of these effects for a ground-glass dispersion function is shown in the image plane photographs of figure 4. Figure 4a is a photograph of the image using a relatively large hologram aperture. The two-dimensional information reduction factor  $R^2$  was 10. In figure 4b, the hologram aperture diameter was decreased so that  $R^2$  was 400. From these figures, it appears that reducing the hologram aperture has very little effect on the image resolution. However, there is a marked increase in the background noise as predicted.

**2.3.2. RESOLUTION-REDUCING DISPERSION FUNCTION.** In many cases it is not desirable to trade background noise in the image field for data reduction but rather to select a dispersion medium which causes the image resolution to decrease as  $R$  increases but which contributes very little to background noise.

A dispersion medium which has this effect is again purely a phase function, but one with different statistics. The dispersion function can be written

$$m(y) = \exp [j\theta(y)]$$

where  $\theta(y)$  is a random function of  $y$ . However, there are two essential restrictions on the statistics of this random function. First, the derivative of the phase  $\theta(y)$  must have a standard



(a)



(b)

FIGURE 4. IMAGING THROUGH GROUND-GLASS DISPERSION FUNCTION WITH INFORMATION CONTENT

deviation which is large enough so that light from all parts of the object field is diverted by the entire dispersion plane into the relatively narrow hologram aperture. That is, it is essential that

$$\frac{\sigma}{k} \approx \left| \frac{X_m + Y_m}{D_1} \right| + \left| \frac{Y_m}{D_2} \right|$$

where  $\sigma$  is the standard deviation of the phase rate  $\dot{\phi}$ , and  $2X_m$  and  $2Y_m$  are the dimensions of the object and dispersion function, respectively. When this requirement is satisfied, the large viewing angle is maintained. Next, the second derivative of the phase must be so small that  $\ddot{\phi}$  can be considered constant within a resolution element of the reconstructed wavefront. The size of this resolution element is  $\frac{\lambda D_2}{a}$ . The second restriction implies that the phase relationship between spectral components is not entirely random; thus the previous discussion does not apply. Using a dispersion function having these special characteristics yields an image wavefront  $g_2(y)$  which is the conjugate of the object wavefront, except for an overlaying mask. When this mask is considered as a diffracting object, its spatial frequencies may be directly related to a point-spread function in the image plane. For example, a component whose spatial frequency is  $f$  gives rise to an image-point location error of

$$\delta = D_1 \lambda f$$

The equation relating the autocorrelation of the mask function to the autocorrelation of  $\dot{\phi}$  is (from sec. 2.5)

$$R_M(\tau) \approx \frac{a^2}{[\beta^4 - R(\tau)^2]^{1/2}} \quad (11)$$

where

$$\beta^2 = \frac{k^2 a^2}{D_2^2} + \sigma^2$$

$R_M(\tau)$  is the autocorrelation function of the mask function  $M$ , and  $R(\tau)$  is the autocorrelation function of  $\dot{\phi}$ .

From this equation, it is evident that the width of the autocorrelation function of  $R_M(\tau)$  decreases as the size of the hologram aperture  $a$  decreases. The spatial frequencies of the image spread increase, thus contributing to a poorer resolution. Similarly, as the correlation function for  $\dot{\phi}$  becomes broader (that is, as  $\dot{\phi}$  becomes less rapidly varying), the image-point spread function narrows. However, there are practical limits to the breadth of  $R(\tau)$ , since a point is reached at which the image will appear excessively spotty when viewed by eye.

From equation 11, it is clear that the noise which can be attributed to the higher frequencies of  $R_M(7)$  does not build up as  $\lambda$  is decreased. These desired characteristics are demonstrated by the experimental results shown in figure 5. The object was a ring surrounding a cross. For figure 5a, the space-spatial bandwidth reduction ratio  $R^2$  was 140; for figure 5b, it was 500; and for figure 5c, it was 3600. Observe that the resolution does actually decrease in the manner predicted while the background noise is altered very little.

In the actual experiment, the dispersion medium was an aluminized random surface on glass which, instead of transmitting light, reflected it into the hologram aperture. This was a convenient method for obtaining the large variation of diffraction angles across the surface.

#### 2.4. RELATED ACTIVITIES

Some work has been done on producing a short animated movie by properly positioning a sequence of holograms in plane  $P_2$ . The experimental problems encountered in such an attempt are very difficult, however, because of the precision with which these holograms must be located. Alternatively, a single photographic plate can be fixed in position in  $P_2$ , and the individual holograms of the movie can then be recorded side by side in some regular array. This is the method we used. The necessary scanning is performed by an opaque disc from which a  $15^\circ$  sector has been removed (fig. 6). This disc is driven by a stepper motor and its associated electronics. The stepping speed can be varied to produce different frame rates.

A holographic movie which uses a reflecting scattering function is analogous to a conventional movie in that a wavefront is projected onto a screen. The distinction is that this projection is coherent, and the image can be either in front of or behind the screen, or in the same plane. The advantage of a holographic movie made in conjunction with a scattering plate over a sequence of holograms alone is that small holograms can be used without reducing the viewing angle of the real image.

#### 2.5. DERIVATION OF EQUATION 11.

In this section, an equation is developed which relates the correlation function of the overlying mask to the statistics of the dispersion function  $m(y)$ . If the second derivative of the phase of the dispersion function is so small that the first derivative may be considered constant within a resolution element of the reconstructed dispersion plane, then

$$\begin{aligned}\hat{\phi}(y) &\approx \frac{1}{y' - y} \int_y^{y'} \hat{\phi}(u) du \\ &= \frac{\phi(y') - \phi(y)}{y' - y} \text{ for } |y' - y| < \frac{\lambda D_2}{a}\end{aligned}\quad (12)$$

Using this approximation in equation 9 and assuming an on-axis point object, one gets





FIGURE 5. IMAGING THROUGH A RESOLUTION-REDUCING DISPERSION FUNCTION



FIGURE 6. SCANNING DISC ASSEMBLY FOR PRODUCING ANIMATED HOLOGRAM MOVIE



$$g_2(y) \approx \exp\left(\frac{jky^2}{2D_1}\right) M(\dot{\theta}) \quad (13)$$

where

$$M(\dot{\theta}) = \int \exp \left[ \frac{jk}{2d} (y'^2 - 2y'y) - \frac{k^2 a^2}{2D_2^2} y'^2 \right] \exp (jy'\dot{\theta}) dy'$$

The first exponential term in this equation is simply the point-image reconstruction function. The function  $M$  is the mask function, and it is this portion of the above equation whose spectral density is examined. The problem of analyzing this spectral density, or alternatively the corresponding autocorrelation function, can be solved by using the transform method of nonlinear systems [9], where  $\dot{\theta}$  is assumed to be the Gaussian input to the system, and  $M(\dot{\theta})$  is the output.

With this method, the autocorrelation  $R_M(\tau)$  of the nonlinear system output is

$$R_M(\tau) \approx \int F(\omega_1) \exp\left(\frac{-\sigma^2 \omega_1^2}{2}\right) d\omega_1 \int F(\omega_2) \exp\left(\frac{-\sigma^2 \omega_2^2}{2}\right) d\omega_2 \exp[-R(\tau)\omega_1\omega_2] \quad (14)$$

where  $F(\omega_1)$  is the Fourier transform of  $M$ . That is,

$$F(\omega_1) = \int M(\dot{\theta}) \exp(-j\theta\omega_1) d\dot{\theta} = \exp \left[ \frac{jk}{2d} \left( \omega_1^2 - 2\omega_1 y \right) - \frac{k^2 a^2}{2D_2^2} \omega_1^2 \right]$$

Inserting this function into (14) gives

$$R_M(\tau) \approx \int \exp \left[ -\omega_1 \left( R\omega_2 + \frac{jky_1}{d} \right) - \omega_1^2 \frac{\beta^2}{2} \right] d\omega_1 \int \exp \left[ -\omega_2 \left( \frac{jk}{d} y_2 \right) - \omega_2^2 \frac{\beta^2}{2} \right] d\omega_2 \quad (15)$$

where

$$\beta^2 = \frac{k^2 a^2}{D_2^2} - \frac{jk}{d} + \sigma^2$$

After integrating,

$$R_M(\tau) \approx \frac{a^2}{\sqrt{\beta^4 - R(\tau)^2}} \exp \left[ \frac{-k^2}{2d^2} \left( \frac{\tau^2 \beta^2}{\beta^4 - R^2} \pm \frac{2\tau y}{\beta^2 + R} + \frac{2y^2}{\beta^2 + R} \right) \right] \quad (16)$$

If there is to be any appreciable data reduction, either  $D_2 \gg Y_{\max}$  or  $a \ll Y_{\max}$ . With these inequalities, the exponential term may be neglected. With the exception of a weighting function of  $y$  across the mask function,

$$R_M(\tau) \approx \frac{a^2}{\sqrt{\beta^4 - R(\lambda)^2}} \quad (11)$$

In an approximate manner, we can relate the standard deviation of the function  $R_M(\tau)$  to the image-point spread. For example, if the width of  $R_M(\tau)$  is  $T$ , then the image-point spread is approximately  $\Delta X = \lambda D_1 / T$ .

## 2.6. CONCLUSIONS

The resolution-reducing dispersion function provided an image resolution loss without a decrease in signal-to-noise ratio. Another advantage of this type of dispersion function is that much less critical realignment is necessary during the reconstruction process than for the ground-glass system. A lateral misalignment on the order of the width of the correlation peak of  $R(\tau)$  will provide at least a blurry image.

Although it is desirable to use as a dispersion function a surface which varies slowly, one which varies too slowly will cause the image to appear spotty. The size of these spots is related to the width of the correlation slope function  $R(\tau)$ . A compromise solution for the slope function must be chosen.

In the dispersion-plane systems discussed so far, the pseudoscopic real image was reconstructed. Although this simplified the experimental work, the system is not limited to pseudoscopic images. A different though related dispersion function can be used to reconstruct non-pseudoscopic images. An example of a system which reconstructs an orthoscopic real image is one for which the actual image of the dispersion plane is focused by a telescope of unit magnification into a space which is readily accessible. In this focused plane, the conjugate of the dispersion function is placed. For the mirror dispersion-function system used to obtain the results of figure 5, this conjugate mirror is simply an imprint of the original surface.

It should be mentioned that the dispersion function need not be confined to a planar function, but may use functions with depth or axial variations. An example of a system using a dispersion function in two planes is one in which the first plane is an array of small diameter lenses which focuses the object onto a ground-glass plate in the second plane. This entire assembly may then be considered as the function  $m(y)$ . Using such a system yielded results in which the resolution deteriorated with decreasing aperture. With this specific dispersion function, there may be some difficulty in avoiding focusing on the lens structure itself when the image is viewed by eye. However, it does illustrate the use of a three-dimensional dispersion function.

# TECHNIQUES FOR IMPROVING THE DIFFRACTION EFFICIENCY OF PHOTOGRAPHICALLY RECORDED INTERFERENCE PATTERNS

## 3.1. INTRODUCTION

Large interference patterns can be produced easily with lasers. Such patterns may be used as diffraction gratings, Fresnel zone plates, and other optical elements. Some uses already have been described [10], and other uses also exist. The major deficiency of such optical elements is low efficiency, typically about 4%. With such an efficiency, possibly one element might be used in an optical system, but several in series would be impractical.

An investigation was undertaken to find and examine bleaches which would improve the diffraction efficiency of photographically recorded interference patterns. If these patterns are recorded in thick recording media and if the density changes are converted into corresponding refraction index changes, then, theoretically, efficiencies of 100% could be achieved [11]. In practice, efficiency is limited by such factors as absorption in the emulsion, scattering, surface reflections, and limited control over the index of refraction. With an ideal bleach, efficiency of 80% to 90% should be possible without the use of antireflection coatings on the surfaces. These efficiencies are for polarized light with the E-vector perpendicular to the plane of incidence. When the E-vector is parallel to the plane of incidence, diffraction efficiency is dependent on the angle of incidence.

Experiments have shown that different bleaching techniques should be used for two-dimensional and three-dimensional diffraction gratings. For the two-dimensional case, bleaching techniques which produce relief patterns are efficient and easy to use, whereas for the three-dimensional case, the diffraction efficiency depends on index-of-refraction change. Here we shall consider only the index-of-refraction change.

This investigation consisted of the following: (1) obtaining diffraction efficiency vs. density curves for various known bleaches, (2) finding the probable chemical reactions and identifying the chemical compounds causing the change in index of refraction, (3) investigating the losses in efficiency, (4) finding ways of stabilizing chemical compounds that tend to darken with exposure to light, and (5) finding other chemical compounds that might give the desired results.

## 3.2. BLEACHING OF SILVER IMAGES

To obtain the desired index-of-refraction change as a function of density, each exposed silver grain must be converted into a compound that has an index of refraction significantly different from that of the emulsion. The desired change can be expressed as follows: If we have a three-dimensional interference pattern described by  $T = k_0 - kI(x, y, z)$ , then we would like to replace it by a phase image such that after bleaching the transmission is one and the

index of refraction is  $n = n_0 + k_1 I(x, y, z)$ , where  $k_1$  is an appropriate constant. This gives phase variations in the emulsion of  $\exp(\gamma n_0) \exp[\gamma k_1 I(x, y, z)]$ . It is this type of phase variation that we would like to achieve.

In practice, each exposed silver grain is converted into a small dielectric particle having an index of refraction different than the emulsion. Variations in the concentration of these particles create an effective phase change. The maximum phase change should occur when the greatest difference exists between concentration of exposed silver grains in the light and dark fringe areas. If each silver atom would be replaced by one molecule of the bleach product, then all efficiency of diffraction versus density curves should have similar shapes. This is not the case, however, indicating that the mechanics of the bleaching process are more complicated.

In the bleaching process, either the silver in the emulsion should react with the bleaching chemicals to form a compound that is insoluble in water or the bleaching solution, or the silver may act as a catalyst by which the bleach produces a compound at the location of the silver particles while the silver itself is eventually removed from the emulsion. With some bleaches, the silver both forms compounds in the emulsion and acts as a catalyst. The compounds formed in the emulsion should have the following properties:

- (1) The resulting compound should be transparent to light.
- (2) The refractive index of the compound should be significantly different from that of the gelatin.
- (3) The compound should be stable and should not decompose or become opaque with exposure to light.

All the tests for diffraction efficiencies were made using the recorded interference pattern between two spherical waves with an angular separation of  $90^\circ$ , as shown in figure 7. The spatial frequencies were about 2200 lines per millimeter. The interference patterns were recorded on Kodak 649F emulsion on  $4 \times 5 \times 1/8$ -in. glass plates. The plates were developed in Kodak D-19 developer for 5 min, rinsed in short-stop bath for 15 to 20 sec, and fixed for 10 min. Continuous agitation was used in development and occasional agitation thereafter. The plates appear deep pink after fixing and become light pink after 20 min of washing in running water. After this processing, the plates were dried, the average transmission was measured, and then the plates were bleached. The detailed description of the bleaching process and of the probable chemical reactions is given in section 3.7.

Figures 8 through 10 show the average transmission before bleaching versus efficiency-of-diffraction curves for various bleaches. The Kodak Chromium Intensifier Bleach (KCIB) gives the highest efficiency, 47%, and is the only one that is linear over most of its effective range. Various treatments were tried with plates processed in the KCIB to prevent them from

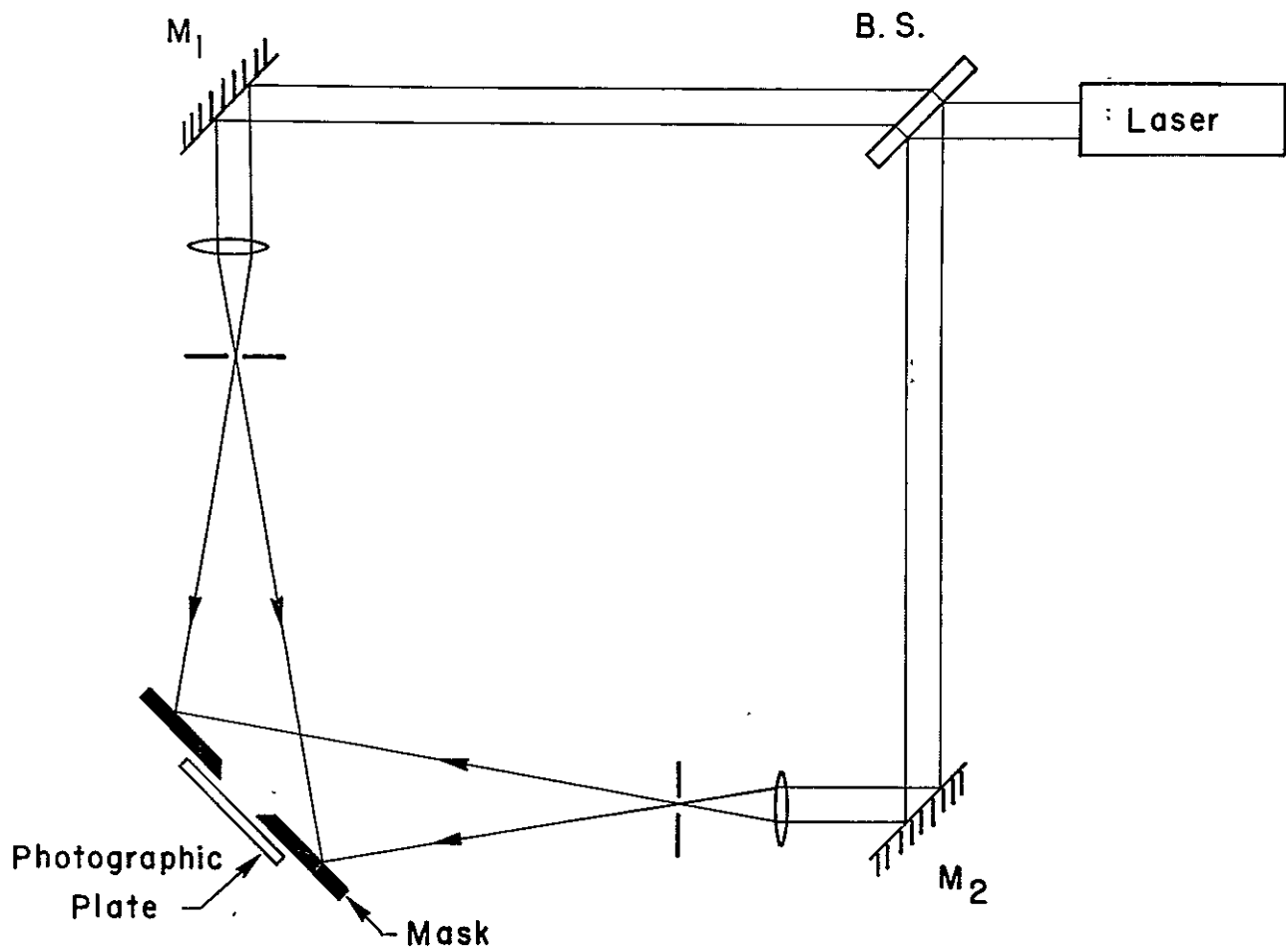


FIGURE 7. EXPERIMENTAL ARRANGEMENT FOR RECORDING INTERFERENCE FRINGES

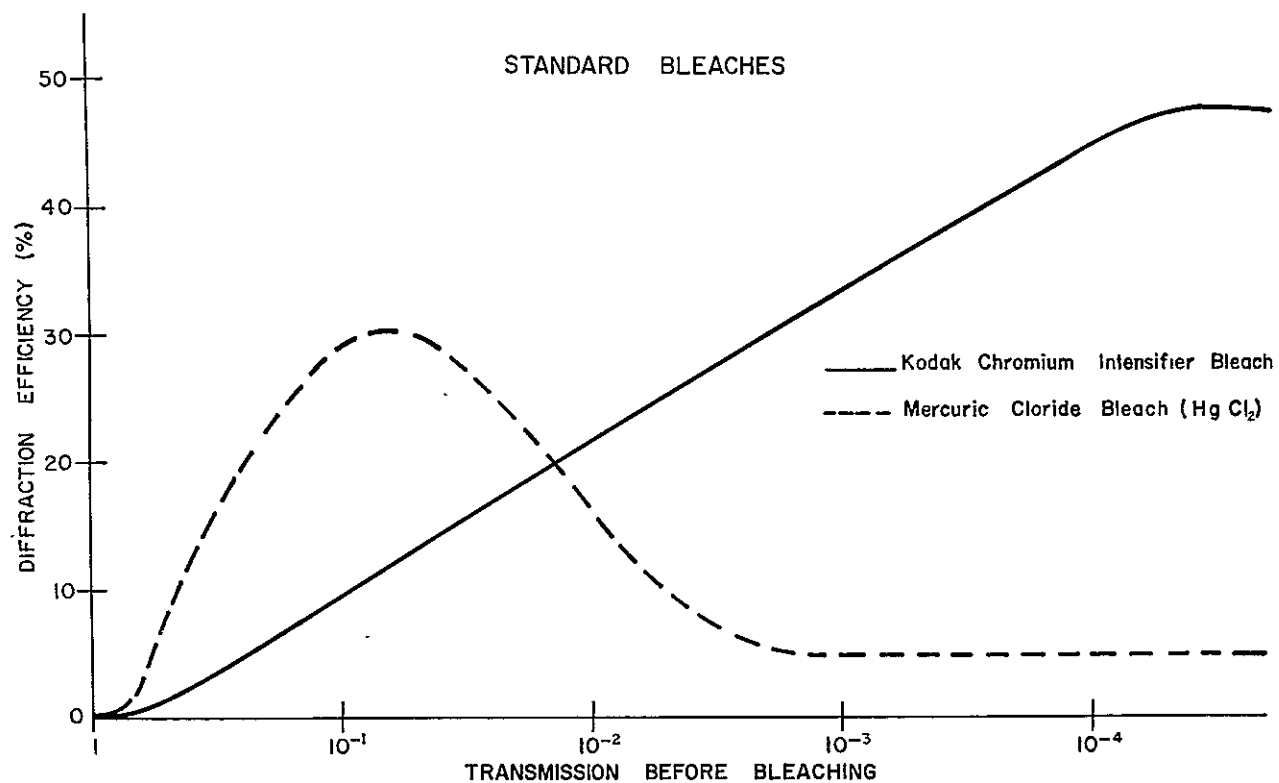


FIGURE 8. TRANSMISSION BEFORE BLEACHING VS. DIFFRACTION EFFICIENCY OF STANDARD BLEACHES

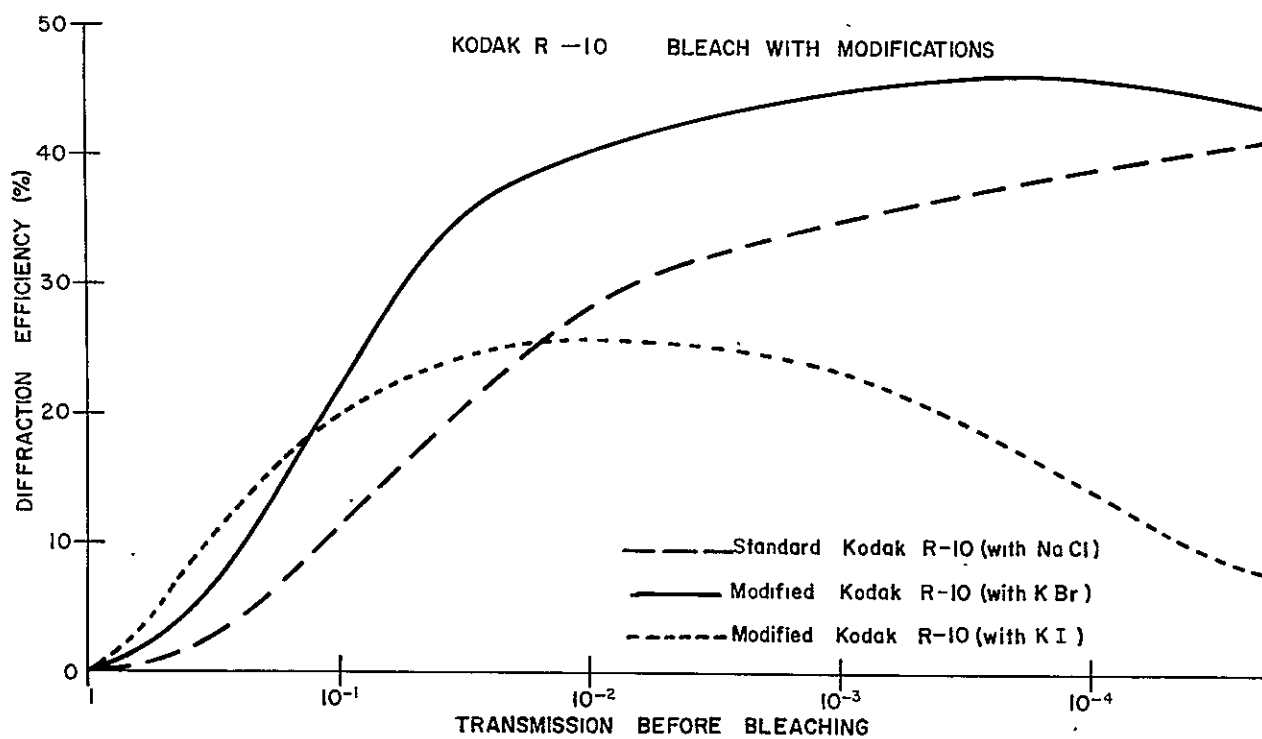


FIGURE 9. TRANSMISSION BEFORE BLEACHING VS. DIFFRACTION EFFICIENCY OF R-10 SERIES BLEACHES

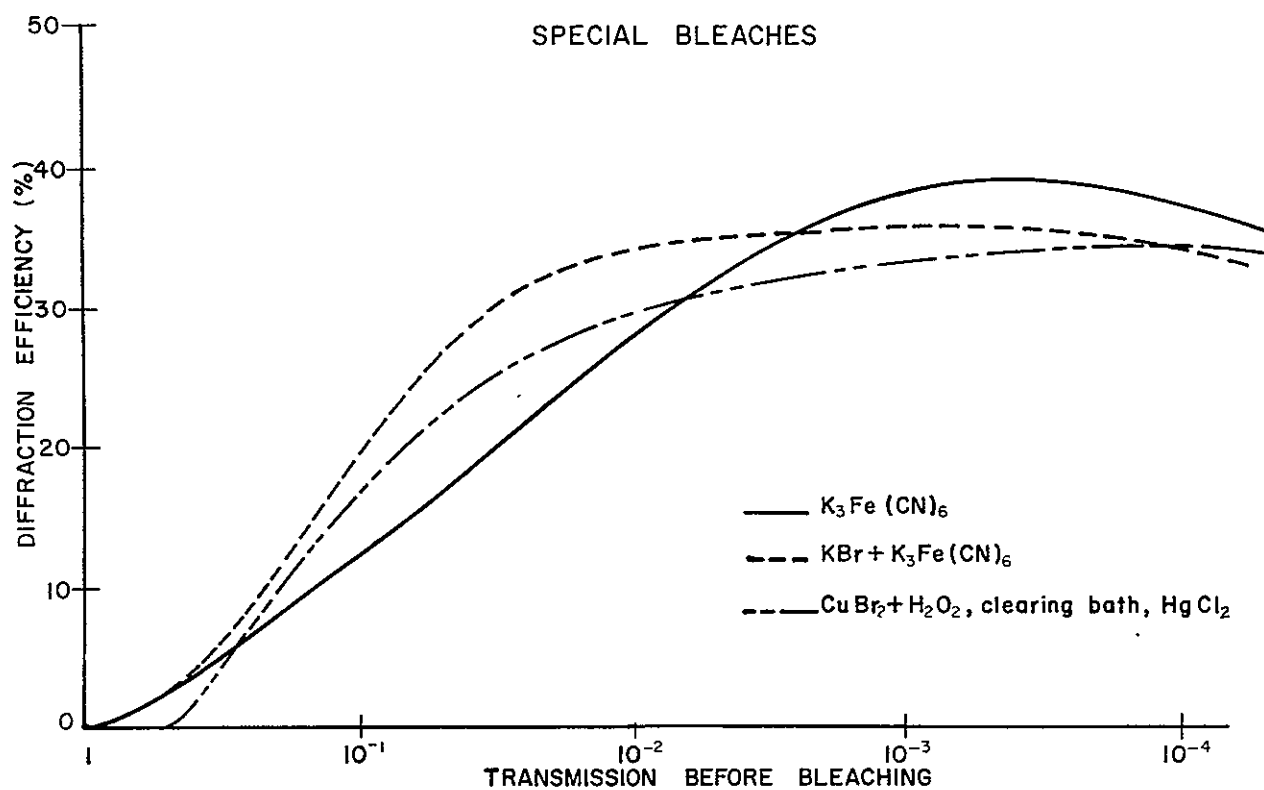


FIGURE 10. TRANSMISSION BEFORE BLEACHING VS. DIFFRACTION EFFICIENCY OF SPECIAL BLEACHES



turning dark after processing. If the plate is soaked in mercuric chloride ( $\text{HgCl}_2$ ) bleach for 5 min as a final step and not washed afterwards, the plate remains clear. Because of the extremely poisonous nature of  $\text{HgCl}_2$ , this is not a desirable treatment. We found that soaking in copper bromide ( $\text{CuBr}_2$ ) or copper chloride ( $\text{CuCl}_2$ ) also prevents the plate from turning dark.

Besides the chromate-type bleaches, several others were found to improve the diffraction efficiency. Among these the potassium ferrocyanide ( $\text{K}_3\text{Fe}(\text{CN})_6$ ), copper bromide and hydrogen peroxide ( $\text{CuBr}_2 + \text{H}_2\text{O}_2$ ), and potassium bromide with potassium ferrocyanide ( $\text{KBr} + \text{K}_3\text{Fe}(\text{CN})_6$ ) were some that were quite good. The first two do not cause the plate to become more opaque with exposure to light or air, and the  $\text{K}_3\text{Fe}(\text{CN})_6$  by itself produces a very stable compound. The maximum measured diffraction efficiencies of the above three compounds were 39%, 37%, and 34%, respectively. The bleach containing hydrogen peroxide is difficult to use because oxygen bubbles tend to form inside the emulsion and tear it away from the base. This effect can be reduced if a low concentration of  $\text{H}_2\text{O}_2$  is used (1% solution) and bleaching time does not exceed 10 min.

### 3.3. MEASUREMENT OF DIFFRACTION EFFICIENCY

The diffraction efficiency as used here is defined to be  $I_{\text{diff}}/I_{\text{inc}}$ , where  $I_{\text{inc}}$  is the intensity of the incident beam of light and  $I_{\text{diff}}$  is the diffracted intensity of light. The plates were replaced in the same position as when exposed (as shown in fig. 7), with one beam blocked and the other collimated. Collimation was used to eliminate dependence of the light meter on distance from the plate and to obtain a more intense beam of light. A YSI-Kettering model 65 radiometer was used to measure light intensity. The plates were always aligned for maximum diffraction efficiency and sometimes required a few degrees rotation relative to their original positions. The readings were corrected for changes in beam width due to rotation of the plate.

In general, it was difficult to obtain repeatable results for a given exposure and process. The main problem seems to be the distortion of the emulsion caused by stresses in the emulsion or the processing. The curves include losses due to surface reflections which could be eliminated by coating the surfaces with antireflection coatings. To obtain diffraction efficiencies with reflection losses removed, the diffraction efficiencies should be multiplied by a factor of 1.23.

### 3.4. LIGHT DISTRIBUTION IN A BLEACHED GRATING

To make further improvements in bleached diffraction gratings, it is important to know the losses that occur in a grating. One grating, bleached in modified R-10 bleach and having a diffraction efficiency of 44%, was examined for losses. The losses were assumed to be caused by absorption in the emulsion, surface reflection, scattering, and transmission through the plate.

The scattered light was estimated by measuring the light intensity at a large distance—compared to the size of the grating—on either side of the plate and perpendicular to it, taking the average, and assuming the scattering to be uniform. If  $I_T$  is the total scattered light intensity and  $I_M$  is the average of two measured values, then  $I_T = I_M \frac{4\pi D^2}{A}$ , where  $D$  is the distance from the grating and  $A$  is the area of the detector. The surface reflection from a single air-glass surface was measured at 9%, and at the second surface the energy loss is estimated at 4%.

The diffracted light and transmitted light were measured directly, and the difference of the measured intensities and the input is assumed to be absorbed. The light distribution for the sample measured is as follows:

Diffraction	44%
Transmitted light	8%
Surface reflections	13%
Scattered light	9%
Absorbed light	26%

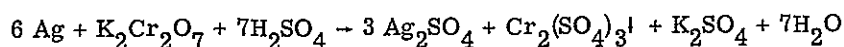
### 3.5. CHEMICAL REACTIONS IN BLEACHING

The chemical compounds that are produced in the bleaching process are of interest, since the knowledge of these helps in the understanding of the bleaching process and helps in finding bleaches that have more desirable properties. Some chemical reactions were found in the literature, while others were assumed to take place but may not be correct. Several of the bleaches are discussed here.

The mercuric chloride bleaching process has been described by R. W. Green [12]. The reaction was described as  $\text{Ag} + \text{HgCl}_2 \rightarrow \text{AgHgCl}_2 \cdot x\text{H}_2\text{O}$ . The plate has a tendency to turn dark with exposure to light, indicating that it decomposes into free silver or mercury. If some  $\text{HgCl}_2$  is left in the emulsion, the bleach is more stable.

Bleaches containing chromates gave the best results, and these were studied in more detail. Pure silver particles were treated with various bleaches, but only the KCIB reacted with the silver in bulk form. The characteristic brownish color was not produced and the only precipitated product seemed to be silver chloride ( $\text{AgCl}$ ). The clearing bath (part B of KCIB) of the Kodak bleach did not react with this precipitate and apparently reacts with other deposits in the emulsion.

One reaction produced by bleaching with a chromate bleach [13] is



Only chromium sulphate ( $\text{Cr}_2(\text{SO}_4)_3$ ) remains in the emulsion. The diffraction efficiency of this bleach is low. This is probably because of the low refractive index of  $\text{Cr}_2(\text{SO}_4)_3$ , but it also

may be because of the low ratio of chromium molecules to silver atoms (1:6), and possibly the formation of  $\text{Cr}_2(\text{SO}_4)_3$  molecules away from silver atoms.

It appears that most of the good bleaches contain chlorine or bromide to form AgCl or silver bromide (AgBr) in the emulsion, which usually give high diffraction efficiencies. In the Kodak R-10 bleach, the probable reaction products remaining in the emulsion are  $\text{Cr}_2(\text{SO}_4)_3$  and AgCl, but the AgCl seems to have more effect. The most efficient chromate bleaches apparently leave AgCl and chromium chloride ( $\text{CrCl}_3$ ) in the emulsion.

Two bleaches were found that do not contain chromium or chloride and still have rather high diffraction efficiency. One of these is potassium ferrocyanide  $\text{K}_3\text{Fe}(\text{CN})_6$ , which probably forms either  $\text{AgK}_3\text{Fe}(\text{CN})_6$  or  $\text{Ag}_4\text{Fe}(\text{CN})_6$  in the bleaching process. The resulting compound is very stable, reasonably transparent at red wavelengths, and gives a maximum efficiency of 39%. The other bleach contained copper bromide  $\text{CuBr}_2$  and hydrogen peroxide  $\text{H}_2\text{O}_2$ , which is believed to form two compounds, AgBr and copper oxide ( $\text{Cu}_2\text{O}$ ) in the emulsion. Both of these have high indexes of refraction, 2.25 and 2.70, respectively. The bleached plate has a light brownish color. It can be further processed by washing it in KCIB clearing bath, which turns it white, and then soaked in  $\text{HgCl}_2$  to stabilize the compound. Since the composition of the clearing bath is unknown, the final compounds in the bleached plate are also unknown. Many other chemical compounds are known to have high indexes of refraction, some of which are listed in table I.

### 3.6. DISCUSSION

The conversion of silver grains into transparent salt is a process dependent on many factors not well understood. The efficiency of the bleached grating likewise depends on many factors, including the handling of the exposed plates in the bleaching process, stability of optical systems during exposure, relative amplitude of the two interfering beams, and distortions in the emulsion. Because of these factors, it is difficult to repeat experiments, and slight variations in efficiencies usually exist between gratings prepared in a similar manner. The graphs were drawn using the best efficiencies for each exposure.

None of the bleaches that we have investigated possesses all the desired properties. The two most serious shortcomings are that the bleached plates still absorb light and that they tend to turn dark with exposure to light. Fixing apparently removes compounds responsible for index-of-refraction changes and, therefore, plates are not fixed after bleaching. The index-of-refraction changes also are not sufficiently high. Treatment with HgCl solution after bleaching and clearing seems to prevent darkening of the gratings.

Other bleaches were tried. Good results were obtained with Kodak In-4 intensifier bleach. Up to an optical density of 2.8, it follows the Kodak bleach, at which point it flattens out with a

TABLE I. CHEMICAL COMPOUNDS WITH A HIGH INDEX OF REFRACTION

Compound	Index of Refraction	Color of Bulk Compound
AgCl	2.071	White
AgI	2.21	Yellow
AgBr	2.253	Pale yellow
HgO	2.37	Yellow or red
Hg <sub>2</sub> Cl <sub>2</sub>	1.97	White
Hg <sub>2</sub> Cl <sub>2</sub> · 2H <sub>2</sub> O	2.35	
HgCl <sub>2</sub>	1.859	Colorless
CuO	2.63	
Cu <sub>2</sub> O	2.705	Red
Cu <sub>2</sub> O <sub>3</sub>	2.5	Green
CuBr	2.160	White
HgI	2.75	Red
SrS	2.11	Colorless or light gray
TlCl	2.25	White
Tl I	2.78	Yellow or red
SnI <sub>4</sub>	2.106	Orange-red
Al <sub>4</sub> C <sub>3</sub>	2.7	Yellow-green
SbI <sub>3</sub>	2.78	Ruby-red
BaO	1.98	Colorless or white-yellowish powder
BaS	2.16	Colorless
CdO	2.49	Brown
CdS	2.506	Yellow-orange
Cr <sub>2</sub> (SO <sub>4</sub> )	Unknown	Unknown
CrCl <sub>3</sub> · xH <sub>2</sub> O	Unknown	Unknown

maximum efficiency of about 33%. Another bleach (not standard) used KBr and  $K_3Fe(CN)_6$  and gave an efficiency curve that behaved like modified R-10 with KBr up to an efficiency of 30%, at which point it leveled out, reaching a maximum of 35%.

Different developers were also tried: D-19 and HRP gave equally good results, while Dektal and D-8 showed a decline in efficiencies. The results given here are for a Kodak D-19 developer.

Several bleaches are available which would give diffraction efficiencies in the range of 35% to 48%. This variable represents about one-half f-stop change and, in ordinary photography, would be considered insignificant. Within this range, diffraction gratings or similar optical elements could be made quite easily. Some difficulty is expected in obtaining uniform diffraction efficiencies over larger areas of film since the emulsion tends to get distorted. Without surface reflections, the best efficiency achieved would be 60%.

The many problems and unanswered questions concerning bleaching provide a challenging project for a chemist or a thesis project for a chemistry student.

### 3.7. CHEMICAL REACTIONS AND BLEACHING PROCEDURES

#### 3.7.1. KODAK CHROMIUM INTENSIFIER BLEACH

Chemical Reaction:  $Ag^+ + 4Cl^- + Cr^{+++} \rightarrow AgCl \downarrow + CrCl_3 \downarrow$

The chemical compositions of the bleach and the clearing bath are unknown; therefore, the chemical reaction is not definitely known.

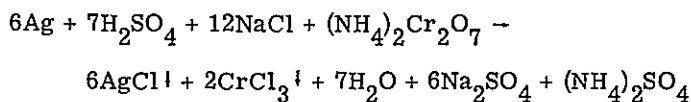
Procedure:

- (1) Mix bleach and clearing bath according to manufacturer's instructions.
- (2) Bleach for 1 min after the silver image has been removed (approximately 3 to 5 min).  
Agitate.
- (3) Rinse 0.5 min in running water.
- (4) Soak in clearing bath (part B) until exposed emulsion becomes white, for about 5 to 20 min. Use occasional agitation.
- (5) Wash in running water 5 to 10 min.
- (6) Soak 5 min in Photo-Flo and  $CuCl_2$  solution.
- (7) Dry without washing.

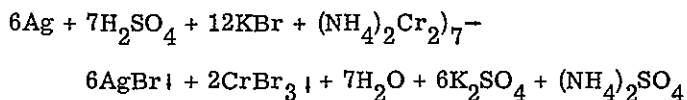
#### 3.7.2. KODAK R-10 BLEACH AND MODIFIED R-10 BLEACHES.

Chemical Reactions:

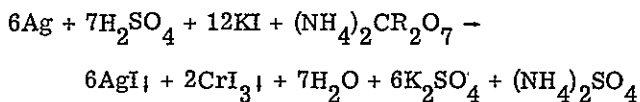
- (1) Standard R-10 bleach with NaCl in solution B:



- (2) Modified R-10 bleach with KBr in solution B:



- (3) Modified R-10 bleach with KI in solution B:



Composition of bleaching solutions [14]:

Stock Solution A

Distilled water	500 ml
Ammonium bichromate	20 g
Concentrated sulfuric acid	14 ml
Distilled water to make	1000 ml

Stock Solution B

Sodium chloride	45 g
Distilled water to make	1000 ml

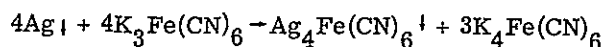
For the bromide or iodate modifications, 92 g potassium bromide or 128 g potassium iodate instead of the sodium chloride was used in solution B. The NaCl in solution B was also replaced with NaF, but the effect was to remove emulsion without bleaching the silver. For use, mix 1 part A to 1 part B to 10 parts water.

Procedure:

- (1) Bleach for 1 min more than required for the removal of the silver (3 to 5 min). Agitate.
- (2) Rinse in running water, soak 1 min in CB-6 (clearing bath), and wash (approximately 5 min).
- (3) Soak for 5 min in respective cupric halogen ( $\text{CuCl}_2$ ,  $\text{CuBr}_2$ , etc.), which also has Photo-Flo in it. The cupric halogen solutions contained 5 g of cupric halogen per 100 ml of water.
- (4) Dry without washing.

### 3.7.3. POTASSIUM FERRICYANIDE BLEACH

Chemical Reaction:  $\text{Ag}\downarrow + \text{K}_3\text{Fe}(\text{CN})_6 \rightarrow \text{AgK}_3\text{Fe}(\text{CN})_6\downarrow$  or



Procedure:

- (1) Bleach for 4 min in 15 g of  $K_3Fe(CN)_6$  per 1000 ml of water.
- (2) Wash for 15 min in running water.
- (3) Soak in print flattening solution for 5 min.

#### 3.7.4. COPPER BROMIDE BLEACH

Chemical Reaction:  $4Ag\downarrow + CuBr_2 + H_2O_2 \rightarrow 4AgBr\downarrow + Cu_2O\downarrow + H_2O$

Note: the copper may also form  $CuO$  or  $CuO_2$  salt.

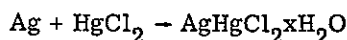
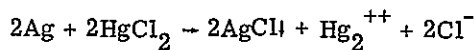
Procedure:

- (1) Mix a solution in the proportions of 40 ml of 15 g of  $CuBr_2$  per 1000 ml of water solution with 60 ml of diluted hydrogen peroxide (1 part of 3% hydrogen peroxide with 2 parts of water). Mix the two solutions immediately before use because  $O_2$  is liberated from the mixed solution:  $2H_2O_2 \rightarrow 2H_2O + O_2$  in presence of  $CuBr_2$ .
- (2) Bleach the plate until exposed emulsion turns brownish, but not longer than 10 min. Continuously brush off bubbles forming on top of the emulsion.
- (3) Wash plate for 15 min in running water.
- (4) Rinse in Photo-Flow and dry emulsion, or continue with the following steps which make the plate more transparent and improve the efficiency somewhat.
- (5) Soak the plate for 8 min in KCIB, part B, the clearing bath.
- (6) Wash for 5 min.
- (7) Soak the plate in  $HgCl$  solution for 2 min.
- (8) Dry without washing.

Note: The  $H_2O_2$  has a tendency to decompose thus forming oxygen bubbles inside the emulsion, and, in some cases, the emulsion will peel off. For this reason, the concentration of the bleach should not be stronger than indicated above, and the bleaching time should not exceed 10 min.

#### 3.7.5. MERCURIC CHLORIDE BLEACH

Chemical Reaction:



Procedure:

- (1) Bleach 3 to 5 min or 1 min after dark silver image has disappeared.
- (2) Wash for 4 min, Photo-Flo rinse, and dry.

## 4.1. INTRODUCTION

The two-frequency method has been used successfully to generate constant range contours on or near holographic images [15]. One such method for obtaining the desired contours is to construct a hologram of an object at one wavelength  $\lambda_1$ ; then the hologram, as well as the object, is illuminated with a different wavelength  $\lambda_2$ . By carefully positioning the holographic image in near coincidence with the object, an interference pattern results which is comprised of contours denoting constant depth. One problem with the above procedure is that the holographic image becomes translated, rotated, and distorted when the reconstruction wavelength differs from the construction wavelength. Consequently, contours can often be produced only on a relatively small portion of the object surface. However, this problem can be greatly alleviated by appropriately modifying the geometry for constructing the required hologram.

Consider a small portion of a hologram constructed with a collimated reference of wavelength  $\lambda_1$  and then interrogated with a collimated beam of wavelength  $\lambda_2$ . Each point of the object at a distance  $R_1$  from a small hologram is imaged at a distance  $R'_1$  such that

$$R'_1 = \frac{\lambda_1}{\lambda_2} R_1 \quad (16)$$

Thus, to minimize the relative change from the object to the corresponding image position, the object-to-hologram distance should be as small as possible. If plane-wave reference and readout beams are used, this condition can be relaxed considerably by utilizing only the object-to-hologram rays which are nearly longitudinal. Then the displacement of the image of the hologram is in a direction having the least effect on the range contours.

We shall now present a practical method for generating range contours over large surfaces. Often one to two orders of magnitude improvement can easily be obtained for a given wavelength ratio. Furthermore, by properly using both collimated reference and illuminating beams, we can obtain contour surfaces denoting equidistant planes parallel to the hologram.\* These surfaces are generally much easier to interpret than the ellipsoids obtained by previous techniques.

---

\*Plane contour surfaces can be obtained using techniques previously reported, for example, by requiring all beams to be collimated and then viewing the reconstruction with a telescope. However, the maximum object slope over which contours can be thus recorded is considerably less than that obtainable with techniques described below.



#### 4.2. THEORY

Rather than attempting to place the object very near to a hologram (e.g., by illuminating the object from the back side of a hologram), we image an exact replica of the object near the hologram by utilizing an imaging system. Consider the unit telescope system shown in figure 11. This telescope performs two basic functions. First, it produces an image I of the object O such that a hologram can easily be constructed in a plane which passes near or actually through the image. Second, its aperture A restricts the image-forming rays to be nearly longitudinal.

To obtain contour fringes of the diffuse object O, we first construct a hologram H located very near to the image I with wavelength  $\lambda_1$ . Then the hologram and the object are illuminated with a new wavelength  $\lambda_2$ . By carefully positioning the image of the hologram in near coincidence with the image of the telescope, an interference pattern results denoting constant range contours. If a collimated reference beam is used to construct the hologram, the appropriate reconstructing beam is also a collimated beam but of slightly different orientation than the reference beam. In particular, we require that the directions of the reconstructing beam  $\alpha_c$  and the reference beam  $\alpha_r$  satisfy the following relationship:

$$\sin \alpha_c = \frac{\lambda_2}{\lambda_1} \sin \alpha_r \quad (17)$$

Let us now consider minimum requirements for the formation of contour fringes on or near the image of the hologram. It is well known that contour fringes occur due to interference effects between two images. Therefore, the lateral and longitudinal displacements of the reconstructed image should be less than the resolution and depth of focus of the viewing system, respectively. However, we restrict either the imaging system or the subsequent viewing system to small viewing angles relative to their axes. Thus, no appreciable lateral displacements result, and only longitudinal displacements need to be considered.

The resolution, depth of focus, and viewing angle are, respectively,

$$\rho = \frac{\lambda}{\theta} = \lambda \frac{f}{d} \quad (18)$$

$$\Delta Z = 4 \frac{\lambda}{\theta^2} = 4 \lambda \left( \frac{f}{d} \right)^2 \quad (19)$$

$$\theta = \frac{d}{f} \quad (20)$$

where  $\lambda$  denotes the wavelength,  $f$  the focal length of each lens, and  $d$  the diameter of the aperture A. According to equation 16, the longitudinal displacement of the image of the hologram is

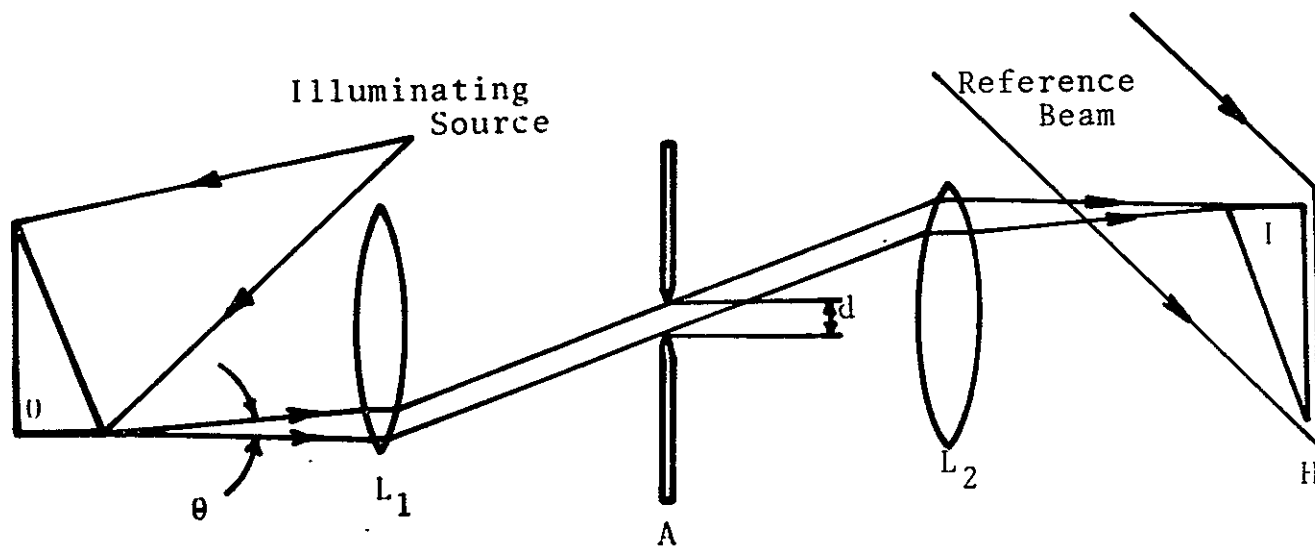


FIGURE 11. A SYSTEM FOR GENERATING CONTOURS OVER LARGE SURFACES

$$z'_1 - z_1 = \frac{\lambda_1 - \lambda_2}{\lambda_2} z_1 \approx \frac{\Delta\lambda}{\lambda} z_1 \quad (21)$$

where

$$\Delta\lambda = \lambda_1 - \lambda_2$$

and

$$\lambda_1 \approx \lambda = \frac{\lambda_1 + \lambda_2}{2} \approx \lambda_2$$

The above discussion on interference requires the following necessary condition:

$$|z'_1 - z_1| \leq \Delta Z \quad (22)$$

After substituting (19) and (21) into (22), we find the following constraint on the longitudinal distance from the hologram to its reconstructed image

$$|z_1| \leq \frac{4\lambda^2}{|\Delta\lambda|\theta^2} = \frac{4\lambda^2}{|\Delta\lambda|} \left(\frac{f}{d}\right)^2 \quad (23)$$

Of course, if the entire image is to be recorded, its longitudinal extent must be less than the depth of focus associated with the recorder. Thus, we usually need the more stringent condition

$$|z_1| \leq \frac{\Delta Z}{2} = 2\lambda/\theta^2 = 2\lambda \left(\frac{f}{d}\right)^2 \quad (24)$$

Let us now consider the light intensity which results when the image of the hologram and that of the imaging system are made to interfere. Assume that the two image intensities are equal. It is convenient to define a rectangular coordinate system having its z-axis normal to the hologram and the elements of the imaging system while the x- and y-axes are in the plane of the hologram. A point source located at  $(x_s, 0, z_s)$  illuminates the object. The desired image intensity of an arbitrary object point  $(x_0, y_0, z_0)$  is then given by

$$I' = 2I \left( 1 + b \cos \left\{ (k_1 - k_2)z_0 + (k_1 - k_2) \left[ (z_0 - z_s)^2 + (x_0 - x_s)^2 + y_0^2 \right]^{1/2} + \beta \right\} \right) \quad (25)$$

where  $I$  denotes the image intensity in the absence of the reconstruction of the hologram;  $b$  is some real constant between 0 and 1, depending upon the amount of image displacement associated with the holographic image;  $k_1$  and  $k_2$  are the wave numbers corresponding to  $\lambda_1$  and  $\lambda_2$ ; and  $\beta$  is an unknown constant phase. According to (25), the contour maxima occur when

$$z_0 + \left[ (z_0 - z_s)^2 + (x_0 - x_s)^2 + y_0^2 \right]^{1/2} = \frac{\lambda_1 \lambda_2}{|\Delta \lambda|} \left( n - \frac{\beta}{2\pi} \right) \quad (26)$$

for integer values of  $n$ .

Equation 26 denotes a set of paraboloids of revolution about the line  $(x - x_s, y = 0)$  with vertices at  $\left( x_s, 0, \frac{1}{2} z_s \right) + \frac{\lambda_1 \lambda_2}{|\Delta \lambda|} \left( n - \frac{\beta}{2\pi} \right)$ . However, we are interested in generating plane contour surfaces. Such surfaces can easily be obtained by merely letting  $|z_s|$  get very large. More specifically, equation 26 becomes

$$z_0 = n_2 \frac{\lambda_1 \lambda_2}{|\Delta \lambda|} + \text{constant} \quad (27)$$

provided that

$$\frac{(2|x_s| + |x_0|)^2 + y_0^2}{|z_s - z_0|} \leq 2 \frac{\lambda_1 \lambda_2}{\Delta \lambda} \quad (28)$$

where the lateral extent of the object is bounded by

$$|x_0| \leq \frac{x_0}{2}$$

and

$$|y_0| \leq \frac{y_0}{2}$$

Inequality 28 was obtained by requiring the resulting phase error to be bounded by  $\pm\pi/4$  radians. Plane contour surfaces can be obtained with the setup shown in figure 11 by merely replacing the point-source illuminator with a collimated one oriented along the  $z$ -axis. This can easily be done by incorporating a beam splitter between the object  $O$  and the objective lens  $L_1$  to reflect a collimated wave onto the object.

As the angle between the normals of the hologram and the object is increased, the frequency of the contour fringes increases. The object orientation for which the contour fringes become indistinguishable will now be determined. Referring to the object shown in figure 12, we observe that separate contour fringes are imaged provided that

$$\tan |\phi| \leq \frac{\lambda_1 \lambda_2}{2|\Delta \lambda| \rho} \approx \frac{\lambda^2}{2|\Delta \lambda| \rho} \approx \frac{\lambda \theta}{2|\Delta \lambda|} \quad (29)$$

Combining (23) and (29) to eliminate  $\theta$  yields

$$|z_1| (\tan \phi)^2 \leq \frac{\lambda^4}{|\Delta \lambda|^3} \quad (30)$$

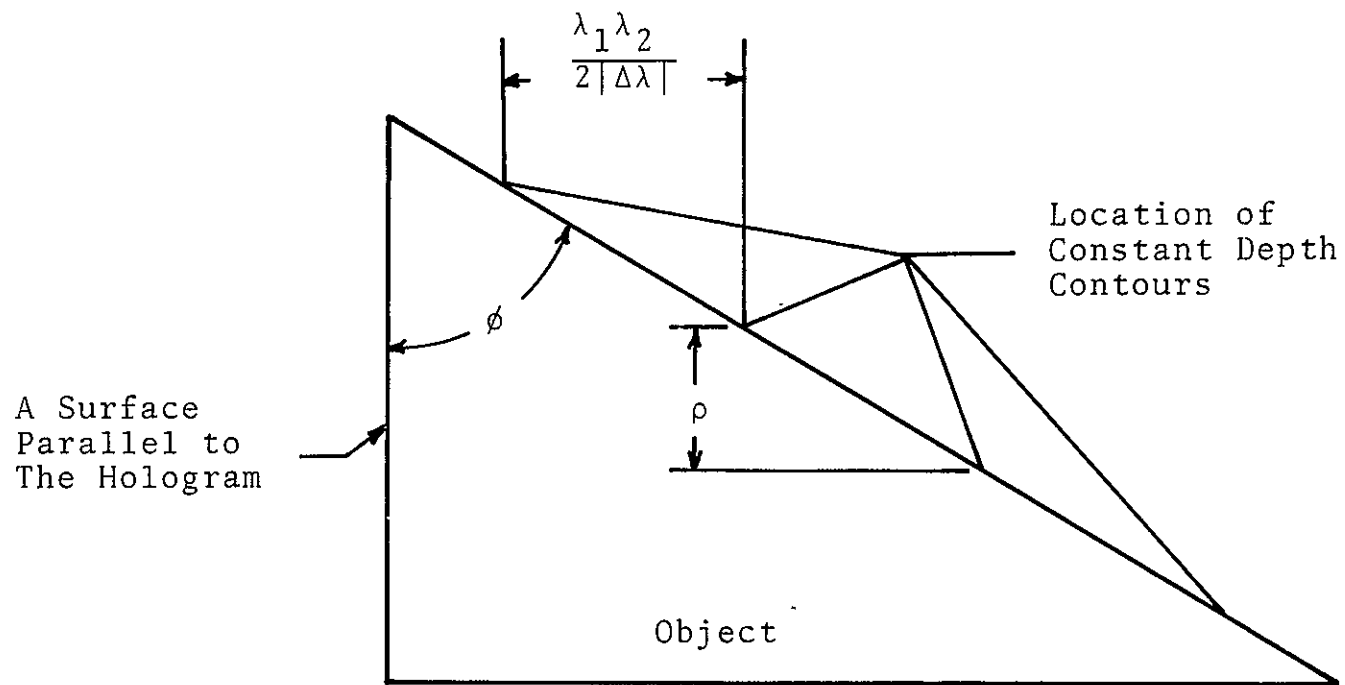


FIGURE 12. AN INCLINED SURFACE OF THE OBJECT

This important result shows that contours can, in theory, be generated over surfaces of arbitrary large lateral extent. The maximum allowable inclination of the object is determined by the position of the object as well as the two wavelengths which are used.

Practical limitations actually require that the right side of inequality 30 be greatly reduced. As previously noted, if the entire object is to be recorded, the allowable range of  $z_1$  values must be reduced by a factor  $|\Delta\lambda|/\lambda$ . Furthermore, if good fringe contrast is to be obtained, still greater reduction in the extent is required. Consequently, inequality 28 becomes after practical considerations

$$|z_1|(\tan \phi)^2 \leq \frac{\lambda^3}{2(\Delta\lambda)^2} \quad (31)$$

Clearly, there is nothing unique about the imaging system shown in figure 11. In fact, a lensless system can be implemented by employing holographic techniques. Consider a doubly exposed hologram constructed by sequentially exposing a photographic plate to two different wavelengths, say  $\lambda_1$  and  $\lambda_2$ . Rotating either the reference beam or the hologram between exposures allows us to read out the images separately. First, the exposure made with wavelength  $\lambda_1$  is read out with a  $\lambda_1$  beam to form a real image in the original object space. This image is then recorded by a second hologram situated in the original object position. Next, the second exposure of the first hologram is read out with wavelength  $\lambda_2$ . Simultaneously, the hologram constructed in the object plane is read out with the appropriate  $\lambda_2$  beam to form the desired contour fringes. Clearly, such a doubly exposed hologram duplicates the task performed by the unit telescope of figure 11, except for the aperture A which restricts the image-forming rays to being nearly longitudinal. However, such an aperture can be incorporated into the subsequent recording or viewing system. It should be noted that the holographic imaging system just described causes two pseudoscopic rather than orthoscopic images to interfere, but no noticeable change in the recorded image and accompanying depth-contours results.

The final contouring system which we consider requires one large lens and one large photographic plate. Consider two small holograms constructed at the aperture plane A of figure 11, with respective wavelengths  $\lambda_1$  and  $\lambda_2$ . Now by illuminating the two holograms with beams which are conjugate to the original constructing reference beams, images at both wavelengths  $\lambda_1$  and  $\lambda_2$  can be generated at the original object position. One of these images can be used to construct a third hologram in a plane near the original position. The image of this third hologram can then be made to interfere with the image of the other hologram recorded at plane A. In essence, the system just described uses one lens for both the objective and the eyepiece lenses of a unit telescope, except for the fact that pseudoscopic images are formed. The size of the frequency-plane aperture A is determined by the extent of the holograms constructed there.

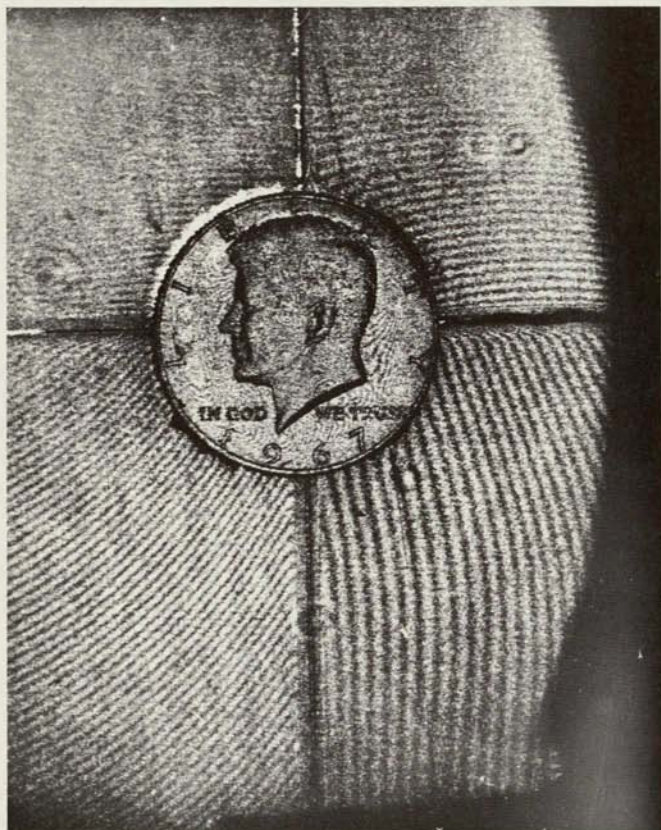


FIGURE 13. DEPTH CONTOURS ON FOUR FLAT SURFACES

#### 4.3. EXPERIMENTAL RESULTS

The system shown in figure 11 has been used to generate constant depth contours. A Spectra Physics model 125 helium neon (He-Ne) laser capable of generating both a red line ( $\lambda_1 = 6328\text{\AA}$ ) and an orange line ( $\lambda_2 = 6118\text{\AA}$ ) was used. Thus, consecutive contour fringes denote a depth separation of

$$\frac{\lambda_1 \lambda_2}{2 |\Delta \lambda|} = 9.25 \text{ } \mu\text{m}$$

The object used is comprised of four flat surfaces, each of slightly different angular orientation, and a fifty-cent coin. The lateral extent of the object on which we were able to record fringes was about 10 cm by 8 cm. Actually, the lateral dimensions over which we could obtain depth contours—as the above theory predicts—was only limited by the useful apertures of the lenses used to image the object and those required to collimate the illuminating and reference beams.

Figure 13 is a result obtained by using a telescope having a demagnification of 2 and a viewing angle  $\theta$  of about 1/50 rad. The depth contours can be seen on the four flat surfaces as well as the coin. The curvature associated with the contours located at the extremities of the photograph is primarily attributed to aberrations introduced by our collimating lens.

#### 4.4. CONCLUSIONS

We have shown that two-frequency range (depth) contours can be formed over areas considerably larger than were previously possible. This is accomplished by using an imaging system so that the required hologram can be constructed arbitrarily close to the resulting image. Additional improvement is obtained by using only the imaging rays which are nearly longitudinal. Working with plane-wave sources, it is possible to form contour surfaces which are plane and equidistant from the hologram.

The contouring techniques which we have described are not limited to optical wavelengths. Clearly other electromagnetic wavelengths, as well as acoustical sources, could be used. Generally, the required imaging system does not have to be of very high quality, providing that it functions the same way at both the wavelengths which are used. The basic result given in this report is that the lateral extent over which range contours can be obtained is only limited by the longitudinal extent of the object surface and by its maximum slope.

#### 5.1. INTRODUCTION

We have investigated the use of holographic interferometry to study phenomena related to the measurement of refractive index of transparent media. The principle underlying this



important application of holography is that the wavefront emanating from a coherently illuminated object can be holographically reconstructed so precisely that it is optically indistinguishable from the actual wavefront from the object. The actual and reconstructed wavefronts can, therefore, be interfered with each other. If the object is transparent, this allows sensitive detection of changes of optical path length through the object, whether due to displacement of the object or changes in its index of refraction. Similarly, two reconstructed wavefronts can be interfered with each other. This is most readily accomplished by superimposing on one hologram the wavefronts emanating from the object at two different times. The image reconstructed from this hologram contains a fringe pattern characteristic of any change in the optical path length through the object with respect to that at the time of the first recording. This latter technique was used in most of the experiments reported here.

We have concentrated on the detection of optical path length changes which are due solely to refractive index variation. The use of holographic interferometry to measure the refractive index of homogeneous media has been explored, and an investigation of its application to heat and mass transfer and related fields has been initiated.

## 5.2. BASIC APPARATUS AND PROCEDURE

The apparatus of figure 14 can be utilized for interferometry in real time or for interferometry by dual exposure. The procedure for real-time interferometry is as follows: The photographic plate is exposed simultaneously to the reference beam and to the object beam, which has passed through the undisturbed transparent test object. When the developed photographic plate is replaced in its original position, the wavefront which emanated from the undisturbed object can be reconstructed by illuminating the film with the reference beam. If the object beam is also turned on, it will interfere with the reconstructed object beam; hence, if the test object is disturbed by displacing it or changing its refractive index, fringe patterns are observed. In this manner, real-time differential interferometry can be performed.

Differential interferometry by dual exposure is a similar process. In this case, two holograms are produced on the same photographic plate—one of the undisturbed test object and one of the disturbed test object. When this plate is developed and illuminated by the reference beam, the two wavefronts are simultaneously reconstructed and the resulting interference pattern is readily observed.

In certain phases of the investigation, holographic interferometry was performed with a phase structure, such as a diffusing screen, placed between the collimating lens and the object. This gave rise to fringe localization phenomena of great interest and possible application, which are described below.

Experiments involving the measurement of refractive index and application to the study of natural convection heat transfer are described in the following sections.

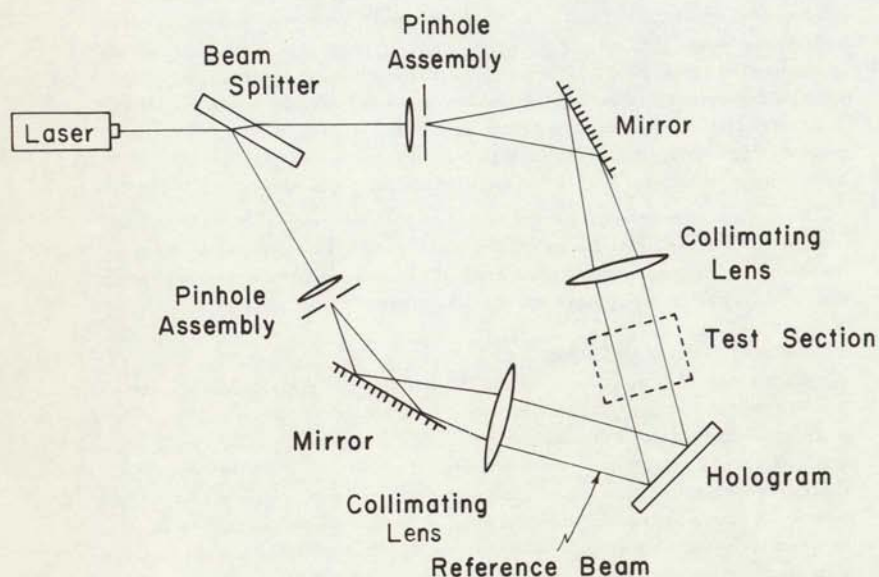


FIGURE 14. EXPERIMENTAL SETUP FOR HOLOGRAM INTERFEROMETRY OF TRANSPARENT MEDIA

### 5.3. MEASUREMENT OF INDEX OF REFRACTION OF HOMOGENEOUS MEDIA

Conventional interferometric techniques for determining the refractive index of transparent objects entail considerable experimental difficulty. Generally, these techniques involve the comparison of optical paths in the two legs of a two-beam interferometer. For the case of liquid or gaseous substances, each leg must include a transparent container—for the substance of unknown refractive index in one leg and for the standard substance to which it is to be compared in the other. It is essential that the two paths be identical in the absence of the unknown and standard fluids. This requires precision alignment and high optical quality of all components, including the containers. Once these conditions are satisfied, the resulting interference pattern provides an accurate measurement of the difference in optical path length between the two beams due to the presence of the test and standard fluids. The refractive index can then be computed.

The use of holographic interferometry preserves the accuracy and sensitivity of the conventional techniques, but substantially alleviates much of their experimental complexity. This is true because the instrument is effectively a one-path interferometer.

The holographic apparatus used in this experiment is the same as that of figure 14, except the collimating lens is removed from the object beam. Hence, the hologram is the recorded interference pattern between a spherical object beam and a plane reference beam. The test object in this case is a transparent container for the liquid whose refractive index is to be determined. This container need not be of high optical quality; in fact, the one used in this experiment was made of plexiglas.

5.3.1. ANALYSIS. Let  $O$  denote the wavefront of the object beam which emanates from a monochromatic point source at  $(x_1, y_1, z_1)$ . Let  $r$  denote the plane wavefront of the reference beam which impinges on the hologram at an angle  $\theta$ . The interference of these wavefronts results in an intensity distribution at the hologram plane given by

$$I = |O + r|^2 = |O|^2 + |r|^2 + O^*r + Or^*$$

where an asterisk denotes a complex conjugate.

This intensity is recorded on a photographic plate which is then developed such that its amplitude transmission at any point is proportional to  $I$ . When this hologram is illuminated with a monochromatic beam of wavefront  $C$ , a wavefront  $H$ , therefore, emerges from the hologram and is represented by

$$H = C(|O|^2 + |r|^2 + O^*r + Or^*)$$

The first two terms within the parentheses represent the zero-order images and are of no interest in the present applications. The last two terms represent the first-order images. Attention is focused on the virtual images  $Or^*C$ .

Let the coordinate system be located such that the hologram is in the  $(x, y, 0)$  plane. For simplicity, it is assumed that reference and signal-beam intensities are constant across the hologram, and also that the plane wave  $C$  used for reconstruction is identical to  $r$ . The resulting virtual image, which is a replica of the object wavefront, is represented by

$$K e^{j \frac{2\pi}{\lambda} [(x-x_1)^2 + (y-y_1)^2 + z_1^2]}$$

where  $K$  is a constant amplitude term and where the phases of the reference and reconstructing beams cancel each other.

Now suppose that a plane, parallel, and homogeneous transparent object such as a flat glass plate or a rectangular vessel containing a fluid is placed in the object beam. If the object is perpendicular to the beam, the point source will appear to have been displaced in the axial direction (see fig. 15). The resulting wavefront appears to emanate from a point source at  $(x_1, y_1, z_2)$  and is represented by

$$A_2 e^{j \frac{2\pi}{\lambda} [(x-x_1)^2 + (y-y_1)^2 + z_2^2]}$$

The interference of this wave with the reconstruction of the original object beam produces a Fresnel zone pattern of concentric circular fringes. When a first-order analysis is performed with  $x_1$  and  $y_1$  taken to be zero, the radius of the  $m$ th fringe in the observation plane is found to be

$$\rho_m = \sqrt{(x^2 + y^2)_m} = \sqrt{\frac{z_1 z_2}{z_1 + z_2}} \cdot \sqrt{2m\lambda}$$

where  $\lambda$  is the illumination wavelength.

Since  $z_1$  can be measured, the above relation can be used to determine  $\Delta z = z_1 - z_2$ . It is known that

$$\Delta z = nt$$

where  $n$  is the index of refraction of the object and  $t$  is its thickness; hence, if either of these quantities is known, the other can be determined readily.

**5.3.2. EXPERIMENTAL RESULTS.** Experiments were conducted to verify the analysis presented in the previous section. Typical results for both dual-exposure and real-time interferometry are shown in figures 16 through 18. The object was a transparent rectangular vessel whose parallel faces were normal to the object beam. In some cases, it was empty. Figure 16 is a photograph of the reconstructed wavefront from a dual-exposure hologram. The first exposure was made with no vessel in the object beam and the second exposure with the vessel in place. The expected Fresnel zone pattern is clearly evident.



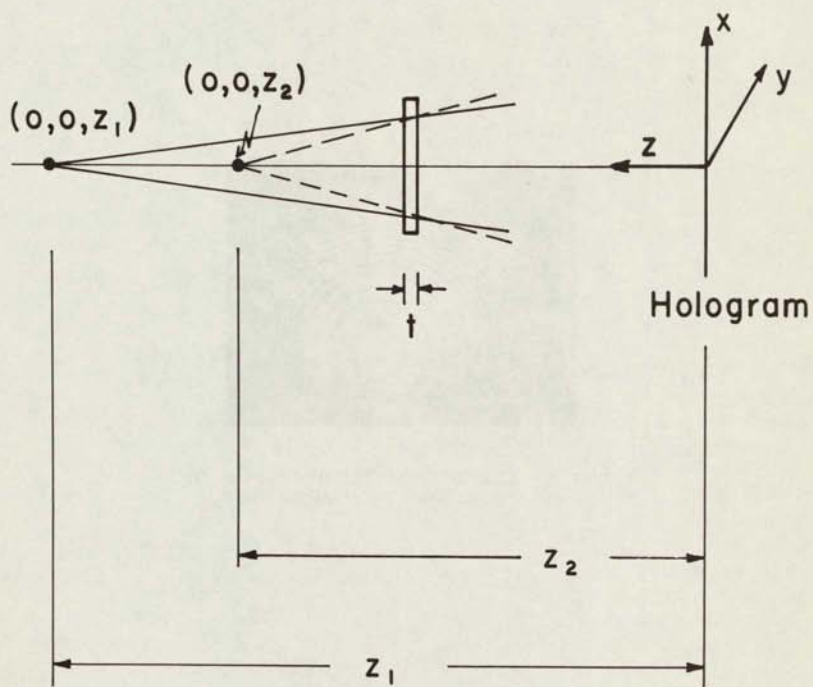


FIGURE 15. EFFECT OF PLACING A PLANE PARALLEL OBJECT IN THE BEAM



FIGURE 16. DUAL-EXPOSURE INTERFEROGRAM FOR  
INDEX-OF-REFRACTION MEASUREMENT



(a) Effect of Emulsion Distortion

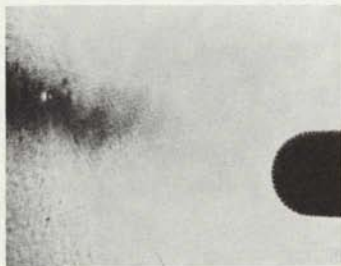


(b) Recording of Hologram with No Object.  
During Reconstruction, Object Inserted.



(c) Recording of Hologram with Object in Place.  
During Reconstruction, Object Removed.

FIGURE 17. REAL-TIME INTERFEROGRAMS FOR INDEX-  
OF-REFRACTION MEASUREMENT



(a) Effect of Emulsion Distortion



(b) Recording of Hologram with Object in Place.  
During Reconstruction, Object Removed.



(c) Object Illuminating Source Moved to Null Position

FIGURE 18. REAL-TIME INTERFEROMETRY FOR INDEX-  
OF-REFRACTION MEASUREMENT—NULLING TECHNIQUE



Analogous results of real-time holography are shown in figure 17. Figure 17a shows the interference of waves from the actual point source with those from its own reconstruction. Although inaccurate positioning of the hologram and distortions of its emulsion caused by the development process made it impossible to achieve a true zero fringe situation, a very low order of fringes was obtained. The vessel was then inserted into the object beam and the resulting fringe pattern is shown in figure 17b. The inverse procedure was also carried out: a hologram was made with the vessel in the object beam. It was then removed during reconstruction. The resulting fringes are shown in figure 17c. As expected, the results of all three holographic procedures are equivalent.

A different technique which allows direct measurement of optical path length changes was also tried. A hologram was constructed with the water-filled vessel in the object beam. After appropriate development, the hologram was returned to its original position. The resulting coarse fringes are shown in figure 18a. The water was then removed from the vessel and the resulting fringes at the observation plane are shown in figure 18b. The point source was then axially displaced by means of a micrometer-driven platform until the fringes were nulled. Although we could not obtain the one fringe situation in figure 18a, a rather low-order fringe pattern was reached (fig. 18c). The displacement gave a direct measurement of  $\Delta z$ , from which the refractive index of the water could readily be calculated. With our relatively crude setup, we were able to achieve 5% accuracy with relative ease. A more sophisticated apparatus could no doubt greatly increase this accuracy.

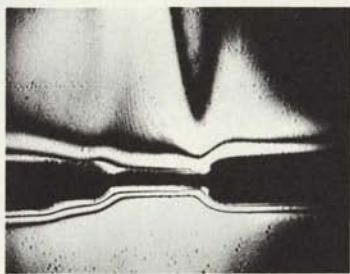
#### 5.4. EXPERIMENTS WITH NONHOMOGENEOUS MEDIA

5.4.1. DIFFERENTIAL INTERFEROMETRY WITH PLANE WAVES. To illustrate the use of holographic interferometry of nonhomogeneous media, we examined the density field of air surrounding heated objects. Two soldering irons, about 5-in. apart, were placed in the object beam of the apparatus shown in figure 14. An exposure was made while the irons were in thermal equilibrium with the ambient. The iron closest to the hologram was then allowed to heat for 5 min and a second exposure was made on the same film plate. The fringe pattern observed upon reconstruction of this dual-exposure hologram is shown in figure 19a. These fringes are nonlocalized; i.e., in focus everywhere. The photograph was made by simply exposing a sheet of polaroid film to the beam emanating from the hologram—no camera was necessary. Similar results were obtained by the real-time procedure. The fringe patterns observed in this case are entirely analogous to those produced by classical interferometers such as the Mach-Zehnder.

A second experiment was carried out in the same manner, except this time both irons were heated simultaneously. The resulting nonlocalized fringes are shown in figure 19b.



(a) One Iron Heated



(b) Both Irons Heated

FIGURE 19. INTERFEROGRAMS OF NATURAL CONVECTION  
IN AIR—PLANE WAVE INTERFEROMETRY

5.4.2. DIFFERENTIAL INTERFEROMETRY WITH DIFFUSED LIGHT. A second group of experiments, like those in section 5.4.1, was carried out, but this time a diffusing screen was placed in the object beam such that the light passing through the object was diffuse. The fringe patterns observed upon reconstruction of the various dual-exposure holograms are shown in figures 20, 21, and 22. These fringes, unlike those discussed in the previous section, are localized at the position of the heated irons. When viewing these holograms, we found it readily apparent that fringe patterns shift as the viewing angle is changed. This localization phenomenon is quite obvious in the sequence of photographs shown.

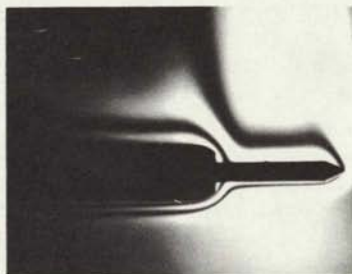
Figure 20a shows the fringes obtained when only the iron farthest from the hologram was heated. Figure 20b shows the analogous fringes when only the iron closest to the hologram was heated. Figures 21a and 21b are two different photographs of the same hologram. In this case, both irons were simultaneously heated. It is obvious that the density field around each iron can be individually visualized—a phenomenon which has no analog in classical interferometry. Finally, figures 22a and 22b are photographs of the reconstruction of a triple-exposure hologram. The first exposure was made with both irons in equilibrium with the ambient. A second exposure was made with only the iron closest to the hologram heated, and later a third exposure was made with only the iron farthest from the hologram heated. Again it is obvious that we can focus on the individual fringe patterns.

## 5.5. EVALUATION

The experimental results indicate that holographic interferometry is a potentially important tool for the measurement of the refractive index of phenomena which manifest themselves as inhomogeneities of transparent materials. Examples of such phenomena are aerodynamic flows, convective heat transfer, mass diffusion, and stress analysis. One of the early dramatic examples of this kind of interferometry applied to transparent media is, of course, the shock-wave patterns of a bullet in flight demonstrated by Brooks, Heflinger, and Wuerker (in Applied Physics Letters, Vol. 7, 1965, p. 92).

Although most of these measurements can be made by classical interferometric methods, the relative ease of setting up and adjusting a holographic interferometer may make it a preferable instrument for many applications. A particularly attractive feature of this method is the elimination of the need for compensating chambers and for test sections of high optical quality in heat transfer and aerodynamic experiments.

The interesting prospect of interferometry with three-dimensional density fields is raised by the fringe localization effects observed when diffuse object beams are used. Evaluation of this prospect, however, awaits further investigation and understanding of the phenomenon.



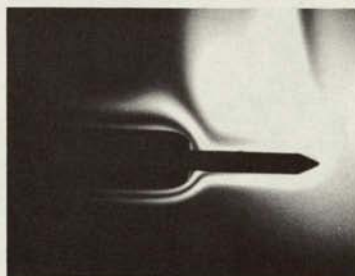
(a) Iron Nearest Hologram Heated



(b) Iron Farthest from Hologram Heated

FIGURE 20. INTERFEROGRAMS OF NATURAL CONVECTION  
IN AIR-DIFFUSE ILLUMINATION INTERFEROMETRY



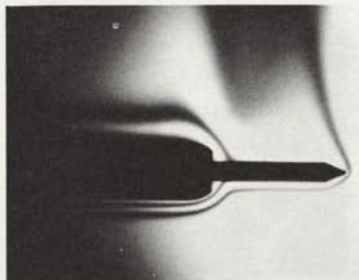


(a) Interferogram of Nearest Iron to Hologram

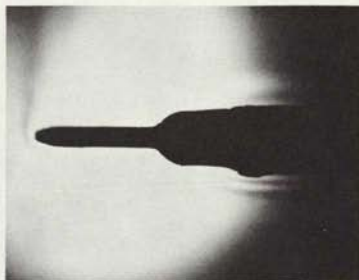


(b) Interferogram of Farthest Iron from Hologram

FIGURE 21. INTERFEROGRAMS OF NATURAL CONVECTION  
IN AIR-DIFFUSE ILLUMINATION INTERFEROMETRY — IRONS  
HEATED SIMULTANEOUSLY



(a) Interferogram of Nearest Iron to Hologram



(b) Interferogram of Farthest Iron from Hologram

FIGURE 22. INTERFEROGRAMS OF NATURAL CONVECTION  
IN AIR-DIFFUSE ILLUMINATION INTERFEROMETRY—IRONS  
HEATED SEPARATELY

### 6.1. INTRODUCTION

It has been repeatedly observed in certain propagation experiments (see fig. 23) at optical frequencies that the first-order distribution of the received wavefront is log-normal. We would like to show the plausibility of this fact and to investigate a method of approximate solution of the wave equation that is suggested by this experimental result.

The log-normal distribution is, of course, directly predicted by the geometric optics and Rytov approximate solutions of the wave equation. (The latter method has recently fallen into some disrepute [16, 17] and, therefore, cannot be considered a reliable predictor.) On the other hand, the Born approximation, of course, amounts to taking only the first two terms of the Neumann series solution. Ignoring convergence questions, the resulting distributions of the scattered wave (as given by the Neumann series) will be quite complicated as the sum of all order products, roughly speaking, of the refractive index field are involved.

We shall review the basic way the log-normal law occurs, and this will suggest a method of approximate solution of the wave equation. The method will involve certain iterations of the Born approximation. In order to end up with a "closed" form for the approximate solution, we will have to make certain assumptions about the nature of the scattering and the commutativity of certain operations.

We do not believe the method of solution is new, although we are not aware of similar approaches for optical waves in the turbulent atmosphere. The closest work appears to be that of Feinstein [18] who calculated the covariance function of such a field. The method appears to be in the vein suggested by Bellman and Koloba [19] and, although for "discrete" scatterers, Feynman [20]; in particular, the latter employs formally an "operator calculus" as we do here.

### 6.2. THE LOG-NORMAL DISTRIBUTION

The motivation for the present discussion is the need for an adequate characterization of an optical wave propagating a relatively long distance through a turbulent medium representing the atmosphere in order to eventually find the statistics of the scattered field. In turn, the statistics of the scattered field are required in order to find optimum procedures for transmission, reception, and processing of information transmitted via the atmosphere by waves in the visible spectrum. Of course, it is generally true that more second-order statistics are required to determine optimum procedures.

We emphasize that our discussion is heuristic and, again, we are led to it by the empirical observation of log-normal statistics rather infrequently; the log-normal probability law occurs for a very natural reason. Suppose a random phenomenon is described by a family of random variables  $\{E_n\}$  such that, for every  $n$ ,

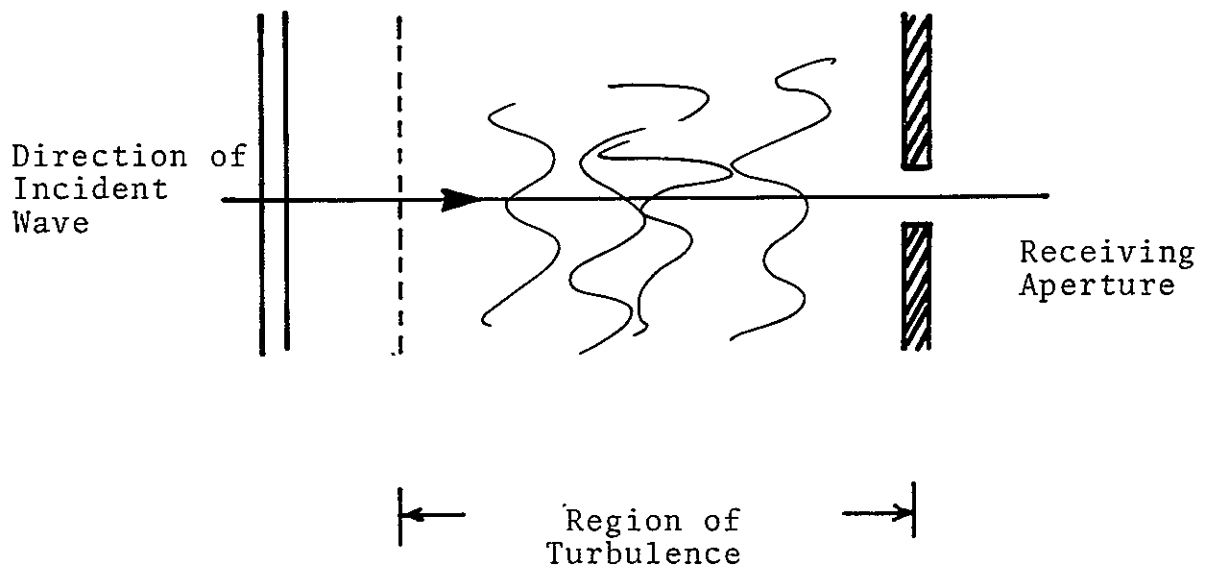


FIGURE 23. TYPICAL GEOMETRY FOR OPTICAL COMMUNICATION CHANNEL



$$E_{n+1} = E_n + \xi_{n+1} E_n \quad (32)$$

where the  $\{\xi_n\}$  is a family of random variables. The meaning of equation 32 is clear: the  $n + 1$ th random variable is the sum of the  $n$ th random variable plus a small perturbation which depends on the  $n$ th random variable; specifically, the dependence is direct proportionality. The fact that many natural phenomena can be modeled this way is not surprising, and the application to the progression of a wavefront from a plane  $P_n$  at  $z = z_n$  through a turbulent medium to a plane  $P_{n+1}$  at  $z = z_{n+1}$  is already roughly indicated.

We assume that  $\xi_n$  is small in some appropriate sense, e.g.,  $|\xi_n| \ll 1$  with large probability. Equation 32 can be written

$$E_{n+1} \approx e^{\xi_{n+1}} E_n = \left( \prod_{\ell=0}^{n+1} e^{\xi_{\ell+1}} \right) E_0 \quad (33)$$

and hence,

$$\log \frac{E_{n+1}}{E_0} \approx \sum_{\ell=0}^{n+1} \xi_{\ell+1} \quad (34)$$

If  $\sum_{\ell=0}^{n+1} \xi_{\ell+1}$  is (tends, as  $n \rightarrow \infty$ , to) a Gaussian, or normal random variable, then (by definition)  $\log (E_{n+1}/E_0)$  is (tends, as  $n \rightarrow \infty$ , to) a log-normal random variable.

There are a variety of conditions that allow a normal approximation to this summation:

- (1) If the  $\{\xi_n\}$  are normal, then so is every partial sum.
- (2) If the  $\{\xi_n\}$  are independent and identically distributed with mean  $m$  and variance  $\sigma^2$ , then as  $n \rightarrow \infty$ , the partial sum  $\sum_{\ell=1}^n \xi_{\ell}$  converges (in distribution) to a normal random variable with mean  $nm$  and variance  $n\sigma^2$  (see the Lindeberg-Levy theorem in ref. 21, p. 215).
- (3) If the  $\{\xi_n\}$  are independent but not identically distributed, there is a central limit theorem in agreement with Lindeberg [22, p. 236].
- (4) There are central limit theorems for partial sums of dependent variables [23, ch. 8].

The above discussion can be easily extended to continuously varying perturbations  $\{\xi_x\}$ :  $x$  now plays the role of a continuous index and  $\xi(x)$  is a random process. Now, for a small change  $\Delta$  in  $x$ , we have

$$E_{x+\Delta} \approx E_x + \Delta \xi$$

and, as  $n \rightarrow \infty$  and  $\Delta \rightarrow 0$ , we find

$$\log \frac{E_x}{E_{x0}} \approx \int_{x_0}^x \xi_x dx \quad (35)$$

It is interesting to note that equation 32 implies a specific way of accounting for multiple scattering. Consider  $E_2 = (1 + \xi_2)E_1 = (1 + \xi_2)(1 + \xi_1)E_0 = (1 + \xi_1 + \xi_2 + \xi_1\xi_2)E_0$ . This scattering is shown graphically in figure 24: we see that only "forward" scattering is accounted for. This is roughly the kind of approximation that we want for the scattering of optical waves by atmospheric turbulence since it is known that, approximately, only forward scattering in small angles is possible.

It should be pointed out that there are situations, different from the geometry of figure 23, when a log-normal law should not be expected. For example, consider the situation shown in figure 25: If the receiving aperture is far from the boundary of the turbulent region, relative to the correlation distance of wavefront emerging from the turbulent region, then the field at the receiving aperture is approximately a summation of uncorrelated contributions. Though this is not sufficient, we might hazard that the field at the aperture is approximately normal—not log-normal.

Generally there would be the intermediate situation where contributions to the field at a given point represent a sum of the contribution propagated along a ray from source to the point—which can be log-normal—and a sum of the contributions scattered from other rays—which could be normal.

### 6.3. APPROXIMATE SOLUTION OF WAVE EQUATION

As is well known [24], the inhomogeneous scalar wave equation in a medium with varying index of refraction  $n^2 \equiv 1 - q$  is

$$\nabla^2 E + k^2 E = E_0 + k^2 q E \quad (36)$$

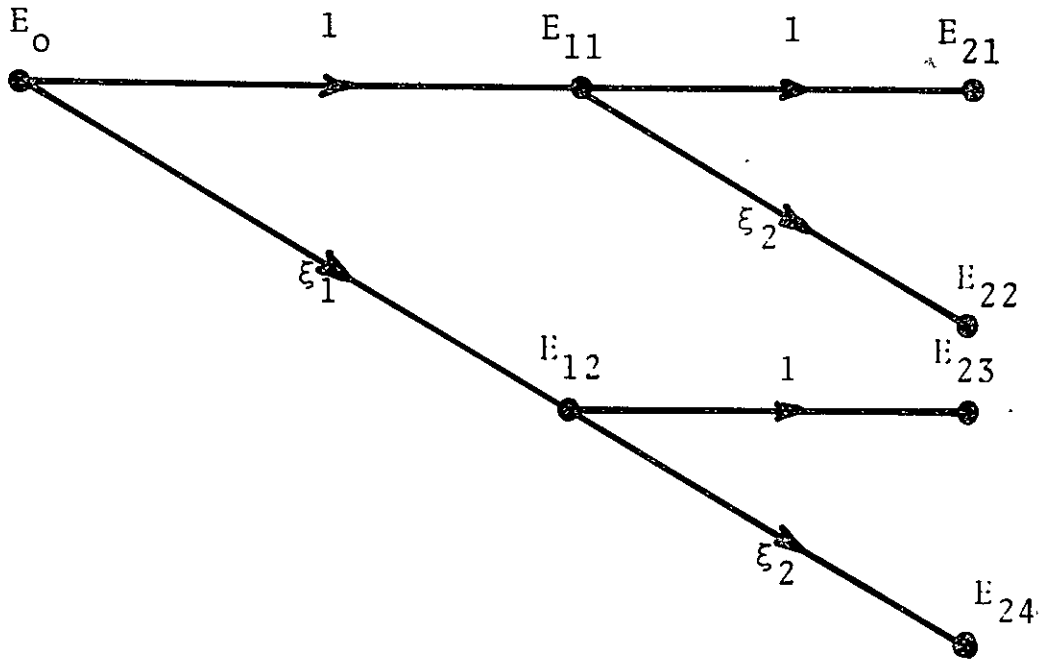
provided the index changes very little over a wavelength. In (36) we have assumed, as usual, a sinusoidal time variation for the field;  $E_0$  is the scalar field of the source. If  $E_\delta$  satisfies homogeneous boundary conditions, the radiation condition (for unbounded media), and the equation

$$\nabla^2 E_\delta + k^2 E_\delta = \delta \quad (37)$$

then, (36) may be written as an integral equation:

$$E = E_\delta * (E_0 + k^2 q E) \equiv A E_0 + k^2 A(q E) \quad (38)$$

We have introduced the operator notation  $A$ :  $Af \equiv E_\delta * f$  ( $A$  is a linear operator). The identity operator will be denoted  $I$ :  $If = f$ . The Born approximation  $E_B$  to  $E$  is the first two terms of the Neumann series [25] which is generated by simple iteration:



$$\left( E_i = \sum_j E_{ij} \right)$$

FIGURE 24. THE SCATTERING MECHANISM, IMPLIED BY EQUATION 32, THAT IMPLIES A LOG-NORMAL DISTRIBUTION FOR  $E_n/E_0$  AS  $n \rightarrow \infty$  IF  $\sum_{i=1}^n \xi_i$  CONVERGES (IN DISTRIBUTION) TO A NORMAL RANDOM VARIABLE AS  $n \rightarrow \infty$

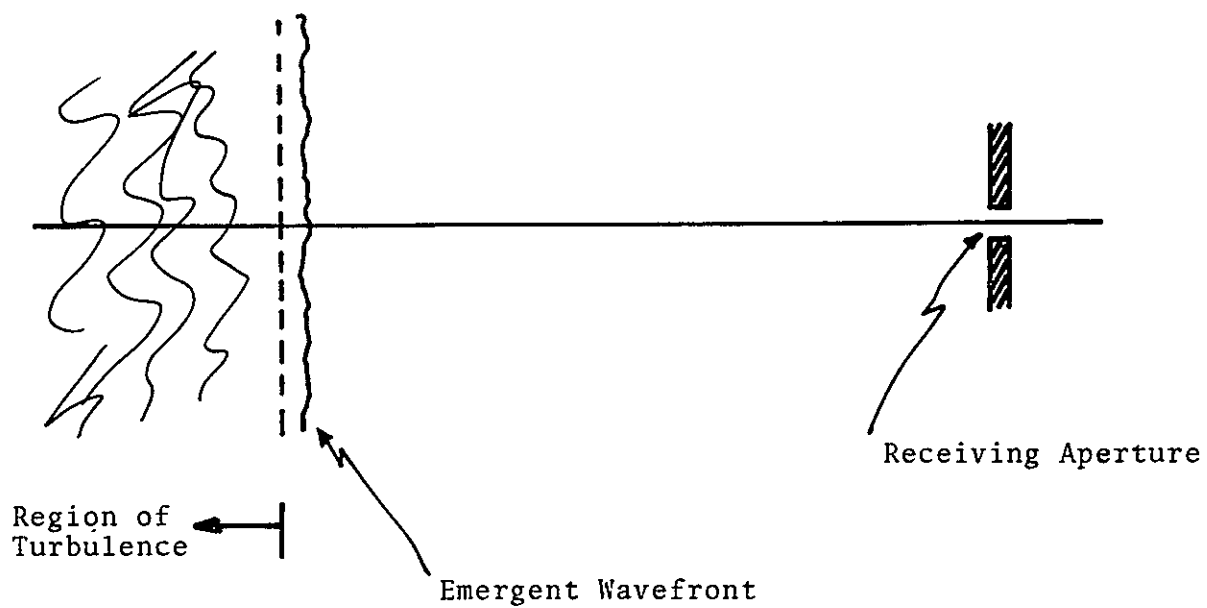


FIGURE 25. GEOMETRY WHERE NORMAL, VICE LOG-NORMAL, DISTRIBUTIONS MAY OCCUR

$$E_B = AE_0 + k^2 A(qAE_0) \quad (39)$$

Referring to figure 26, we wish to calculate the field after it has propagated a distance  $L$  into the turbulence. We allow  $L$  to be a distance too large for the Born approximation (Eq. 39) to be good. We subdivide the region ( $0 \leq z \leq L$ ) into layers  $\Delta$  thick as shown ( $z_{n+1} - z_n = \Delta$ , all  $n$ ) such that—the Born approximation is good, and the free-space diffraction is approximately

$$AE_n \approx e^{i(z-z_n)} E_n \quad (40)$$

With equation 40 and the fact that scattering will only be into small angles, we can make the simplification

$$A(qAE_n) \approx e^{ik(z_{n+1}-z_n)} \iiint_{V_\Delta} \frac{e^{ik\phi}}{4\pi(z-z_n)} q(r) E_n(x, y) dx dy dz \approx e^{ik(z_{n+1}-z_n)} A_1(q_{n+1} E_n) \quad (41)$$

where

$$\phi \equiv \frac{[(x_{n+1} - x)^2 + (y_{n+1} - y)^2]}{2(z_{n+1} - z)}$$

the so-called sagittal approximates. Then equation 39 becomes

$$E_{n+1} \approx e^{ik\Delta} [I + k^2 A_1(q_{n+1})] E_n \approx e^{ik\Delta} e^{k^2 A_1(q_{n+1})} E_n \quad (42)$$

Equation 42 is the generalization of (32) for the propagation of an optical wave through a turbulent medium of described type;  $\exp k^2 B$  is, of course, a linear operator defined by the expansion  $I + k^2 B + \dots$ . We index  $q$  because it depends upon the particular sample function segment of  $q$  present in the slab  $\{r: z_n \leq z \leq z_{n+1}\}$ . We iterate the relation (32) and find

$$E_{n+1} \approx e^{ikn\Delta} \prod_{\ell=0}^n e^{k^2 A_2(q_{\ell+1})} E_0 \quad (43)$$

The product of operators appearing in (43) is generally ordered.

However, in the case of homogeneous turbulence, that is, turbulence whose statistical properties are invariant to spatial location, any particular segment of  $q$  appearing in the slab  $\{r: z_i \leq z \leq z_{i+1}\}$  is just as likely to appear in the slab  $\{r: z_j \leq z \leq z_{j+1}\}$ ,  $j \neq i$ . Therefore, the statistical properties of  $E_{n+1}$  should be invariant to permutations of order in equation 43. We therefore assume that, insofar as we are interested in statistical properties of  $E_{n+1}$ , the operators may be assumed commutative. But if this is true, then it is easy to show that

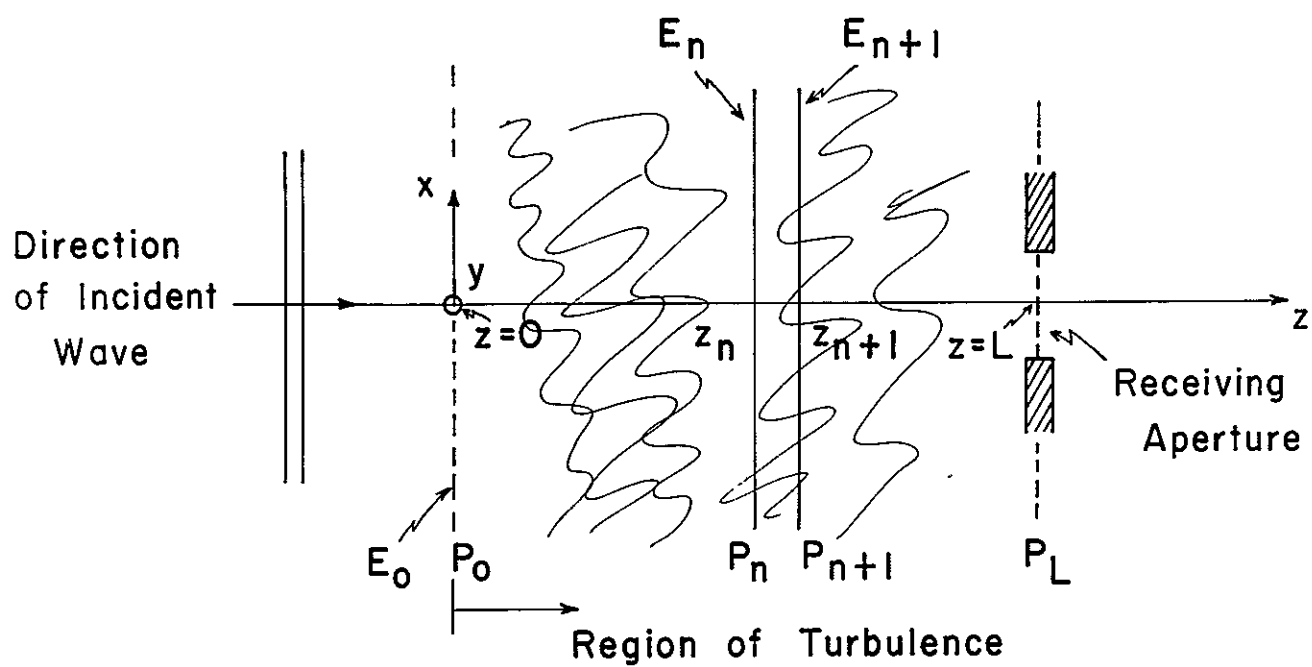


FIGURE 26. THE GEOMETRY AND SUBDIVISION FOR THE CONVOLUTION OF THE SCATTERED WAVE

$$\prod_{\ell=0}^n e^{ik^2 A_1(q_{\ell+1})} = \exp \left[ k^2 \sum_{\ell=0}^n A_1(q_{\ell+1}) \right] \equiv \exp \left[ k^2 A_1(q_{n*}) \right]$$

where

$$q_{n*} \equiv \sum_{\ell=0}^n q_{\ell+1}.$$

Thus, finally,

$$E_{n+1} \approx e^{ikn\Delta} e^{ik^2 A_1(q_{n*})} E_0 \quad (44)$$

#### 6.4. APPLICATION

We now return to the geometry of figure 26 and apply the above approximation method. We divide the z-segment  $\{0 \leq z \leq L\}$  into  $N \equiv L/\Delta$  "slabs" where  $\Delta$  is chosen so that (1) the Born approximation is good, (2) free-space diffraction is small, and (3) the segments of  $q$  are approximately independent. Requirement 2 will be satisfied if, roughly,

$$\Delta \ll \frac{\ell^2}{\lambda}$$

where  $\ell$  is the smallest significant dimension of the turbulence. Requirement 3 will be satisfied if  $\Delta \gg L_0$  where  $L_0$  is the largest significant dimension of the turbulence. We must, therefore, have

$$\frac{\ell}{L_0} \left( \frac{\ell}{\lambda} \right) \gg 1$$

This is presumably true in the atmosphere for optical wavelengths.

Then, we have

$$E_L \approx e^{ikL} e^{ik^2 A_\Delta(q^*)} E_0 \quad (45)$$

where

$$q^* \equiv \sum_{\ell=1}^n q_{\ell+1}$$

and  $A_\Delta$  is defined by equation 41. Equation 45 is the result that we have sought.

## 6.5. FURTHER COMMENTS

The result (45) states, among other things, that the turbulence is equivalent to a strange turbulence distributed over a correspondingly shorter distance. It is to be noted that  $k^2 A_{\Delta}(q^* E_0)$  need not be small (in some sense) with unity in order that (45) hold. For example, in the ray optics limit,

$$A_{\Delta}(q^*) \approx e^{i \frac{\pi}{4} \int_{\Delta} q^*(z) dz} \quad (46)$$

the phase need not be small with respect to a radian in order that this approximation apply.

If the region  $\{z: 0 \leq z \leq L\}$  is composed of subregions of homogeneous turbulence, of a different statistical nature in each region, then, of course, we can apply our approximate method of each subregion. Obviously, some of the subregions can be free of turbulence. (We must keep in mind that we have ignored free-space diffraction: this limits the distance  $L_1$  in a well known way on beam dimension and wavelength. For example, for a uniform circular beam area  $A$ , we must have  $L_1 \ll A/\lambda$ .)

It should also be noted that result (45) does not necessarily predict log-normal statistics. Generally, the statistics are quite complicated. In the ray optics limit, we generally expect log-normal for the reasons originally outlined.

## 7

### THE LOG-NORMAL RANDOM PROCESS

#### 7.1. DEFINITIONS

Both the experimental results on the first-order distribution only (apparently) and the Rytov method within its domain of validity show that the so-called log-normal distribution occurs in optical propagation through the turbulent atmosphere, although the exact conditions of its appearance are unknown. This process is, therefore, worthy of study, and is analyzed here in relation to the definitions listed.

(1) Let  $(X_t, t \in T)$ ,  $X_t \equiv \beta_t + iS_t$  be a complex Gaussian process; then the process where  $\{Y_t, t \in T\}$  and

$$Y_t \equiv e^{X_t}, t \in T \quad (47)$$

is called a log-normal process.

Definition (1) is a special case of the more general nonlinear transformation  $g(x_t)$  of  $\{X_t, t \in T\}$ , where  $g$  is a real-valued measurable function of a real variable.

Equation 47 is such that the ensemble averages of combinations of the values of  $Y_{t_j}$  can be evaluated from the well-known forms of the characteristic functions of a Gaussian process.



For the optical propagation problem, we wish  $T$  to be of greater than one dimension; then "process" is replaced by "field" in definition (1).

(2) We recall that if  $(x_n)$  is an aggregate of real Gaussian random variables, then its joint characteristic function is

$$\phi_{x_1, \dots, x_N}(u_1, \dots, u_N) \equiv E[e^{i(\vec{u}, \vec{x})}] = \exp \left( +i\vec{u} \vec{m} - \frac{1}{2} \vec{u} \Lambda \vec{u} \right)$$

where the row vector  $\vec{u}^t \equiv (u_1, \dots, u_N)$  is the transpose of the column vector  $\vec{u}$ ,  $\vec{m}$ , is the column vector of means,  $\vec{m}^t \equiv (m_1, \dots, m_N)$ ,  $m_n \equiv E(x_n)$ , and  $\Lambda$  is an  $N \times N$  covariance matrix of element  $\lambda_{mn} \equiv E\{[x_m - E(x_m)][x_n - E(x_n)]\}$ . Their joint density function is

$$P_{x_1, \dots, x_N}(x_{10}, \dots, x_{N0}) = \frac{1}{\sqrt{(2\pi)^N |\Lambda|}} \exp - \frac{\sum_{m,n=1}^N |\Lambda_{mn}| (x_{m0} - m_m)(x_{n0} - m_n)}{2 |\Lambda|} \quad (48)$$

where  $|\Lambda|$  is the determinant of  $\Lambda$  and  $|\Lambda_{mn}|$  is the determinant of the cofactor of  $\lambda_{mn}$ . The cofactor matrix  $\Lambda_{mn}$  of  $\lambda_{mn}$  is obtained from  $\Lambda$  by omitting the  $m$ th row and  $n$ th column of  $\Lambda$ .

The statements of definition (2) carry over immediately to a random process  $(x_t, t \in T)$  with mean-value function  $m(t) \equiv E(x_t)$  and centered covariance function  $r(t, s) \equiv E[(x_t - m_t)(x_s - m_s)]$ .

(3) For any complex process  $(z_t, t \in T)$ , we define the following expectations: The mean-value function  $m_z(t) \equiv E(z_t)$ ; the covariance functions  $R_z(t_1, t_2) \equiv E\left(z_{t_1} \bar{z}_{t_2}\right)$  and  $R_{zz}(t_1, t_2) \equiv E\left(z_{t_1} z_{t_2}\right)$ .

We have  $R_z(t_1, t_2) = \overline{R_z(t_2, t_1)}$ , and  $R_{zz}(t_1, t_2) = R_{zz}(t_2, t_1)$ .

If  $z_{Rt} \equiv \text{Re}(z_t)$  and  $z_{It} \equiv \text{Im}(z_t)$ , then we define the covariance function

$$R_{z_R z_I}(t_1, t_2) \equiv E\left(z_{Rt_1} z_{It_2}\right)$$

and have immediately

$$R_{z_R z_I}(t_1, t_2) = R_{z_I z_R}(t_2, t_1)$$

Then,

$$R_z(t_1, t_2) = R_{z_R}(t_1, t_2) + R_{z_I}(t_1, t_2) + iR_{z_I z_R}(t, s) - iR_{z_R z_I}(t, s)$$

and

$$R_{zz}(t_1, t_2) = R_{z_R}(t_1, t_2) - R_{z_I}(t_1, t_2) + iR_{z_I z_R}(t, s) + iR_{z_R z_I}(t, s)$$

We shall also use the centered covariance functions

$$r_z(t_1, t_2) \equiv E \left\{ \left[ z_{t_1} - m_z(t_1) \right] \left[ \overline{z_{t_2} - m_z(t_2)} \right] \right\} = R_z(t_1, t_2) - m_z(t_1) \overline{m_z(t_2)}$$

and

$$r_{zz}(t_1, t_2) \equiv E \left\{ \left[ z_{t_1} - m_z(t_1) \right] \left[ z_{t_2} - m_z(t_2) \right] \right\} = R_{zz}(t_1, t_2) - m_z(t_1) m_z(t_2)$$

Lemma: If  $[Y_t \equiv \exp(\beta_t + iS_t), t \in T]$  is a log-normal process and  $(t_n \in T, 1 \leq n \leq N)$  and  $(\alpha_n, 1 \leq n \leq N)$  are complex scalars, then

$$E \begin{pmatrix} \alpha_1 & \alpha_N \\ Y_{t_1} & \dots & Y_{t_N} \end{pmatrix} = e^{i \vec{u}^t \vec{m} - \frac{1}{2} \vec{u}^t \Lambda \vec{u}} \quad (49)$$

where

$$\vec{u}^t \equiv (u_1, \dots, u_{2N})$$

$$u_j \equiv \begin{cases} -i\alpha_j, & 1 \leq j \leq N \\ \alpha_j, & N+1 \leq j \leq 2N \end{cases}$$

$$\vec{m}^t \equiv (m_1, \dots, m_{2N}),$$

$$m_j \equiv \begin{cases} m_{\beta}(t_j), & 1 \leq j \leq N \\ m_S(t_j), & N+1 \leq j \leq 2N \end{cases}$$

and  $\Lambda$  is the  $2N \times 2N$  matrix of elements

$$\lambda_{mn} = E[(\xi_m - m_m)(\xi_n - m_n)]$$

$$\xi_m \equiv \begin{cases} \beta(t_m), & 1 \leq m \leq N \\ S(t_m), & N+1 \leq m \leq 2N \end{cases}$$

Proof: We have

$$E \begin{pmatrix} \alpha_1 & \alpha_N \\ Y_{t_1} & \dots & Y_{t_N} \end{pmatrix} = E \left[ e^{i(-i\alpha_1)\beta_{t_1} + \dots + i(-i\alpha_N)\beta_{t_N} + i\alpha_1 S_{t_1} + \dots + i\alpha_N S_{t_N}} \right]$$

which is the joint characteristic function of the jointly normal variables  $\left(\beta_{t_1}, \dots, \beta_{t_N}, S_{t_1}, \dots, S_{t_N}\right)$  evaluated at the point  $(-i\alpha_1, \dots, -i\alpha_N, \alpha_1, \dots, \alpha_N)$ . Equation 49 then follows directly from definition (2).

Theorem 1: If  $[Y_t \equiv \exp(\beta_t + iS_t), t \in T]$  is a log-normal process and  $\{t_n \in T, 1 \leq n \leq N\}$  and  $\vec{\alpha}^t \equiv (\alpha_1, \dots, \alpha_N)$  is a row vector of  $N$  complex scalars, then

$$E\left(Y_{t_1}^{\alpha_1} \dots Y_{t_N}^{\alpha_N}\right) = \exp \left[ \vec{\alpha}^t \vec{m}_\beta + i\vec{\alpha}^t \vec{m}_S + \frac{1}{2} \left( \vec{\alpha}^t \Lambda_{\beta\beta} \vec{\alpha} - \vec{\alpha}^t \Lambda_{SS} \vec{\alpha} + i\vec{\alpha}^t \Lambda_{\beta S} \vec{\alpha} + i\vec{\alpha}^t \Lambda_{S\beta} \vec{\alpha} \right) \right]$$

where  $\vec{m}_\beta^t$  is the row vector of elements  $m_\beta(t_n) \equiv E[\beta(t_n)]$ ,  $\vec{m}_S^t$  is the row vector of elements  $m_S(t_n) \equiv E[S(t_n)]$ ,  $\Lambda_{\phi\psi}$  is the  $N \times N$  matrix of elements

$$r_{\phi\psi}(t_m, t_n) \equiv E \left\{ \left[ \phi_{t_m} - E(\phi_{t_m}) \right] \left[ \psi_{t_n} - E(\psi_{t_n}) \right] \right\}$$

where  $\phi$  and  $\psi$  are either  $\beta$  or  $S$ .

Proof: We note that the vectors and matrix of the lemma can be partitioned

$$\vec{u}^t = (-i\vec{\alpha}^t | \xi\vec{\alpha}^t), \vec{m}^t = (\vec{m}_\beta | \vec{m}_S)$$

and

$$\Lambda = \frac{\Lambda_{\beta\beta} \mid \Lambda_{\beta S}}{\Lambda_{S\beta} \mid \Lambda_{SS}}$$

with definitions given below in the statement of the corollary. Since matrixes with partitioned matrix elements obey the same multiplication rule as matrixes with scalar elements (order must be preserved, of course [26]), the assertion now follows.

Corollary 1: If  $(Y_t \equiv \beta_t + iS_t, t \in T)$  is a log-normal process,  $\alpha$  is complex scalar, and  $t \in T$ , then

$$E(Y_t^\alpha) = \exp \left\{ \alpha m_\beta(t) + i\alpha m_S(t) + \frac{1}{2} \left[ \alpha^2 \sigma_\beta^2(t) + 2\alpha^2 \sigma_\beta(t) \sigma_S(t) \rho_{\beta S}(t, t) - \alpha^2 \sigma_S^2(t) \right] \right\}$$

where  $\rho_{\beta S}(t, s) \equiv r_{\beta S}(t, s) / \sigma_\beta(t) \sigma_S(s)$ ,  $\sigma_\beta^2 \equiv r_\beta(t, t)$ , and  $\sigma_S^2 \equiv r_S(t, t)$ ; in particular, the mean-value function

$$m_Y(t) \equiv E(Y_t) = \exp \left\{ m_{\beta_t} + im_{S_t} + \frac{1}{2} \left[ \sigma_{\beta_t}^2 + 2\sigma_{\beta_t} \sigma_{S_t} \rho_{\beta S}(t, t) - \sigma_{S_t}^2 \right] \right\}$$

Proof: In theorem 1, the vectors  $\vec{\alpha}$ ,  $\vec{m}_\beta$ , and  $\vec{m}_S$  reduce to scalars  $\alpha$ ,  $m_\beta(t)$ , and  $m_S(t)$ , respectively, and the matrixes  $\Lambda_{\beta\beta}$ ,  $\Lambda_{SS}$ , and  $\Lambda_{\beta S}$  reduce to scalars  $r_{\beta\beta}(t, t)$ ,  $r_{SS}(t, t)$ , and  $r_{\beta S}(t, t)$ , respectively.

Corollary 2: If  $[Y_t \equiv \exp(\beta_t + iS_t), t \in T]$  is a log-normal process;  $\alpha_1, \alpha_2$  are real numbers; and  $t_1, t_2, \in T$ , then  $E\left(Y_{t_1}^{\alpha_1} Y_{t_2}^{\alpha_2}\right)$  is given by theorem 1 with

$$\vec{\alpha}^t \vec{m}_\beta = \alpha_1 m_\beta(t_1) + \alpha_2 m_\beta(t_2)$$

$$\vec{\alpha}^t \vec{m}_S = \alpha_1 m_S(t_1) + \alpha_2 m_S(t_2)$$

$$\alpha^t \Lambda_{\beta\beta} \alpha = \alpha_1^2 \sigma_\beta^2(t_1) + 2\alpha_1 \alpha_2 \sigma_\beta(t_1) \sigma_\beta(t_2) \rho_\beta(t_1, t_2) + \alpha_2^2 \sigma_\beta^2(t_2)$$

$$\alpha^t \Lambda_{SS} \alpha = \alpha_1^2 \sigma_S^2(t_1) + 2\alpha_1 \alpha_2 \sigma_S(t_1) \sigma_S(t_2) \rho_S(t_1, t_2) + \alpha_2^2 \sigma_S^2(t_2)$$

$$\alpha^t \Lambda_{\beta S} \alpha = \alpha_1^2 r_{\beta S}(t_1, t_1) + 2\alpha_1 \alpha_2 r_{\beta S}(t_1, t_2) + \alpha_2^2 r_{\beta S}(t_2, t_1)$$

and

$$\alpha^t \Lambda_{S\beta} \alpha = \alpha_1^2 r_{S\beta}(t_1, t_1) + 2\alpha_1 \alpha_2 r_{S\beta}(t_1, t_2) + \alpha_2^2 r_{S\beta}(t_2, t_2)$$

In particular, the covariance function  $R_{YY}$  is obtained from these relations with  $\alpha_1 = \alpha_2 = 1$ .

Corollary 3: If  $[Y_t \equiv \exp(\beta_t + iS_t), t \in T]$  is a log-normal process, then its covariance function is

$$\begin{aligned} R_Y(t_1, t_2) \equiv E\left\{Y_{t_1} \overline{Y}_{t_2}\right\} &= \exp\left\{m_{\beta_1} + m_{\beta_2} + i\left(m_{S_1} - m_{S_2}\right)\right. \\ &\quad + \frac{1}{2}\left[\left(R_{\beta_{11}} + 2R_{\beta_{12}} + R_{\beta_{22}}\right) - \left(R_{S_{11}} - 2R_{S_{12}} + R_{S_{22}}\right)\right. \\ &\quad \left.\left.+ 2i\left(R_{\beta S_{11}} - R_{\beta S_{22}}\right)\right]\right\} \end{aligned}$$

Proof: The proof is straightforward but slightly involved. First of all,

$$E\left\{Y_{t_1} \overline{Y}_{t_2}\right\} = \phi_{\beta_1, \beta_2, S_1, S_2}(-i, -i, 1, -1) = \exp\left(i \vec{u}^t \vec{m} - \frac{1}{2} \vec{u}^t \Lambda \vec{u}\right)$$

where

$$\vec{u}^t \equiv \left(\vec{u}_1^t \mid \vec{u}_2^t\right) = [(-i \ -i) \mid (1 \ -1)]$$

$$\vec{m}^t \equiv \left(\vec{m}_\beta^t \mid \vec{m}_S^t\right) = \left[\left(m_{\beta_1} \ m_{\beta_2}\right) \mid \left(m_{S_1} \ m_{S_2}\right)\right]$$

and

$$\Lambda \equiv \left( \begin{array}{c|c} \Lambda_{\beta} & \Lambda_{\beta S} \\ \hline \Lambda_{S\beta} & \Lambda_S \end{array} \right)$$

where, e.g.,

$$\Lambda_{\beta} \equiv \begin{pmatrix} R_{\beta 11} & R_{\beta 12} \\ R_{\beta 21} & R_{\beta 22} \end{pmatrix}$$

With these partitionings, we can write

$$\vec{u}^t \Lambda \vec{u} = \vec{u}_1^t \Lambda_{\beta} \vec{u}_1 + \vec{u}_1^t \Lambda_{\beta S} \vec{u}_2 + \vec{u}_2^t \Lambda_{S\beta} \vec{u}_1 + \vec{u}_2^t \Lambda_S \vec{u}_2$$

and

$$\vec{u}^t \vec{m} = \vec{u}_1^t \vec{m}_{\beta} + \vec{u}_2^t \vec{m}_S$$

By direct calculation, we find, e.g.,

$$\vec{u}_1^t \Lambda_{\beta} \vec{u}_1 = - \left( R_{\beta 11} + 2R_{\beta 12} + R_{\beta 22} \right)$$

where we have used the fact that  $R_{\beta 12} = R_{\beta 21}$  for a real process ( $\beta_t$ ). Further,

$$\vec{u}_1^t \Lambda_{\beta S} \vec{u}_2 + \vec{u}_2^t \Lambda_{S\beta} \vec{u}_1 = -i \left( R_{S\beta 11} - R_{S\beta 22} \right)$$

where we have used the fact that  $R_{\beta S 12} = R_{S\beta 21}$  for real processes. With similar calculations, the assertion results.

## 7.2. STATIONARY PROCESSES

We assume, in this section, that  $(\beta_t, t \in T)$  and  $(S_t, t \in T)$  are wide-sense stationary, and we list the following definitions:

(4) The real random process  $(x_t, t \in T)$  is wide-sense stationary, if  $E(x_t^2) < \infty$  and  $R_x(t+s, s) \equiv E(x_{t+s} x_s)$  does not depend on  $S$ .

If the real wide-sense stationary random process  $\{x_t, t \in T\}$  is Gaussian and  $E(x_t)$  does not depend on  $t$ , then  $(x_t, t \in T)$  is strictly stationary.

(5) The real, wide-sense stationary processes  $\{\beta_t, t \in T\}$  and  $\{S_t, t \in T\}$  are jointly wide-sense stationary, if  $R_{\beta S}(t+s, s) \equiv E\{\beta_{t+s} S_s\}$  does not depend on  $S$ .

We confuse the notation by denoting, e.g.,  $R_{\beta}(t+s, s)$  by  $R_{\beta}(t)$  when  $\{\beta_t, t \in T\}$  is wide-sense stationary. If  $\{\beta_t, t \in T\}$  and  $\{S_t, t \in T\}$  are jointly wide-sense stationary, then  $R_{\beta S}(t) = R_{S\beta}(-t)$ .

(6) A complex random process  $(X_t, t \in T)$  is wide-sense stationary, if  $E(|X_t|^2) < \infty$  and  $R_X(t+s, s) = E\{X_{t+s}\overline{X_s}\}$  does not depend on  $s$ .

From equation 48 above, we see that  $(X_t \equiv \beta_t + iS_t)$  is wide-sense stationary, if  $\{\beta_t, t \in T\}$  and  $\{S_t, t \in T\}$  are jointly wide-sense stationary.

If a complex process is wide-sense stationary and Gaussian with, e.g., zero mean value function and  $R_{XX}(t+s, s) = E\{X_{t+s}X_s\} = 0$ , then it is strictly stationary.

We shall assume where the process  $(\beta_t, t \in T)$  and  $(S_t, t \in T)$  are jointly wide-sense stationary, that their mean value functions  $m_{\beta}(t)$  and  $m_S(t)$  do not depend on  $t$ .

Theorem 2: If  $\{Y_t \equiv \exp(\beta_t + iS_t), t \in T\}$  where  $\{\beta_t, t \in T\}$  and  $\{S_t, t \in T\}$  are jointly wide-sense stationary Gaussian (JWSSG) processes with constant mean value functions, then

$$m_Y = \exp \left\{ m_{\beta} + im_S + 1/2 \left[ \sigma_{\beta}^2 + 2\sigma_{\beta} \sigma_S \rho_{\beta S}(0) - \sigma_S^2 \right] \right\} \quad (50)$$

$$R_Y(t) = \exp \left\{ 2m_{\beta} + \sigma_{\beta}^2 [1 + \rho_{\beta}(1)] - \sigma_S^2 [1 - \rho_S(t)] \right\} \quad (51)$$

and

$$R_{YY}(t) = R_Y(t) \exp 2i[m_S + r_{\beta S}(t) + r_{S\beta}(t) + 2r_{\beta S}(0)] \quad (52)$$

Proof: Equation 50 follows trivially from the equation of corollary 1. Equation 51 follows easily from the equations of corollary 2. Equation 52 follows trivially from corollary 3.

Theorem 2 implies that if  $\{\beta_t, t \in T\}$  and  $\{S_t, t \in T\}$  are JWSSG processes with constant mean value functions, then  $\{Y_t \equiv \exp(\beta_t + iS_t), t \in T\}$  is a WSS log-normal (complex) process with constant mean value function.

Theorem 3: If  $\{Y_t \equiv \exp(\beta_t + iS_t), t \in T\}$  where  $(\beta_t, t \in T)$  and  $\{S_t, t \in T\}$  are JWSSG processes with zero means, then the covariance functions  $R_Y$  and  $R_{YY}$  completely determine the  $(Y_t, t \in T)$  log-normal process.

Proof: It is sufficient to show that  $R_Y$  and  $R_{YY}$  determine  $R_{\beta}$  and  $R_S$ , for then the Gaussian processes  $\{\beta_t, t \in T\}$  and  $\{S_t, t \in T\}$  will be completely determined (recall the lemma) and hence then also  $(Y_t, t \in T)$ .

From theorem 2 we have

$$\log R_Y(t) = \sigma_{\beta}^2 [1 + \rho_{\beta}(t)] - \sigma_S^2 [1 - \rho_S(t)] \quad (53)$$

and

$$\log R_{yy}(t) = \sigma_{\beta}^2[1 + \rho_{\beta}(t)] - \sigma_s^2[1 + \rho_s(t)] \quad (54)$$

Subtracting equation 54 from equation 53,

$$\sigma_s^2 \rho_s(t) = 1/2 \log \frac{R_y(t)}{R_{yy}(t)} \quad (55)$$

thus,  $(s_t, t \in T)$  is completely specified.

We can then, e.g., add equations 53 and 54 to get

$$1/2 \log R_y(t) R_{yy}(t) = \sigma_{\beta}^2[1 + \rho_{\beta}(t)] - \sigma_s^2$$

or,

$$\sigma_{\beta}^2[1 + \rho_{\beta}(t)] = \log R_y(t)$$

Hence, it is easy to see that

$$\sigma_{\beta}^2 \rho_{\beta}(t) = \log \frac{R_y(t)}{\sqrt{R_y(0)}}$$

Thus,  $\{\beta_t, t \in T\}$  is completely determined.

Lemma: If  $(\beta_t, t \in T)$  and  $(S_t, t \in T)$  are WSSG processes with constant mean value functions, then

$$E\left(e^{\beta_{t+s} + \beta_s}\right) = \exp\left\{2m_{\beta} + \sigma_{\beta}^2[1 + \rho_{\beta}(t)]\right\} \quad (56)$$

and

$$E\left\{e^{iS_{t+s} - iS_s}\right\} = \exp\left\{-\sigma_s^2[1 - \rho_s(t)]\right\} \quad (57)$$

Proof: To prove equation 56 we, of course, note that  $E[\exp(\beta_{t+s} + \beta_s)]$  is the joint characteristic function of the Gaussian random variable  $\beta_{t+s}$  and  $\beta_s$ , evaluated at  $(-i, -i)$ . From the lemma, we have the asserted result. Similarly,  $E[\exp(iS_{t+s} - iS_s)]$  is the joint characteristic function of the Gaussian random variables  $S_{t+s}$  and  $S_s$ , evaluated at  $(1, -1)$ . From the lemma, we have the asserted result (eq. 57).

Theorem 4: The log-normal random variables  $\exp(\beta_{t+s} + \beta_s)$  and  $\exp i(S_{t+s} - S_s)$  formed from the JWSSG constant mean processes  $(\beta_t, t \in T)$  and  $(S_t, t \in T)$  are uncorrelated.

Proof: We note that we can write

$$R_y(t) = E[\exp(\beta_{t+s} + \beta_s) \cdot \exp i(S_{t+s} - S_s)]$$

Comparing the form of  $R_y$  asserted by theorem 2 with the asserted forms of the lemma, we have

$$E[\exp(\beta_{t+s} + \beta_s) \cdot \exp i(S_{t+s} - S_s)] = E[\exp(\beta_{t+s} + \beta_s)] \cdot E[\exp i(S_{t+s} - S_s)]$$

Theorem 4 has been asserted with the incorrect proof that asserts the two random variables  $(\beta_{t+s} + \beta_s)$  and  $i(S_{t+s} - S_s)$  are uncorrelated. For example, Cernov [27] specifically asserts  $E(\beta_{t2} S_{t1}) = E(\beta_{t1} S_{t2})$  which is not generally true. The most that can be said without further assumption is that  $R_{\beta S}(t) = R_{S\beta}(-t)$  (they are real, WSS processes).

### 7.3. LIKELIHOOD FUNCTIONAL

Of paramount importance in communication-type problems of detection (hypothesis testing and estimation, e.g., regression) is the likelihood ratio, or likelihood functional, in the context of random processes. We now seek this functional for the log-normal random process.

Real processes:  $z_t \equiv \exp x_t$ . We begin by considering real log-normal processes  $\{z_t \equiv \exp x_t\}$  and the typical test between the two hypotheses:

$$H_1: z_t = g(x_t)$$

$$H_0: z_t = g(y_t)$$

where  $(x_t, t \in T)$  and  $(y_t, t \in T)$  are Gaussian processes. We suspect that if  $g$  is, e.g., a monotone function of a real variable, the likelihood functional should exist provided the likelihood functional for the problem

$$H_1: g^{-1} z_t = x_t$$

$$H_0: g^{-1} z_t = y_t$$

exists: that is, if the Gaussian processes  $\{x_t, t \in T\}$  and  $\{y_t, t \in T\}$  are equivalent.

The basis for this expectation is the following. We take as the underlying probability spaces the function spaces: then  $g$  is a very simple transformation on these spaces, and the new measures seemingly can be obtained from the old just as with ordinary random variables.

$$f_2(z) = \frac{f_z[g^{-1}(z)] \frac{d}{dz} g^{-1}(z)}{f_y[g^{-1}(z)] \frac{d}{dz} g^{-1}(z)} = \frac{f_x[g^{-1}(z)]}{f_y[g^{-1}(z)]} = f_1[g^{-1}(z)]$$

We may motivate this further by the following argument. Under conditions of equivalence, the likelihood functional is calculable from the limit

$$f_1(z) = \lim_{N \rightarrow \infty} f_{1N}(z), f_{1N}(z) \equiv \frac{f_x(z_{t1}, \dots, z_{tN})}{f_y(z_{t1}, \dots, z_{tN})}$$



To find this ratio for  $H_1$  when  $z = g(x)$  and for  $H_0$  when  $z = g(y)$ , we use well-known elementary probability theory. The Jacobian reduces to a diagonal because of the simple nature of the  $X$  formation from  $x(y)$  to  $z$ :

$$|J| = \prod_{i=1}^N \left[ \frac{\partial}{\partial z} g^{-1}(z) \right]_{z=z_{ti}}$$

In any case, the Jacobian cancels out, giving

$$f_{2N}(z) = \frac{f_x[g^{-1}(z_{t1}), \dots, g^{-1}(z_{tN})]}{f_y[g^{-1}(z_{t1}), \dots, g^{-1}(z_{tN})]}$$

It would appear that under certain conditions of  $g$ , the linear operation should be successful. Formally,

$$f_2(z_t) = \lim_{N \rightarrow \infty} f_{2N}(z) = f_1[g^{-1}(z_t)]$$

Theorem 5: If  $A_{1t} \equiv e^{\beta_{1t}}$  and  $A_{2t} \equiv e^{\beta_{2t}}$  are log-normal processes such that  $(\beta_{1t})$  and  $(\beta_{2t})$  are equivalent, with likelihood functional  $f_\beta(z) \equiv dP_{\beta_1}(z)/dP_{\beta_2}(z)$ , then the likelihood functional

$$f_A(z) \equiv \frac{dP_{A1}(z)}{dP_{A2}(z)} = f_\beta(\log z_t)$$

Proof: We have the measurable space  $(\Omega, \beta)$  associated with the process  $(x_t, t \in T)$ ; on the measurable sets we have either a probability measure  $P_0$  or a probability measure  $P_1$ , giving rise to two measure spaces  $(\Omega, \beta, P_0)$  and  $(\Omega, \beta, P_1)$ . We assume that  $P_0$  and  $P_1$  are equivalent, i.e., mutually absolutely continuous. Then, by the Radon-Nikodyn theorem there exists a finite-valued  $P_0$  measurable function  $f$  such that, for any set  $B \in \beta$

$$P_1(B) = \int_B f(\omega) dP_0(\omega) \quad (58)$$

$f$  is the Radon-Nikodyn derivative, frequently denoted  $dP_1/dP_0$ , or likelihood functional [28, theo. 31.B].

Now let  $g$  be a monotone, increasing, continuous, real function of a real variable and consider the new random process, defined by the relation  $y(t) \equiv g[x(t)]$ , with measurable space denoted  $(\Sigma, S)$ . This relation induces a transformation  $T$  from  $\Omega$  to  $\Sigma$ : its nature is most easily seen if we take  $\Omega$  and  $\Sigma$  to be the function, or coordinate, spaces  $\tilde{\Omega}$  and  $\tilde{\Sigma}$  [29]. For then  $T$  is  $g$ : since  $g$  is continuous and monotone,  $T$  must be measurable and one-to-one. Thus  $T$  induces two new measures,  $Q_0 \equiv P_0 T^{-1}$  and  $Q_1 \equiv P_1 T^{-1}$ , giving rise to the two measure spaces  $(\tilde{\Sigma}, S, Q_0)$  and  $(\tilde{\Sigma}, S, Q_1)$ .

The measures  $Q_0$  and  $Q_1$  are also equivalent, since  $P_0$  and  $P_1$  are [28, p. 165]. Therefore, there exists a  $Q_0$ -measurable function  $h$  such that, for any  $s \in S$ ,

$$Q_1(S) = \int_S h(\tilde{\sigma}) dQ_0(\tilde{\sigma})$$

That is,

$$P_1 T^{-1}(S) = \int_S h(\tilde{\sigma}) dP_0 T^{-1}(\tilde{\sigma})$$

But we can rewrite the right side as [28]

$$\int_{T^{-1}(S)} h[T(\tilde{\omega})] dP_0(\tilde{\omega})$$

thus, setting  $B \equiv T^{-1}(S)$ , we have that for an arbitrary  $s \in S$  and hence  $B \in \beta$  that

$$P_1(B) = \int_B h[T(\tilde{\omega})] dP_0(\tilde{\omega}) \quad (59)$$

But comparing (58) and (59), we have  $f(\tilde{\omega}) = h[T(\tilde{\omega})]$ ; that is, the Radon-Nikodyn derivative (likelihood functional) for the  $(y_t, t \in T)$  process is

$$h(\tilde{\omega}) = f(T^{-1}\tilde{\omega})$$

Since  $\tilde{\omega} = z_t$ , this can be written

$$h(x_t) = f^{-1}[g(x_t)]$$

Appendix  
PHOTOCHROMIC MATERIALS IN HOLOGRAPHY

### A.1. INTRODUCTION

During the past year an extensive program was designed to investigate the capabilities of photochromic materials as three-dimensional recording media for holographic data and to investigate their utilization in real-time processing. These materials included F-centered potassium bromide (KBr) crystals, silver halide glass, and a variety of photochromic plastics. A significant amount of data has been obtained that is directly applicable to construction of holograms, including

- (1) Exposure sensitivity
- (2) Angular orientation sensitivity
- (3) Diffraction efficiency
- (4) Wavelength sensitivity
- (5) Reciprocity failure
- (6) Temperature effects

This section presents a large part of these results and also contains information on our experiments with multiple-image storage and multicolor wavefront reconstruction.

### A.2. EXPOSURE SENSITIVITY

One of the properties of photochromic materials that makes them potentially useful is the occurrence of a change in optical transmission during exposure to a source of radiation of the proper wavelength. Because this change in transmission is concurrent with the exposure process, no developing is required as is usually the case in photographic emulsions. In addition, this change can be reversed by reilluminating the photochromic material with a different wavelength.

It is important to determine the amount of energy that is required to cause a certain change in the optical transmission. These changes, or exposure characteristics, can be presented in several ways: amplitude transmittance vs. exposure, density vs. exposure, and density vs. logarithmic exposure. This report presents plots of amplitude transmittance vs. exposure which can be used to determine the sensitivity (time of exposure), the region of linear response, and the operating point which obtains maximum diffraction.

The exposure sensitivity depends on many factors, including (1) type of photochromic material, (2) wavelength of illumination, (3) temperature, and (4) intensity of illumination (reciprocity). Amplitude transmittance vs. exposure was measured for photochromic materials from the American Cyanamid Company, KBr crystals from Carson Laboratories and silver halide photochromic glass from the Corning Glass Works. When appropriate, the wavelength, temperature, and intensity were varied. In this section, typical results for KBr crystals and photochromic glass are presented. The reciprocity effects will be discussed in section A.7.

A KBr crystal is first colored to maximum density with UV radiation and then bleached with 6328-Å light derived from the He-Ne laser. Experiments were performed in which a uniform beam was allowed to strike a previously colored crystal. The intensity of the light passing through the crystal was measured with a photomultiplier tube and recorded as a function of time by means of a chart recorder. From these data, amplitude transmittance vs. exposure curves were obtained. Figure 27 shows the results for several crystals.

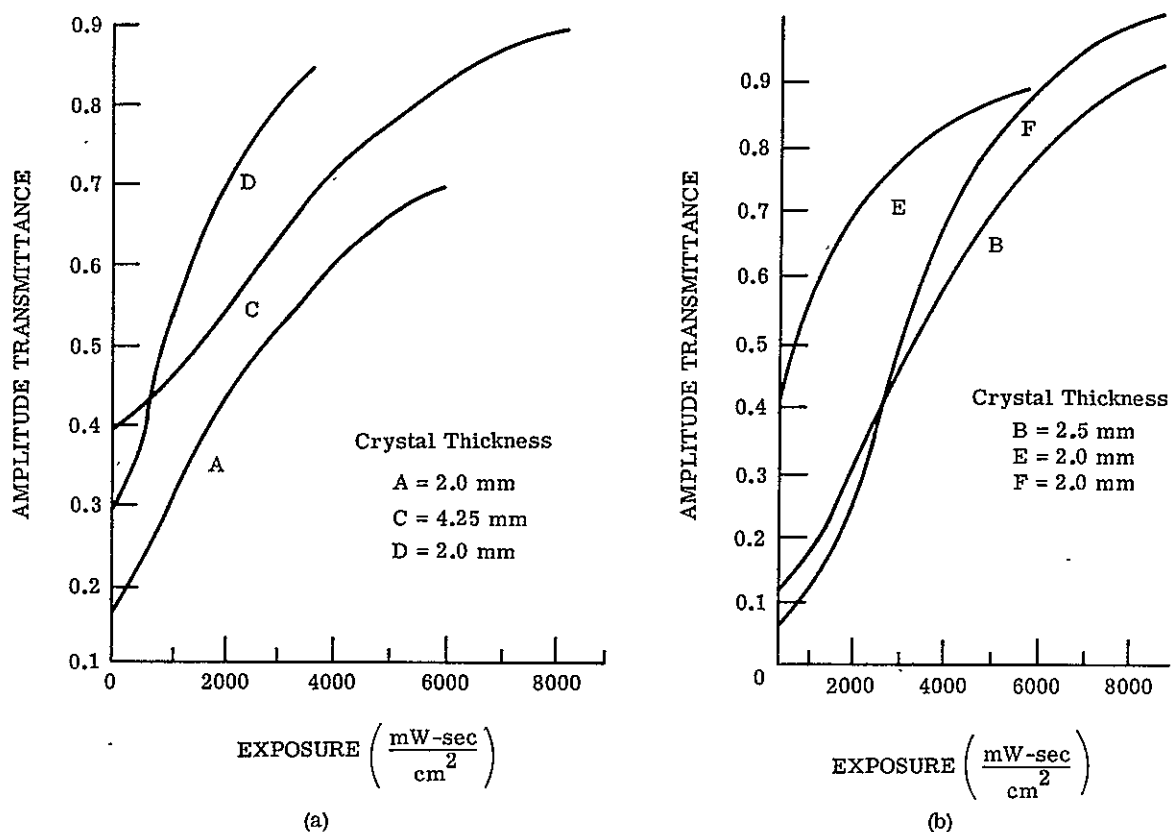


FIGURE 27. TRANSMITTANCE vs. EXPOSURE CHARACTERISTICS OF KBr CRYSTALS. Constant temperature of 80°C.

The effect of temperature on the sensitivity of the KBr crystals was determined by measuring amplitude transmittance vs. exposure while the crystal under test was held at a constant temperature with a thermoelectric heater unit. As shown in figure 28, the rate of bleaching increases as the temperature is raised. A temperature of 80°C is considered to be optimum by the manufacturers, since above 80°C, the thermal coloration effects tend to cancel any improvement in bleaching sensitivity.

Amplitude transmittance vs. exposure was also measured for samples of photochromic glass. Figure 29 shows results for three different wavelengths. All data were obtained at

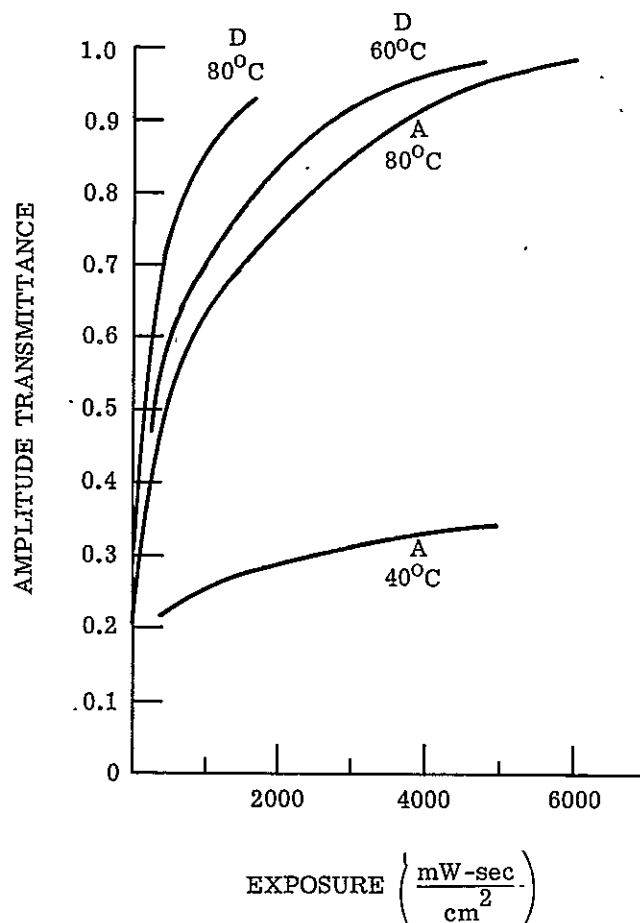


FIGURE 28. TRANSMITTANCE vs. EXPOSURE CHARACTERISTICS OF KBr CRYSTALS SHOWING THE EFFECT OF TEMPERATURE VARIATIONS

room temperature. The fact that this photochromic material is sensitive to a range of wavelengths indicates its application to multicolor holography (see sec. A.9).

The exposure sensitivity data presented here show that for typical intensities used in holography ( $<1 \text{ mW/cm}^2$ ), the exposure times may be on the order of several minutes. The sensitivity of these materials is approximately  $10^4$  times less than Kodak 649F spectroscopic plates.

The shape of the amplitude transmittance vs. exposure curves for KBr crystals can be justified analytically by assuming that the optical density  $D$  is directly proportional to the number of color centers  $N$  in the crystal. That is,

$$D = aN = \log \frac{1}{T}$$

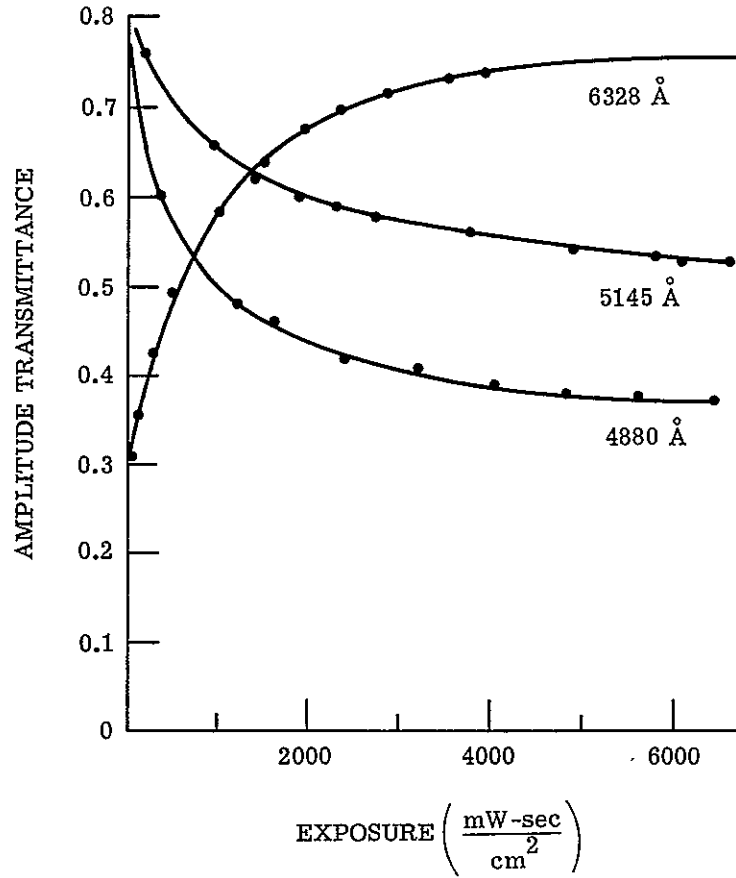


FIGURE 29. TRANSMITTANCE vs. EXPOSURE CHARACTERISTICS OF PHOTOCHROMIC GLASS SHOWING EFFECT OF WAVELENGTH VARIATIONS

where  $T_i = \frac{I_{out}}{I_{in}}$  is the intensity transmission. The energy per unit area absorbed in the crystal is  $(I_{in} - I_{out}) \Delta t$ . In turn, this quantity is proportional to the decrease in the number of color centers,

$$(I_{in} - I_{out})t = -rN$$

where  $r$  is a proportionality constant related to the bleaching efficiency.

If we let  $I$  be the incident intensity, we have in the limit the following nonlinear differential equation

$$r \frac{dN(t)}{dt} = I(e^{-aN(t)} - 1)$$

and the solution is

$$N(t) = \frac{\ln\left(1 - N_0 a e^{-\frac{It}{r}}\right)}{a}$$

where  $N_0$  is the initial number of color centers.

Since

$$T_i = e^{-D(t)} = e^{-aN(t)} = \frac{1}{1 - N_0 a e^{-\frac{aIt}{r}}}$$

the amplitude transmittance  $T_a$  as a function of the exposure  $It$  is

$$T_a = \sqrt{\frac{1}{1 - N_0 a e^{-\frac{aIt}{r}}}}$$

The quantities  $N_0 a$  and  $\frac{a}{r}$  can be considered constants depending on the particular crystal. Figure 30 shows a typical curve which agrees quite closely with the experimental curves.

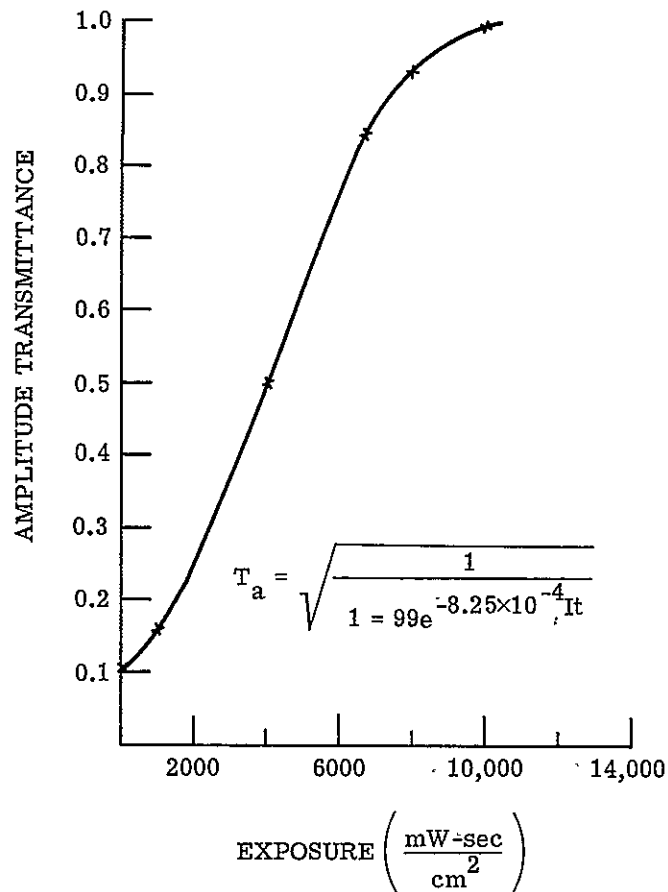


FIGURE 30. CALCULATED TRANSMITTANCE vs. EXPOSURE CHARACTERISTICS OF KBr CRYSTALS

### A.3. ANGULAR ORIENTATION SENSITIVITY

When the wavelength or the direction of incidence of the readout beam is varied continuously, there will be a corresponding change in the diffraction intensity from a hologram. The experimental methods used to determine the sensitivity of the hologram are either to vary the wavelength while the direction of incidence is fixed or to maintain a constant wavelength and vary the direction of incidence. The first method is difficult to implement because the wavelengths of available sources cannot be varied continuously. The second and most convenient method can be carried out experimentally by rotating the incident beam relative to the hologram, or by rotating the hologram relative to the incident beam. It should be noted that the direction of incidence has two degrees of freedom. However, in all our experiments only one was employed.

**A.3.1. CALCULATED RESULTS.** The angular width between half-power points of the curve of diffracted intensity vs. readout-beam angle can be derived from existing x-ray diffraction theory and is given by

$$\Delta\theta_{1/2} = \sqrt{\frac{\ln 2}{\pi}} \cdot \frac{\lambda}{D \cos \theta_B}$$

where  $\lambda$  is the constructing and reconstructing illumination wavelength

$\theta_B$  is the Bragg angle

D is the effective thickness of the hologram

If the incidence angles of the reference beam and signal beam are denoted by  $\theta_r$  and  $\theta_s$  (see fig. 31), each impinging from the two sides of the normal to the hologram, then

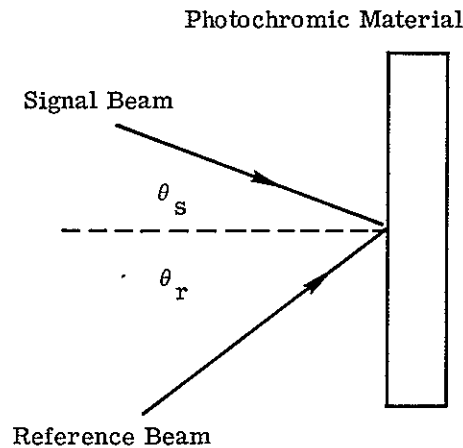


FIGURE 31. DIAGRAM OF ANGLE CONVENTION FOR REFERENCE AND SIGNAL BEAMS



$$\theta_B = \frac{\theta_s + \theta_r}{2}$$

and

$$D = \frac{t_o \sin \frac{(\theta_s + \theta_r)}{2}}{\cos \theta_s}$$

where  $t_o$  is the actual thickness of the hologram.

The half-power width becomes

$$\Delta\theta_{1/2} = \sqrt{\frac{\ell n 2}{\pi}} \cdot \frac{2\lambda \cos \theta_s}{t_o \sin (\theta_s + \theta_r)} \quad (60)$$

This equation was obtained on the assumption that the absorption and the interaction between incident and diffracted waves in the hologram can be neglected. As we shall subsequently demonstrate, the half-power width value in equation 60 is in good agreement with our experimental results. The approximate formula for  $\Delta\theta_{1/2}$  is indeed applicable to a variety of angular orientations and thicknesses of photochromic materials.

The equation for  $\Delta\theta_{1/2}$  represents the internal half-power width. By applying Snell's relation, we can determine  $\Delta\theta_{1/2}$  in terms of the external parameters

$$\Delta\theta_{1/2} = (\Delta\theta_{1/2})_{int} = \sqrt{\frac{\ell n 2}{\pi}} \frac{2 \frac{\lambda_{air}}{n} \cos \left[ \sin^{-1} \left( \frac{\sin \theta_{s_{air}}}{n} \right) \right]}{t_o \sin \left[ \sin^{-1} \left( \frac{\sin \theta_{s_{air}}}{n} \right) + \sin^{-1} \left( \frac{\sin \theta_{r_{air}}}{n} \right) \right]}$$

which can also be represented as

$$(\Delta\theta_{1/2})_{int} = \sqrt{\frac{\ell n 2}{\pi}} \left[ \frac{2\lambda_{air} \sqrt{n^2 - \sin^2 \theta_{s_{air}}}}{t_o \left( \sin \theta_{s_{air}} \sqrt{n^2 - \sin^2 \theta_{r_{air}}} + \sin \theta_{r_{air}} \sqrt{n^2 - \sin^2 \theta_{s_{air}}} \right)} \right]$$

In order to find the external half-power width value of the angular orientations  $(\Delta\theta_{1/2})_{air}$ , we reapply Snell's law to get

$$\sin \left[ \theta_{r_{air}} + \frac{1}{2} (\Delta\theta_{1/2})_{air} \right] = n \sin \left[ \sin^{-1} \left( \frac{\sin \theta_{r_{air}}}{n} \right) + \frac{1}{2} (\Delta\theta_{1/2})_{int} \right]$$

and

$$\sin \left[ \theta_{r \text{ air}} - \frac{1}{2} (\Delta \theta''_{1/2})_{\text{air}} \right] = n \sin \left[ \sin^{-1} \left( \frac{\sin \theta_{r \text{ air}}}{n} \right) - \frac{1}{2} (\Delta \theta_{1/2})_{\text{int}} \right]$$

and finally

$$(\Delta \theta_{1/2})_{\text{air}} = \frac{1}{2} (\Delta \theta'_{1/2})_{\text{air}} + \frac{1}{2} (\Delta \theta''_{1/2})_{\text{air}}$$

If the small-angle approximation of  $\sin \Delta \theta = \Delta \theta$  is used, we then obtain the following relation

$$(\Delta \theta_{1/2})_{\text{air}} = (\Delta \theta_{1/2})_{\text{int}} \frac{\sqrt{n^2 - \sin^2 \theta_{r \text{ air}}}}{\cos \theta_{r \text{ air}}}$$

and in more complete form

$$(\Delta \theta_{1/2})_{\text{air}} = \sqrt{\frac{\ell n^2}{\pi}} \left( \frac{2\lambda}{t_0} \right) \left[ \frac{\sqrt{n^2 - \sin^2 \theta_r} \sqrt{n^2 - \sin^2 \theta_s}}{\cos \theta_r \left( \sin \theta_s \sqrt{n^2 - \sin^2 \theta_r} + \sin \theta_r \sqrt{n^2 - \sin^2 \theta_s} \right)} \right]_{\text{air}} \quad (61)$$

This relation was used in all our calculations. Using equation 61, we have calculated the half-power width as a function of hologram thickness and as a function of reference beam and signal beam orientations. The results are shown in figures 32 through 35. The curves shown in figure 28 depict the calculated external half-power width as a function of hologram thickness for three different offset angles. The offset angle, which is the angle subtended between the reference beam and signal beam, was chosen so that its bisector is the normal to the hologram plane. The fringe surfaces were thus perpendicular to the hologram medium and spacing between these fringe surfaces decreased with higher offset angle. In all instances, the  $\Delta \theta_{1/2}$  is inversely proportional to the thickness.

The curve shown in figure 33 shows the half-power width as a function of incidence angle. Here  $\theta_r = \theta_s = \theta$ , so that the fringe surfaces are again perpendicular to the surface of the recording medium.

The external half-power width as a function of the reference beam angle, for different signal beam angles, is shown in figure 34. The thickness  $t_0$  represents a typical value and is a constant for these curves. Finally, we calculated the half-power width as a function of reference beam angle, with the offset angle kept constant. The resulting data are shown in figure 35.

As is evident from figures 33 and 34, there is an optimum value of  $\theta_r$  for which the angular orientation sensitivity is maximized. By differentiating  $(\Delta \theta_{1/2})_{\text{air}}$  with respect to  $\theta_r$  and setting the result equal to zero, we have determined this optimum  $\theta_r$  when  $\theta_r = \theta_s$ , and  $n$  and  $\theta_s$  are fixed. For the first condition we obtain the relation

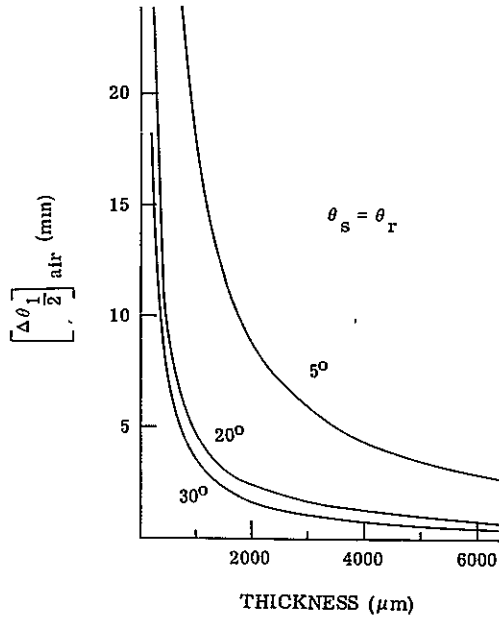


FIGURE 32. CALCULATED HALF-POWER WIDTH AS A FUNCTION OF HOLOGRAM THICKNESS FOR DIFFERENT OFFSET ANGLES.  $n = 1.49$ ,  $\lambda = 6328 \text{ \AA}$ ,  $\theta_r = \theta_s$ .

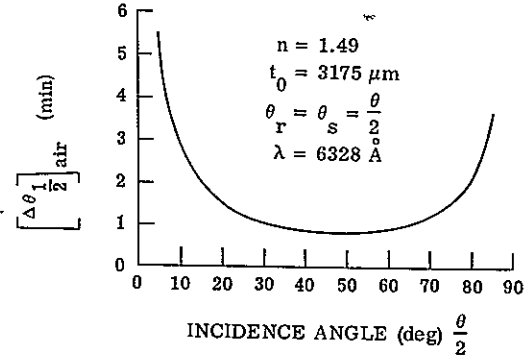


FIGURE 33. CALCULATED HALF-POWER WIDTH AS A FUNCTION OF INCIDENCE ANGLE.  $n = 1.49$ ,  $\lambda = 6328 \text{ \AA}$ ,  $\theta_r = \theta_s$ ,  $t_0 = 3175 \mu$ .

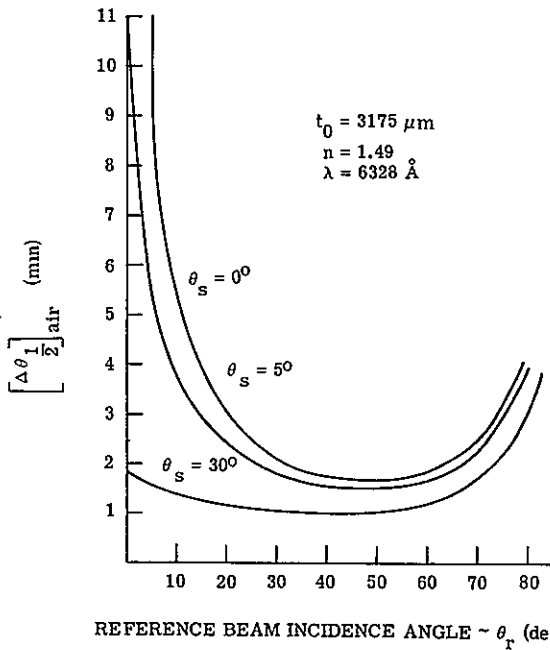


FIGURE 34. CALCULATED HALF-POWER WIDTH AS A FUNCTION OF REFERENCE ANGLE FOR DIFFERENT SIGNAL BEAM ANGLES.  $n = 1.49$ ,  $\lambda = 6328 \text{ \AA}$ ,  $t_0 = 3175 \mu\text{m}$ .

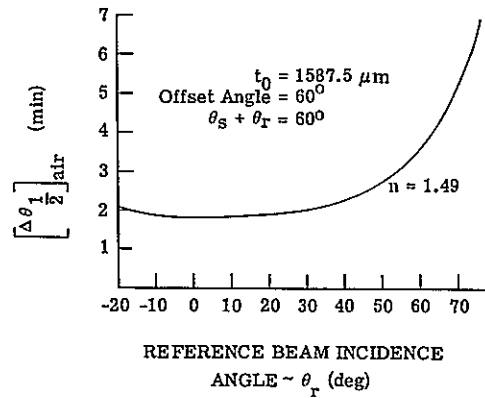


FIGURE 35. CALCULATED HALF-POWER WIDTH AS A FUNCTION OF REFERENCE ANGLE WITH A FIXED OFFSET ANGLE OF  $60^\circ$ .  $t_0 = 1587.5 \mu\text{m}$ .

$$n^2 = \frac{\sin^4 \theta_{r \text{ opt}}}{2 \sin^2 \theta_{r \text{ opt}} - 1}$$

Using this relation, we calculated  $\theta_r$  as a function of the index of refraction  $n$ . A plot of the resulting data is shown in figure 36. The same results were also obtained when  $\theta_s = 0$ . For silver halide photochromic glass,  $n = 1.49$  and consequently the optimum  $\theta_r$  is found to be  $49.2^\circ$ .

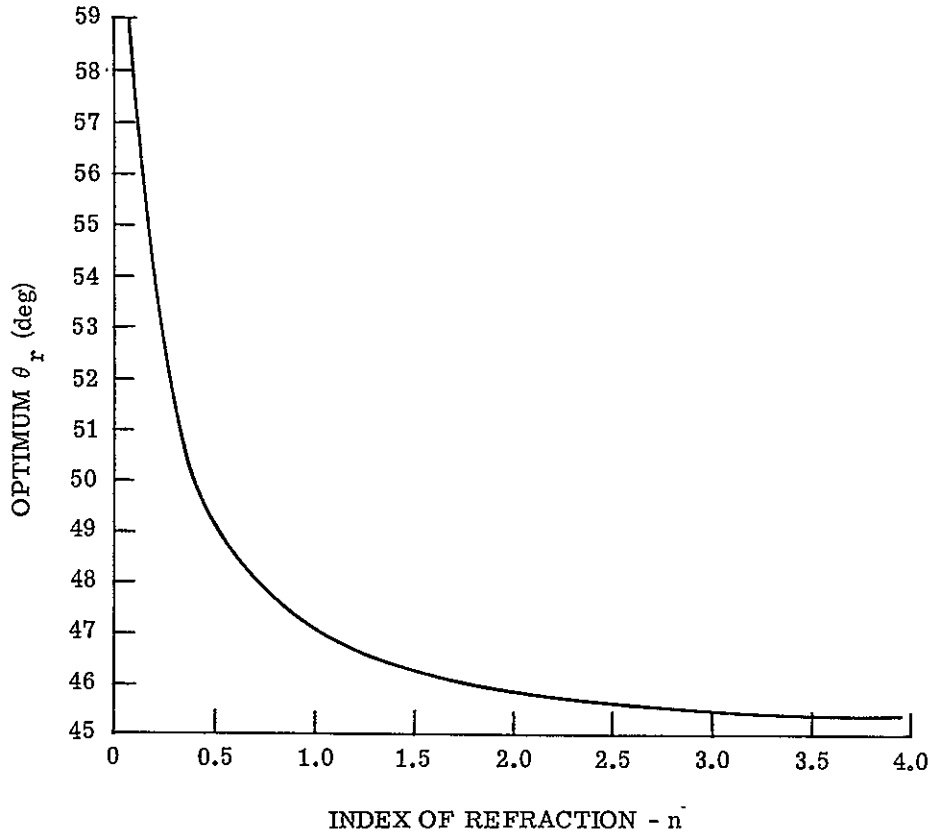


FIGURE 36. CALCULATED OPTIMUM REFERENCE BEAM ANGLE AS A FUNCTION OF THE REFRACTIVE INDEX OF THE RECORDING MEDIUM.  $\theta_r = \theta_s$  or  $\theta_s = 0$ .

For the more general condition of a fixed  $\theta_s$ , we obtain the following relation

$$\frac{n^2 - \sin^2 \theta_s}{\sin^2 \theta_s} = \frac{\sin^2 \theta_{r \text{ opt}} \left( n^2 - \sin^2 \theta_{r \text{ opt}} \right)^3}{\left( \sin^4 \theta_{r \text{ opt}} - 2n^2 \sin^2 \theta_{r \text{ opt}} + n^2 \right)^2}$$

Using this relation, we have determined  $\theta_{r\text{opt}}$  as a function of  $\theta_s$  for different fixed  $n$ . The resulting data were then plotted and are shown in figure 37.

As is clearly indicated in our calculated results, the maximum angular orientation sensitivity, and consequently the least interaction between successive images, occurs at some optimum angle of incidence. This optimum angle is primarily a function of the index of refraction of the hologram medium  $n$  and to some extent a function of signal beam angular orientation  $\theta_s$ .

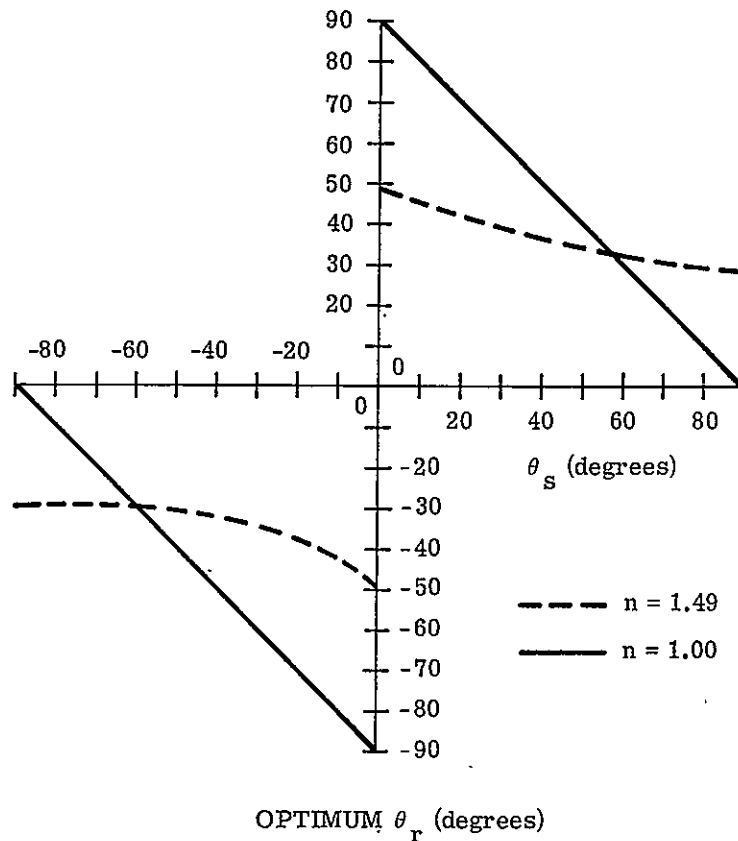


FIGURE 37. CALCULATED OPTIMUM REFERENCE BEAM ANGLE AS A FUNCTION OF SIGNAL BEAM ANGLE.  $n = 1.49$ ,  $n = 1.0$ .

A.3.2. EXPERIMENTAL RESULTS. All of our experiments involve the recording of simple interference gratings which result from the interference of two plane waves. The effect of different hologram thicknesses and different offset angles between the reference beam and signal beams was determined. The recording medium was either KBr crystals or silver halide glass. For comparison purposes, we also used the Kodak 649F spectroscopic plates which have a nominal emulsion thickness of  $15\ \mu\text{m}$ .

The experimental setup is shown in figure 38. The light from the laser is split into two paths by the beam splitter and subsequently diverted by the mirrors to the photochromic sample. The pinhole assemblies and collimating lenses expand and collimate the beam. The result is that two plane waves,  $I_r$  and  $I_s$ , interfere at the sample. Experiments were performed in which the interference pattern was recorded for various values of the angle  $\theta$  between the two beams and for various angular orientations of the photochromic material with respect to the light beams. The orientation can be adjusted with great precision by means of a motor-driven platform. The angle  $\theta$  was changed by relocating the optical components.

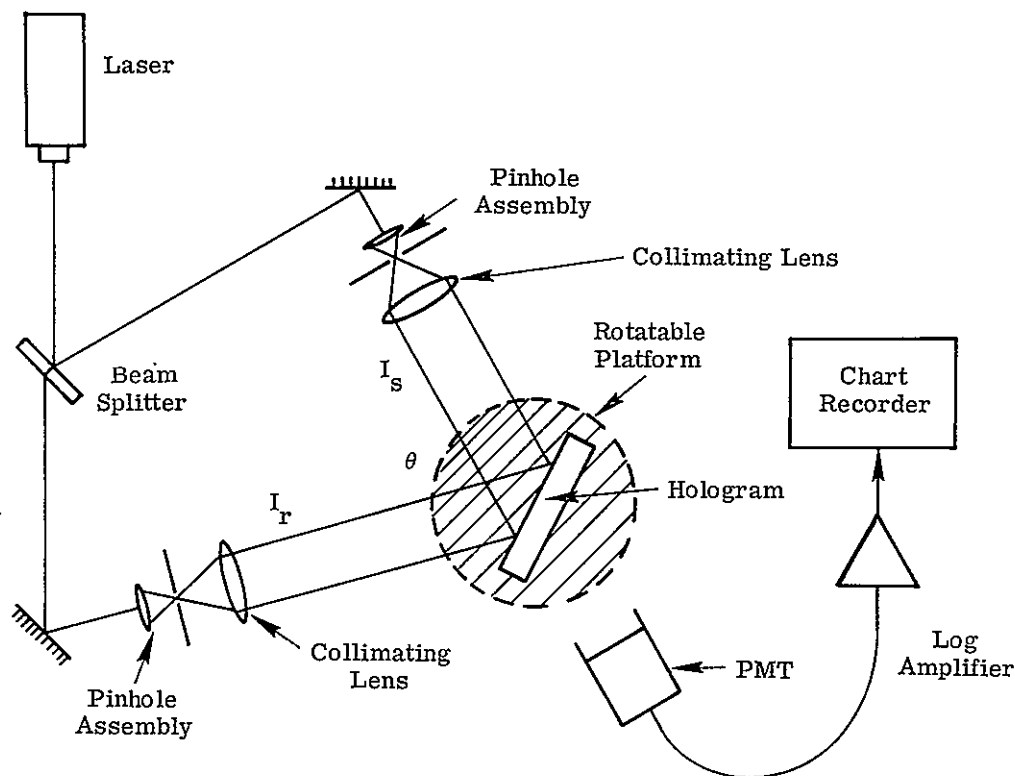


FIGURE 38. DIAGRAM OF SETUP FOR ANGULAR ORIENTATION SENSITIVITY MEASUREMENTS

During readout, only the  $I_r$  beam was allowed to be incident on the photochromic material. The intensity of the diffracted beam was measured with a photomultiplier tube. The resulting voltage was then fed into a paper chart recorder via a logarithmic amplifier. By rotating the photochromic at a constant rate, the relative intensity of the diffracted light was continuously plotted as a function of the incidence angle of the readout wave.

It should be noted that the angle of diffraction  $\theta_d$  must satisfy the grating equation

$$\sin \theta_i + \sin \theta_d = \frac{\lambda}{d}$$

where  $\lambda$  is the wavelength of the readout wave

$d$  is the fringe spacing of the grating

$\theta_i$  is the angle of incidence of the readout wave

$\theta_d$  is the angle of the diffracted wave

In our measurements, the readout source and the photomultiplier tube remained fixed while the three-dimensional grating was rotated. This means that the relation between  $\theta_i$  and  $\theta_d$  implied by the experimental configuration is that the sum of the incidence angle of the readout wave and the angle of diffraction is a constant. Figure 39 shows an example to illustrate this point. The curved line represents the actual variation based on the grating equation, whereas the straight line is the assumed variation. The difference between the two curves represents an experimental error. Since the curves coincide at the Bragg angle and remain extremely close for several degrees on either side, the error is negligible if measurements are confined to this region. Moreover, the orientation sensitivity of the thick recording materials under investigation here is so great that very little light is diffracted when the incidence angle of the readout wave differs from the Bragg angle by more than several minutes of arc.

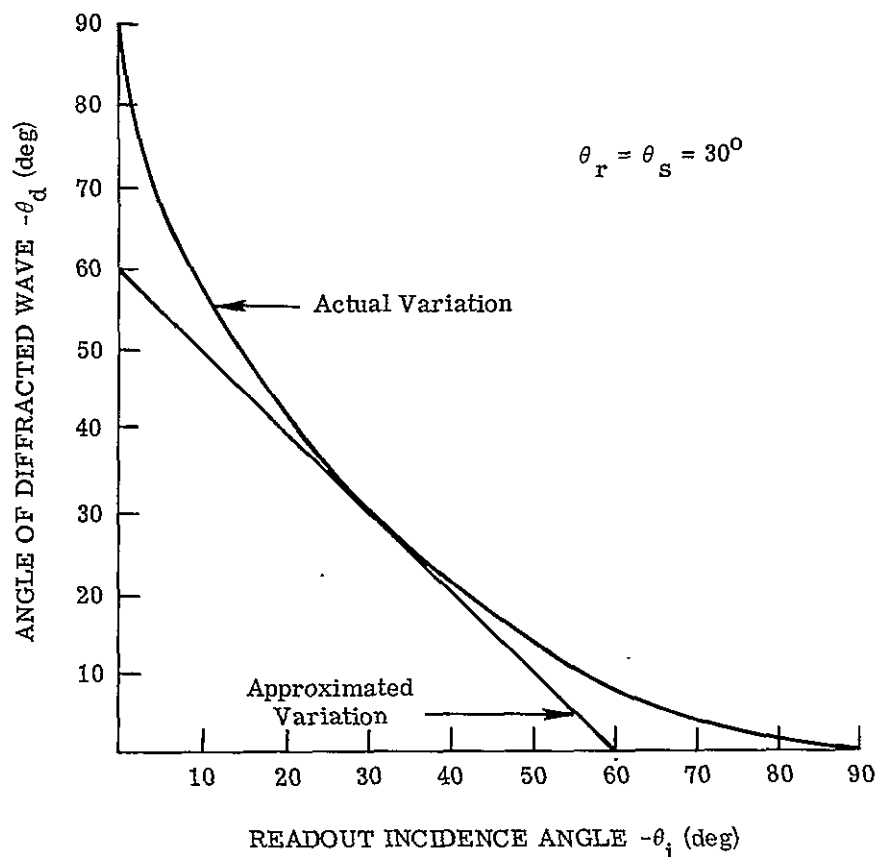


FIGURE 39. CURVE REPRESENTING ERROR DUE TO FIXED PHOTOMULTIPLIER POSITION

Because of this, it was not necessary in these experiments to track the diffracted beam or use a collecting lens when measuring the intensity while the photochromic sample was being rotated.

Several examples of the experimental results are shown in figures 40, 41, and 42. Figure 40 shows the relative diffracted intensity as a function of incidence angle of the readout beam for KBr crystals with two different thicknesses and offset angles. Similarly, figure 41 shows results obtained from photochromic glass of three different thicknesses. Figures 41d, e, and f demonstrate the change in orientation sensitivity due to different reference beam angles even though the angle between the signal beam and reference beam is held constant. For comparison purposes, an orientation sensitivity curve obtained for Kodak 649F spectroscopic plates is shown in figure 42.

The half-power width of the angular orientation sensitivity curves was determined from the experimental data and compared with calculated results. These data are shown in table II. Good agreement between calculated and experimental results is clearly evident.

#### A.4. DIFFRACTION EFFICIENCY

Diffraction efficiency is defined as the ratio of the diffracted light intensity to the incident light intensity. The experimental setup for measuring diffraction efficiency was essentially the same as that used in the orientation sensitivity experiments (see fig. 38). Simple interferograms of two monochromatic ( $6328\text{-}\text{\AA}$ ) plane waves were recorded in the photochromic materials under investigation. In the reconstruction process a plane wave was also used and the percentage of light diffracted by the photochromic was measured by means of a photomultiplier tube.

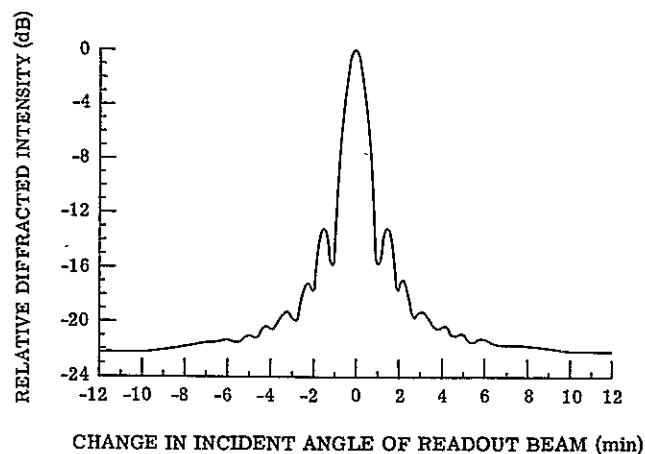
Efficiencies were measured for interference gratings made with different exposure times, reference-beam-to-signal-beam ratios, and different spatial frequencies of the fringes as determined by the angle between the two beams. Typical results obtained for KBr crystals range from 0.002% to 0.175% for exposures of  $480 \frac{\text{mW-sec}}{\text{cm}^2}$  and  $2400 \frac{\text{mW-sec}}{\text{cm}^2}$ , respectively, with an offset angle of  $40^\circ$ . Figure 43 shows the variation in diffraction efficiency as a function of exposure with relatively low exposures of photochromic glass.

If an interferogram is recorded in a photochromic material and then reilluminated with one of the beams of light, the diffraction efficiency will decrease as shown in figure 44. This behavior has important consequences in the multiple-image storage problem which is discussed in section A.5.

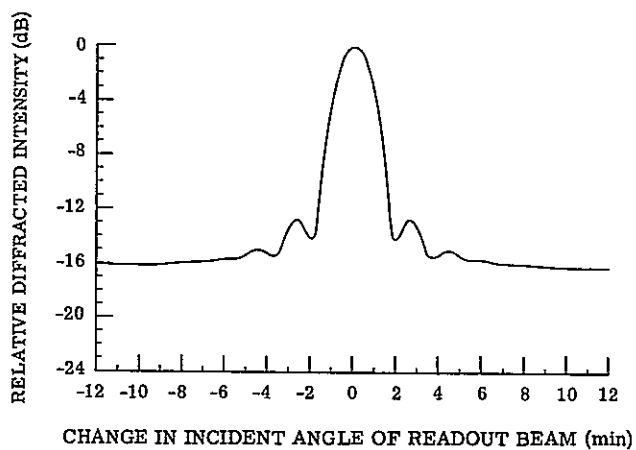
#### A.5. MULTIPLE-IMAGE STORAGE

One of the more important reasons for using a three-dimensional recording medium is its potential application to the storage of multiple signals. In this section we will discuss the

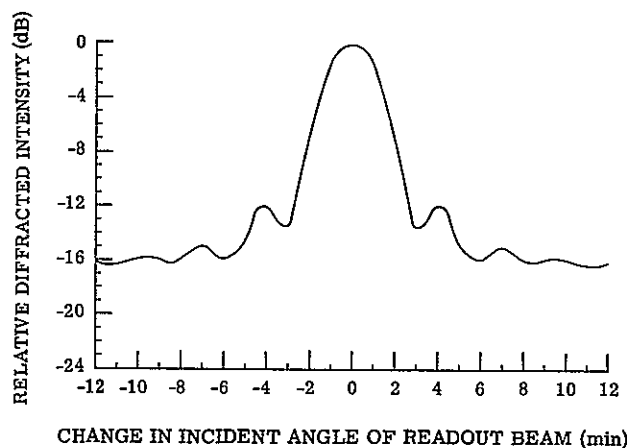




(a) Thickness = 4.25 mm. Offset angle =  $60^\circ$ ,  $\theta_r = \theta_s = 30^\circ$ .

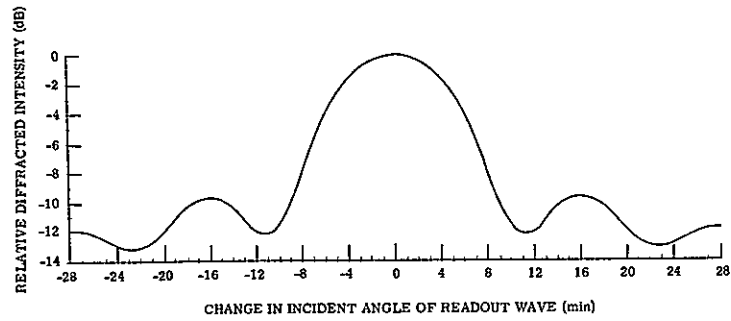


(b) Thickness = 2 mm. Offset angle =  $60^\circ$ ,  $\theta_r = \theta_s = 30^\circ$ .

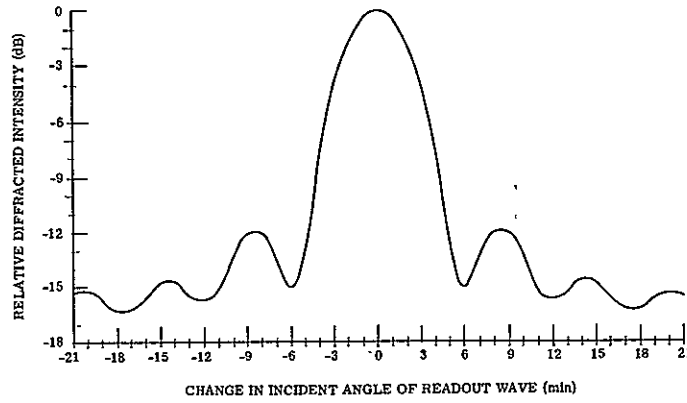


(c) Thickness = 2 mm. Offset angle =  $40^\circ$ ,  $\theta_r = \theta_s = 20^\circ$ .

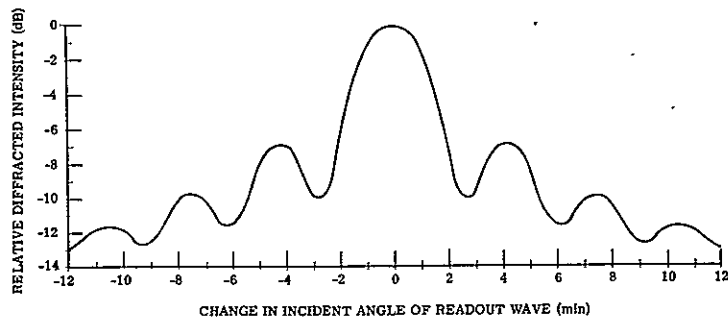
FIGURE 40. EXPERIMENTAL RESULTS OF ANGULAR ORIENTATION SENSITIVITY MEASUREMENTS OF KBr CRYSTALS



(a) Thickness = 1587.5  $\mu\text{m}$ . Offset angle =  $10^\circ$ ,  $\theta_r = \theta_s = 5^\circ$ .

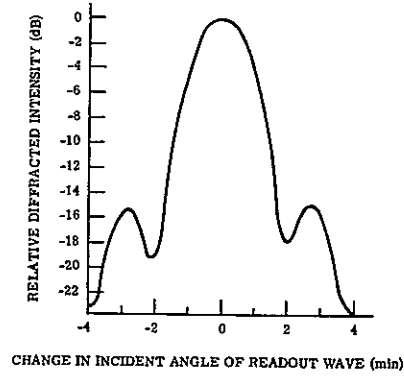


(b) Thickness = 3175  $\mu\text{m}$ . Offset angle =  $10^\circ$ ,  $\theta_r = \theta_s = 5^\circ$ .

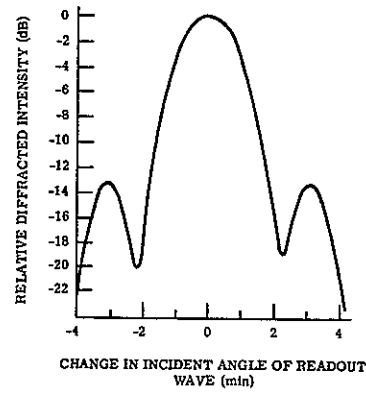


(c) Thickness = 6350  $\mu\text{m}$ . Offset angle =  $10^\circ$ ,  $\theta_r = \theta_s = 5^\circ$ .

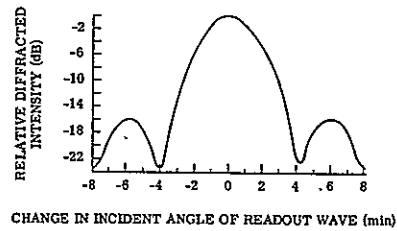
FIGURE 41. EXPERIMENTAL RESULTS OF ANGULAR ORIENTATION SENSITIVITY MEASUREMENTS OF SILVER HALIDE GLASS



(d) Thickness = 1587.5  $\mu\text{m}$ . Offset angle =  $60^\circ$ ,  $\theta_r = 0^\circ$ ,  $\theta_s = 60^\circ$ .



(e) Thickness = 1587.5  $\mu\text{m}$ . Offset angle =  $60^\circ$ ,  $\theta_r = 30^\circ$ ,  $\theta_s = 30^\circ$ .



(f) Thickness = 1587.5  $\mu\text{m}$ . Offset angle =  $60^\circ$ ,  $\theta_r = 60^\circ$ ,  $\theta_s = 0^\circ$ .

FIGURE 41 EXPERIMENTAL RESULTS OF ANGULAR ORIENTATION SENSITIVITY MEASUREMENTS OF SILVER HALIDE GLASS (Continued)

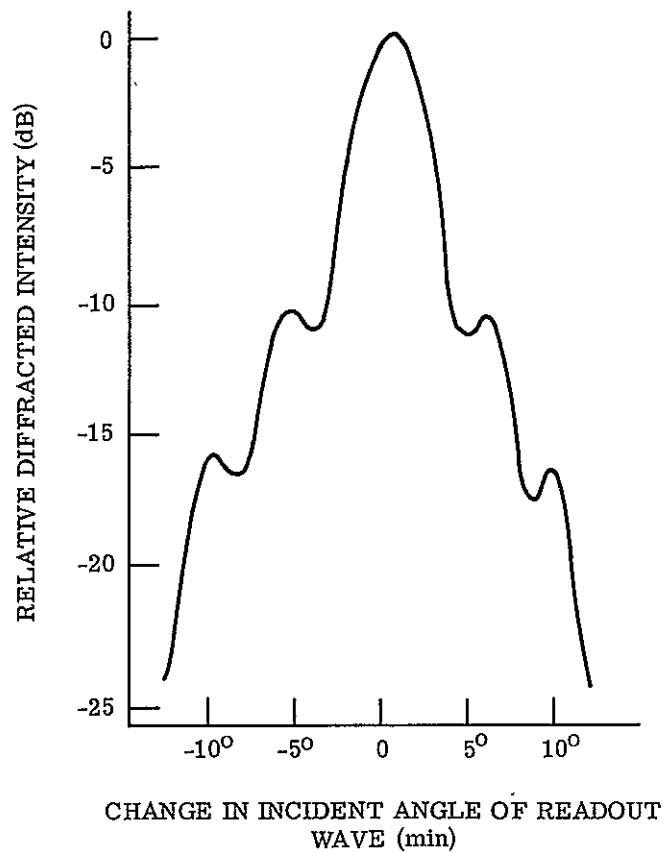


FIGURE 42. EXPERIMENTAL RESULTS OF ANGULAR ORIENTATION SENSITIVITY MEASUREMENTS OF KODAK 649-F SPECTROSCOPIC PLATES. Offset angle =  $60^\circ$ ,  $\theta_r = \theta_s = 30^\circ$ .

TABLE II. COMPARISON OF CALCULATED VALUES OF HALF-POWER WIDTH OF ANGULAR ORIENTATION SENSITIVITY CURVE WITH EXPERIMENTAL VALUES

Reference Beam Angle $\theta_r$ (deg)	Signal Beam Angle $\theta_s$ (deg)	Thickness ( $\mu\text{m}$ )	Calculated Half- Power Width (min)	Experimental Value of Half- Power Width (min)
60	0	1587.5	3.6	3.2
30	30	1587.5	2.1	2.0
0	60	1587.5	1.8	1.7
5	5	1587.5	11.0	10.9
5	5	3175.0	5.5	5.3
5	5	6350.0	2.75	2.8

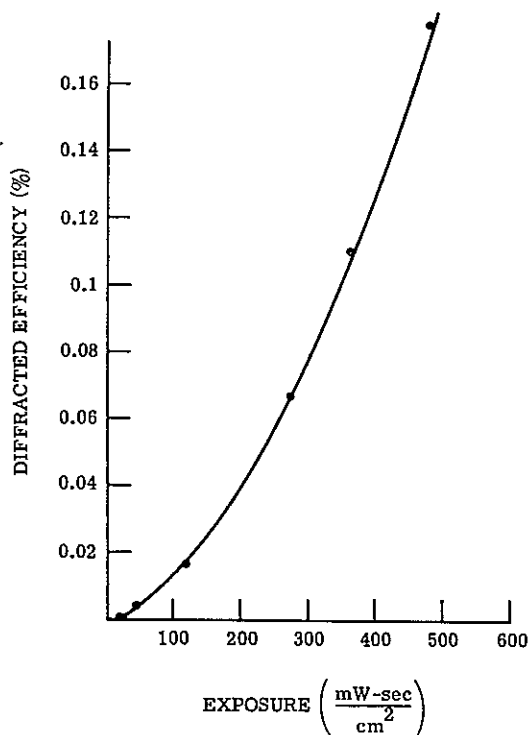


FIGURE 43. CURVE OF DIFFRACTION EFFICIENCY AS A FUNCTION OF EXPOSURE LEVELS FOR SILVER HALIDE GLASS. Thickness =  $3175 \mu$ ,  $I_r = I_s = 0.2 \text{ mW/cm}^2$ ,  $\theta_r = \theta_s = 5^\circ$ .

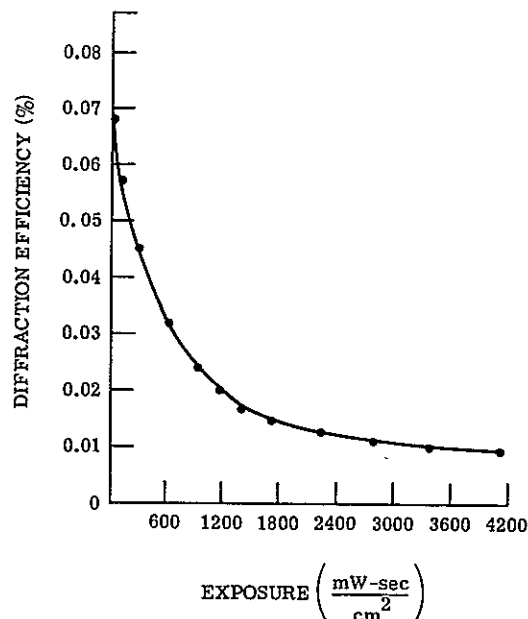


FIGURE 44. CURVE ILLUSTRATING REDUCTION OF DIFFRACTION EFFICIENCY DURING RECONSTRUCTION. Thickness =  $3175 \mu$ ,  $I_r = I_s = 0.27 \text{ mW/cm}^2$ ,  $\theta_r = \theta_s = 5^\circ$ , exposure time = 10 min.

practical aspects of the photochromic devices in actual system operation and the problems encountered.

The Bragg discrimination must be considered in relation to limitations imposed on the number of holographically stored signals, when we store many complex images each constructed with a differently oriented reference beam. With photographic plates having an emulsion thickness of  $15 \mu\text{m}$ , the average change of orientation between each successive image with little interaction is  $10^\circ$ . The angular orientation sensitivity is quite low at low offset angles and increases with higher offset angles. Since the available angular orientation in constructing a conventional hologram is  $180^\circ$ , we are confined to storage of only 18 images. With special coding techniques, separation of images, and wavelength variations, the calculated number of stored images can be significantly increased. In this section we deal solely with Bragg holography.

A calculated increase of two to three orders of magnitude can be achieved in stored images with existing photochromic materials. In practice, however, the primary limitation is not the number of images. The diffracted intensities of recordings made early in a sequence of equal recordings are either below the noise level or at best very weak. This anomalous behavior,

which is peculiar to photochromic materials and is not evident in photographic material, is believed to be caused by some nonlinear bleaching effect. Assuming that the photochromic material is comprised of a large number of layers of equal thickness, the layer closest to the illumination source is partially bleached with the first recorded image. Illumination of subsequent images continues to bleach the first layer and penetrates into the inner layers. The cumulative bleaching of the first layer continues until the saturation point when the recorded information about the first image is obliterated. This process is then repeated at the second layer, at the third layer, and so on, each time obliterating the recorded information or reducing the recorded fringe contrast and thereby lowering the diffraction efficiency. We have performed a number of experiments which demonstrate the nonlinear bleaching behavior in photochromic glass and KBr crystals and have found that the latter create the most difficult problems.

Early experiments involved the recording of simple interference patterns of two plane waves, each at a different orientation of the photochromic material. To date a sequence of 40 separate gratings, each incoherent with the others, has been successfully recorded in the KBr crystals, whereas around 200 gratings were recorded in the photochromic glasses. Two examples of these results which illustrate the cumulative bleaching problem are shown in figure 45 and figure 46. The curves represent fluctuations in diffracted intensity as the orienta-

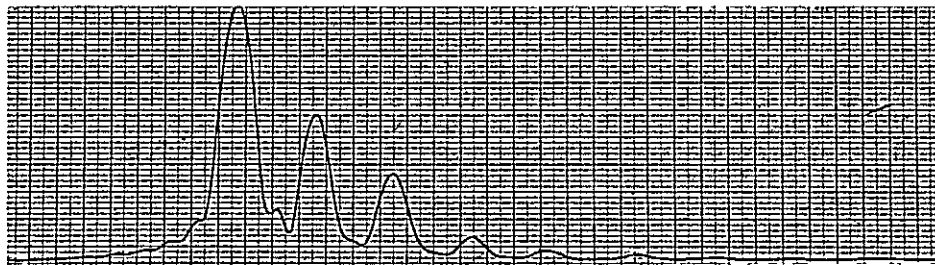


FIGURE 45. EFFECT OF NONLINEAR BLEACHING ON KBr CRYSTALS



FIGURE 46. EFFECT OF NONLINEAR BLEACHING ON SILVER HALIDE GLASS

tion of the incident illumination with respect to the photochromic medium is continuously altered. The angular separation between recordings was sufficiently large so that the  $\frac{\sin x}{x}$  structure for some recordings is clearly evident.

For the examples shown in figures 45 and 46, 10 recordings were made in each medium. The average offset angle was approximately  $10^\circ$  and the change in angular orientation between each recording was approximately four minutes of arc. The intensities of the reference beam and signal beam were  $2 \text{ mW/cm}^2$  and the exposure time for each recording was five minutes. For the KBr crystal, the effect of nonlinear bleaching is dramatically demonstrated in figure 45. The diffracted intensity of the tenth recording is shown at the extreme left and is the highest. The diffracted intensities of the earlier recordings decrease down to the sixth recording, and the remainder cannot be detected. The situation is improved for the photochromic glass, and in figure 46 the diffracted intensity variations for all 10 recordings can be seen clearly. The diffracted intensity of the tenth recording is on the extreme right and although there is some effect of nonlinear bleaching, it is not significant.

We also recorded 100 relatively complex diffraction patterns in one hologram on the 1/8-inch-thick photochromic glass. The patterns resulted from the interference between plane waves of the reference beam and complex waves from the signal beam. A sequence of 100 diffusely illuminated transparencies were used as objects, each having a bandwidth of approximately 150 lines/mm. Exposure times for each recording ranged from two to three minutes, and angular orientation (between reference beam and hologram) was changed by four minutes of arc to separate each recording.

Finally, the reconstructed image of each recording was investigated. A representative sample of the results is shown in figure 47. As expected, the signal-to-noise ratio for the later recordings was relatively high, providing reconstructed images of high quality. As is evident from the results shown in figure 47a and b, the signal-to-noise ratio of the reconstructed images is significantly degraded in the earlier recordings, but in no instance were the images totally obliterated. It is believed that by optimizing the illumination intensities and exposure time, 200 or 300 complex recordings can easily and effectively be stored in existing materials.

An illustration of the excellent Bragg discrimination capabilities for photochromic glass is shown in figure 48. There is very little if any, interaction between recordings. The objects chosen were transparencies showing the face of a time clock. The first recording was made at 0 minutes and 0 seconds and in subsequent recordings the second hand was advanced by 15 seconds. On readout, if the hologram is given continuous angular motion, the reconstructed image of the clock face appears to have its second hand move continuously. This, in effect, is a stored movie. The 100 recordings in the photochromic material replace 100 frames of strip film.



(a) Image from Fifth Recording



(b) Image from Twentieth Recording



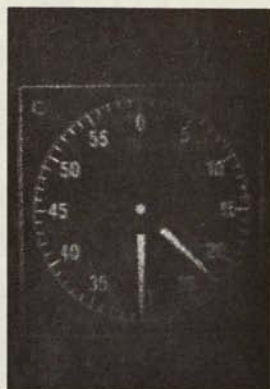
(c) Image from Sixtieth Recording



(d) Image from Eightieth Recording

FIGURE 47. RECONSTRUCTED IMAGES FROM A MULTIPLE-EXPOSURE HOLOGRAM OF 100 RECORDINGS. Angular separation between each recorded image is 4 min of arc.





(e) Image from Ninetieth Recording

FIGURE 47. RECONSTRUCTED IMAGES FROM A MULTIPLE-EXPOSURE HOLOGRAM OF 100 RECORDINGS (Continued)

#### A.6. SHRINKAGE EFFECTS

The presence of shrinkage in three-dimensional recording media generally causes a change in both orientation and spacing of the fringe surfaces in the hologram. As a consequence of this change, either the orientation or the wavelength of the reconstructing beam must be altered to maximize the diffracted intensity. In both instances, the location of the reconstructed image will also change. In photographic material, the shrinkage is caused by the emulsion shrinkage that occurs during chemical processing. In photochromic crystal, the shrinkage is due to reduction of temperature between readin and readout.

The shrinkage phenomenon in KBr crystals was investigated by calculating the effect of temperature reduction in the crystals on the orientation of the reconstructing beam and confirmed our results experimentally. A simple grating hologram formed by the interference of two coherent plane waves was used. In three-dimensional media, the recorded interference pattern is composed of parallel plane surfaces. The orientation and frequency of these surfaces are described in relation to the schematic illustration of figure 49. For simplification, symmetrical orientation for the two plane waves was chosen which produced fringe surfaces perpendicular to the surface of the recording medium. The spacing of the recorded fringes  $d$  obeys the Bragg relation

$$d = \frac{\lambda}{2 \sin \theta}$$



(a) Image from Sixty-first Recording



(b) Image from Sixty-second Recording



(c) Image from Sixty-third Recording



(d) Image from Sixty-fourth Recording

FIGURE 48. RECONSTRUCTED IMAGES FROM A MULTIPLE-EXPOSURE HOLOGRAM OF 100 RECORDINGS ILLUSTRATING BRAGG DISCRIMINATION CAPABILITIES. Angular separation between each recorded image is 4 min of arc.



(e) Image from Sixty-fifth Recording

FIGURE 48. RECONSTRUCTED IMAGES FROM A MULTIPLE-EXPOSURE HOLOGRAM OF 100 RECORDINGS ILLUSTRATING BRAGG DISCRIMINATION CAPABILITIES (Continued)

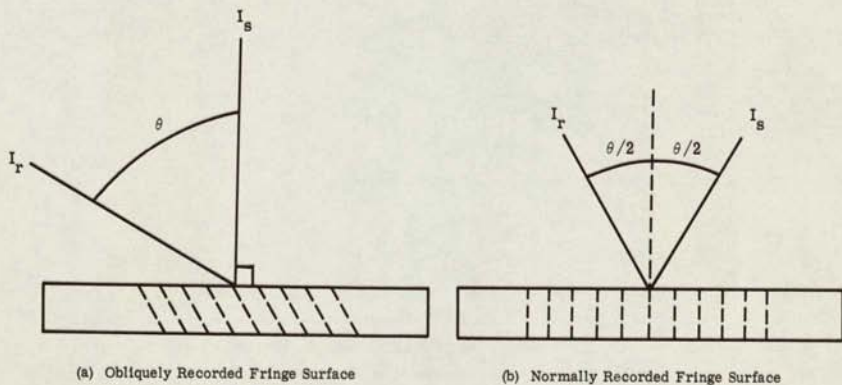


FIGURE 49. DIAGRAM ILLUSTRATING FRINGE SURFACES AND ORIENTATION OF WAVES

where  $\lambda$  is the illumination wavelength, and  $\theta$  is half the angle subtended between the two plane waves.

Using the thermal expansion coefficient of  $43 \times 10^{-6}/^{\circ}\text{C}$  for KBr and denoting the temperature difference between readin and readout as  $\Delta T$ , we obtain an expression for the fringe spacing after contraction

$$d' = (1 - 43 \times 10^{-6} \times \Delta T) \frac{\lambda}{2 \sin \theta}$$

The angle satisfying the Bragg relation for the contracted case is

$$\sin \theta' = \frac{\sin \theta}{1 - 43 \times 10^{-6} \Delta T}$$

and the required angular reorientation between readin and readout becomes

$$\theta' - \theta = \sin^{-1} \left( \frac{\sin \theta}{1 - 43 \times 10^{-6} \Delta T} \right) - \theta \quad (62)$$

It is interesting to note that the required reorientation is not a function of the thickness of the crystal.

In our experiment we used the values

$$\theta = 30^{\circ}$$

$$T_{\text{readin}} = 80^{\circ}\text{C}$$

$$T_{\text{readout}} = 25^{\circ}\text{C}$$

and

$$\Delta T \begin{cases} = T_{\text{readin}} - T_{\text{readout}} \\ = 55^{\circ}\text{C} \end{cases}$$

By substituting these parameters into equation 62, we find that

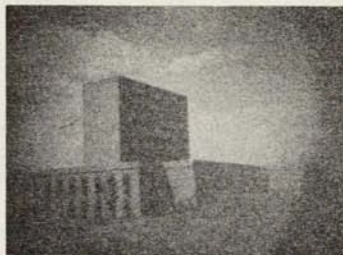
$$\theta' - \theta = 4.6 \text{ min of arc}$$

which is in exact agreement with the experimental result.

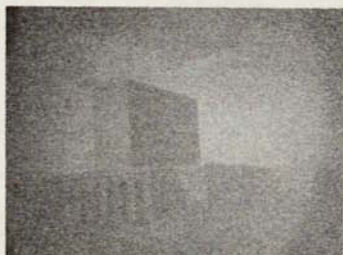
Although the required reorientation is not a function of crystal thickness, the thickness parameter plays an important role. This is particularly evident when complex gratings of a variety of fringe spacings are recorded. In such situations, the shrinkage effects on fringe spacing are varied so that the Bragg relation cannot be simultaneously satisfied for all fringes. The deleterious effect of nonuniform image intensity can then be observed. As the thickness of the crystal is increased, this problem is more severe because of greater angular orientation sensitivity. The photographs shown in figure 50 show the undesirable effects of a reduction in



(a) Temperature 80°C



(b) Temperature 75°C



(c) Temperature 70°C



(d) Temperature 65°C

FIGURE 50. DEGRADATION OF RECONSTRUCTED IMAGE DUE TO REDUCTION IN TEMPERATURE



temperature of a crystal during the reconstruction process. If at any temperature the hologram is reoriented by the proper amount, the quality of the reconstruction is essentially the same as the reconstruction obtained at 80°C.

A new technique proposed by Carson Laboratories can eliminate the shrinkage problem in KBr crystals. Retardation by red light or coloration of crystal is used. The recording takes place at room temperature using the He-Ne laser, while the crystal is being colored with incoherent UV radiation. This simultaneous illumination by UV and red light is essentially controlled coloration of the crystal. Shrinkage is eliminated, since it is no longer necessary to record at elevated temperatures and reconstruct at lower temperatures. In the photochromic glass and in some of the photochromic plastics, the problem of shrinkage is nonexistent since both readin and readout are done at room temperature.

#### A.7. RECIPROCITY FAILURE

Reciprocity failure provides a measurable criterion for determining the inefficiency of a recording medium at different levels of intensity relative to its efficiency at the optimum intensity. This measure plays an important role in wavefront reconstruction, particularly when a wide range of intensity levels are to be recorded.

A series of experiments was performed to measure the reciprocity failure of the KBr crystals. The amplitude transmittance was measured as a function of exposure for a 50-dB range of incident light intensities. The results for two different crystals are shown in figure 51. The reciprocity curves in each figure were measured for different bias levels of amplitude transmittance. In all cases, the results show severe high-intensity reciprocity failure.

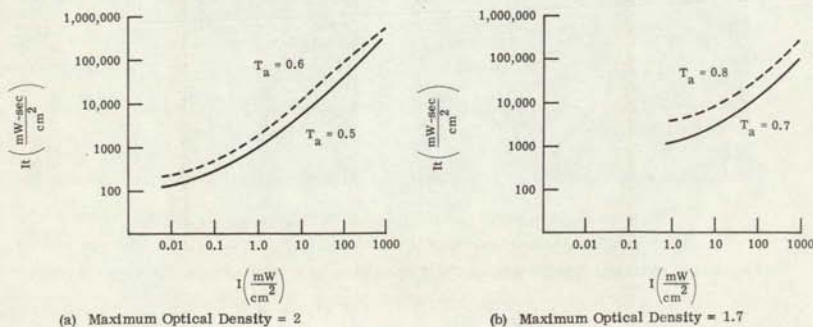


FIGURE 51. RECIPROCITY CURVES FOR KBr CRYSTALS. Thickness = 2 mm.

The implication of these results is indeed discouraging. We had hoped that by resorting to very intense illumination sources such as pulse lasers, we could appreciably reduce the readin time. It is evident from the results that this did not happen. The reciprocity law does not hold at any of the investigated intensity levels.

#### A.8. RECORDING COMPLEX INTERFERENCE PATTERNS

In order to demonstrate the use of photochromic materials in holography, experiments were performed in which the signal beam was spatially modulated by transparencies using both planar and diffuse illumination. Two different experimental setups for recording were used. In one, both the reference beam and signal beam were introduced from the same side of the recording medium. In the other, the reference beam and signal beam were introduced from opposite sides. The readout orientation sensitivity is relatively broad for the interference pattern resulting from the latter setup. The spectral resolution, on the other hand, is extremely narrow since the recorded gratings act as spectral interference filters. Readout with a mercury-arc source or a zirconium lamp produced single-color diffracted images of narrow spectral bandwidth.

It is interesting to note that the spectral sensitivity of thick photochromic materials is sufficiently great even for low offset angles that a back-reflection type of hologram is not required in order to obtain good reconstructions with white light. Figure 52 shows the reconstructed image of a signal comprised of transparent targets on a dark background. For the recording, the signal was coherently illuminated, and both the reference beam and the signal beam were introduced from the same side of the crystal. Figure 53 shows the reconstructed image of a

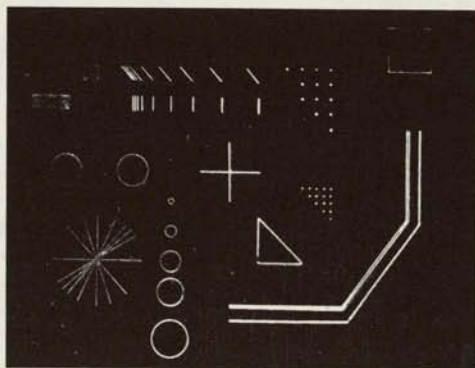


FIGURE 52. RECONSTRUCTED IMAGE OF COHERENTLY ILLUMINATED TRANSPARENT OBJECTS ON A DARK BACKGROUND

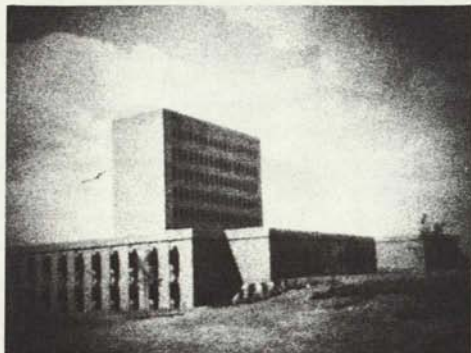


FIGURE 53. RECONSTRUCTED IMAGE OF A DIFFUSELY ILLUMINATED, TRANSPARENT, CONTINUOUS-TONE OBJECT

continuous-tone transparent signal which was diffusely illuminated during recording. In this case, the reference beam and the signal beam were introduced from opposite sides of the recording medium. The recording and readout were done with the 6328-Å illumination from a He-Ne laser. In both cases, the quality of the reconstructed images was comparable to results with Kodak 649F spectroscopic plates.

#### A.9. MULTICOLOR HOLOGRAPHY

As shown earlier, the silver halide photochromic glass is sensitive to various illumination wavelengths and therefore can be effectively employed in multicolor wavefront reconstruction. A number of experiments using photochromic glass was performed. A hologram made of three superimposed diffraction patterns was constructed. Each diffraction pattern resulted from the interference of reference and signal waves of only one of three illumination wavelengths, which were the 6328-Å wavelength derived from a He-Ne laser, and the 4880-Å and 5145-Å wavelengths from the argon laser. The signal used in our experiments was a diffusely illuminated multicolor transparency and the reference beam was a plane wave. The average angle subtended between the reference beam and signal beam was approximately  $10^\circ$ . The construction geometry was such that the reference beam for all three wavelengths was derived from a common point source.

The three wavelengths were then used in the reconstruction, again derived from a common point source, and the resulting reconstructed image was investigated. The reconstructed image, shown in figure 54 is of high quality and duplicates the color hues of the actual signal. In addition, the ghost images and attendant detrimental effects were completely absent. For



comparison, we used the same experimental setup and constructed a hologram with Kodak 649F spectroscopic plates. As shown in figure 55, the reconstructed image contains six ghost images. Some of them overlap on the desired image, resulting in a relatively poor reconstruction.

As demonstrated by the experimental results, there are obvious advantages in using the thick photochromic glass instead of photographic film. Unfortunately, the exposure times involved in our experiments were  $10^4$  times longer for the photochromic material than for the film.

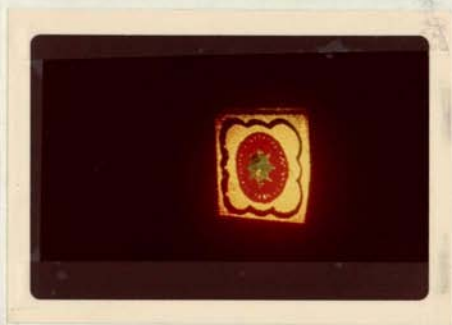


FIGURE 54. RECONSTRUCTED IMAGE OF A DIFFUSELY ILLUMINATED MULTICOLOR TRANSPARENCY USING SILVER HALIDE GLASS. Thickness =  $3175\ \mu\text{m}$ , offset angle =  $10^\circ$ .

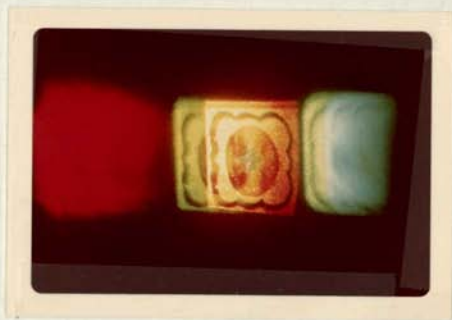


FIGURE 55. RECONSTRUCTED IMAGE OF A DIFFUSELY ILLUMINATED MULTICOLOR TRANSPARENCY USING KODAK 649-F SPECTROSCOPIC PLATES. Thickness =  $15\ \mu\text{m}$ , offset angle =  $10^\circ$ .

# REFERENCES

1. Optical Processing Techniques (Semiannual Status Report, 1 March 1967 Through 31 August 1967), Report No. 8688-1-P, Willow Run Laboratories, Institute of Science and Technology, The University of Michigan, Ann Arbor, December 1967.
2. E. N. Leith, et al., "Requirements for a Wavefront Reconstruction Television Facsimile System," J. Soc. Motion Picture Television Engineers, Vol. 74, 1965, p. 893.
3. Investigation of Hologram Techniques (Interim Technical Report), AFAL-TR-67-324, Radar and Optics Laboratory, Willow Run Laboratories, Institute of Science and Technology, The University of Michigan, Ann Arbor, January 1968.
4. K. A. Haines and D. B. Brumm, "Data Reduction of Holographic Information," J. Opt. Soc. Am., Vol. 57, 1967, p. 1412.
5. J. Upatnieks, "Reduction of Spatial Frequencies in Holograms Without Decreasing the Field of View," J. Opt. Soc. Am., Vol. 58, 1968, p. 589.
6. C. B. Burckhardt, "Information Reduction in Holograms for Visual Display," J. Opt. Soc. Am., Vol. 57, 1967, p. 1412.
7. K. A. Haines and D. B. Brumm, "A Technique for Bandwidth Reduction in Holographic Systems," Proc. IEEE, Vol. 55, 1967, p. 1512.
8. E. N. Leith and J. Upatnieks, "Holography through Diffusing Media," J. Opt. Soc. Am., Vol. 56, 1966, p. 523.
9. Davenport and Root, Random Signals and Noise, McGraw-Hill, Chapt. 13.
10. J. M. Burch and D. A. Palmer, Optica Acta, Vol. 8, 1961, p. 73.
11. C. B. Burckhardt, J. Opt. Soc. Am., Vol. 57, May 1967, pp. 601-603.
12. R. W. Green, The Production of Phase Images on Photographic Film, Report No. ECOM-00013-114 (6400-114-T and 7000-63-T), Willow Run Laboratories, Institute of Science and Technology, The University of Michigan, June 1967.
13. George T. Eaton, Photo Chemistry, Eastman Kodak Company, Rochester, New York, 1957, p. 87.
14. J. H. Altman, Appl. Opt., Vol. 5, October 1966, p. 1689.
15. Investigation of Hologram Techniques (Second Interim Engineering Report, 1 December 1965 Through 31 March 1966), Report No. 7421-22-P, Willow Run Laboratories, Institute of Science and Technology, The University of Michigan, Ann Arbor, July 1966.
16. W. P. Brown, Jr., "Validity of the Rytov Approximation in Optical Propagation," J.O.S.A., Vol. 56, No. 8, August 1966.
17. L. S. Taylor, "On Rytov's Method," Radio Science, Vol. 2, No. 4, April 1967, pp. 437-441.
18. J. Feinstein, "Some Stochastic Problems in Wave Propagation, II," IRE Trans. on Antennas and Propagation, April 1954, pp. 63-70.
19. R. Bellman and R. Kolaba, "On the Principle of Invariant Imbedding and Propagation Through Inhomogeneous Media," Proc. N.A.S., Vol. 42, 1956, pp. 629-632.

DISTRIBUTION LIST

NASA Technical Reports Officer  
Office of University Affairs, Code Y  
National Aeronautics and Space Administration  
Washington, D. C. 20546

(10)

*Do not Press*

20. R. P. Feynman, "Space-Time Approach to Non-Relativistic Quantum-Mechanics," Rev. of Modern Physics, Vol. 20, No. 2, April 1948, pp. 367-387.
21. Cramer, Methods of Mathematical Statistics.
22. J. Aitchison and J. A. C. Brown, The Lognormal Distribution, Cambridge Univ. Press, 1957.
23. M. Lowe, Probability Theory, D. Van Nostrand Co., Inc., Princeton, New Jersey, 1960.
24. W. C. Hoffman, "The Electromagnetic Field in a Randomly Inhomogeneous Medium," IRE Trans. on Antennas and Propagation (Special Supplement), December 1959, pp. S301-S306.
25. F. Riesz and B. Sz-Nagy, Functional Analysis, Frederick Ungar Publishing Company, New York, 1955.
26. R. Thrall and L. Tornheim, Vector Spaces in Matrices, Wiley, 1957, p. 65.
27. L. Cernov, Wave Propagation in Random Media, McGraw-Hill, 1960, p. 131.
28. P. Halmos, Measure Theory, D. Van Nostrand, 1950.
29. J. Doob, Stochastic Processes, Wiley, 1953, par. 2.